Accelerated Durability Testing via Reactants Relative Humidity Cycling on Polymer Electrolyte Membrane Fuel Cells

by

Karachakorn Panha

A thesis
presented to the University of Waterloo
in fulfillment of the
thesis requirement for the degree of
Master of Applied Science
in
Chemical Engineering

Waterloo, Ontario, Canada, 2010

Authors Declaration

I hereby declare that I am the sole author of this thesis. This is a true copy of the thesis, including any required final revisions, as accepted by my examiners.

I understand that my thesis may be made electronically available to the public.

_____

ABSTRACT

Cycling of the relative humidity (RH) levels in the reactant streams of polymer electrolyte membrane (PEM) fuel cells has been reported to decay fuel cell performance. This study focuses on the accelerated durability testing to examine different modes of membrane failure via RH cycling. A single PEM fuel cell with an active area of 42.25 cm^2 was tested. A Greenlight G50 test station was used to establish baseline cell (Run 1) performance with 840 hours of degradation under high-humidity idle conditions at a constant current density of 10 mA cm^{-2}. Under the same conditions, two other experiments were conducted by varying the RH. For the H_2-air RH cycling test (Run 2), anode and cathode inlet gases were provided as dry and humidified gases. Another RH cycling experiment was the H_2 RH cycling test (Run 3): the anode inlet gas was cycled whereas keeping the other side constantly at full humidification. These two RH cycling experiments were alternated in dry and 100% humidified conditions every 10 and 40 minutes, respectively. In the experiments, the fuel cells contained a Gore^{TM} 57 catalyst coated membrane (CCM) and 35 BC SGL gas diffusion layers (GDLs). The fuel cell test station had been performed under idle conditions at a constant current density of 10 mA cm^{-2}. Under the idle conditions, operating at very low current density, a low chemical degradation rate and minimal electrical load stress were anticipated. However, the membrane was expected to degrade due to additional stress from the membrane swelling/contraction cycle controlled by the RH.

In this work the performance of the 100% RH humidified cell (Run 1) was compared with that of RH cycling cells (Run 2 and Run 3). Chemical and mechanical degradation of the membrane were investigated using in-situ and ex-situ diagnostic methods. During the experiments, in-situ tests including polarization curves, electrochemical impedance spectroscopy (EIS), and linear sweep voltammetry (LSV) were employed. The EIS presented that the three runs had high charge transfer resistance due to the operation under idle conditions. The degradation of Run 1's, Run 2's, and Run 3's membranes was believed to be mainly caused by membrane thinning and crossover current for the first run and the delamination of catalyst/membrane layers for the latter two runs. For the LSV to

assess hydrogen crossover, it was obviously shown that the RH cycling cells (Run 2 and Run 3) had a higher crossover current than Run 1; the crossover current of Run 2 and Run 3 rapidly increased and exceeded 10 mA cm^{-2}, defined as the point of membrane failure at approximately 460 hours (Run 2) and 300 hours (Run 3) of operation as indicated by a sharp rise in crossover current, an increase in the degradation rate, and this could be associated with pinhole formation. Moreover, ex-situ tests such as ion chromatography, infrared (IR) imaging, and scanning electron microscopy (SEM) were performed after disassembling the fuel cells. The ion chromatography showed that Run 2 and Run 3 had a higher fluoride ion release concentration, arising from degradation of the membrane structure. Also, the results from the IR and SEM images illustrated that the RH cycling enhanced the stresses on the membrane by showing hot-spot/pin-hole formation, membrane thinning, membrane fusion, and membrane delamination.

In addition, features of the performance polarization curves and degradation curves had been identified and co-related to the membrane failure modes. The RH cycling cells have illustrated a higher rate of membrane degradation than the 100% RH humidified cell. The overall voltage degradation rate for steady state conditions was found to be lower than under RH cycling conditions; 0.18 mV h^{-1} (Run 1), 0.24 mV h^{-1} (Run 2), and 0.3 mV h^{-1} (Run 3). From the deviation and change in slope of the polarization curves and voltage degradation curves, it was believed that the membrane failure, likely due to pinhole formation, was rapidly occurred at approximately 620 hours, 460 hours, and 300 hours for Run 1, Run 2, and Run 3, respectively.

The results of each measurement during and after fuel cell operation are consistent. They clearly show that changing in RH lead to an overall PEM fuel cell degradation due to the increase in membrane degradation rate from membrane resistance, fluoride ion release concentration, hydrogen crossover current, membrane thinning, and hot-spot/pin-hole formation. The variation in RH is equivalent to the change in mechanical load which is believed to be a major driving force that could accelerate mechanical failure of the membrane in PEM fuel cell system.

RH cycling has shown to be a suitable accelerated durability test that leads to rapid membrane mechanical failure. It also shows that this mechanical failure is likely due to pinhole formation, although the RH cycling of an anode side only may have also led to membrane delamination. The slope of the voltage degradation curve with time certainly is indicative of a pinhole formation and thus would make it a useful tool for cell diagnostic in operating fuel cell stacks.

ACKNOWLEDGEMENTS

This work could not have been done without Dr. Michael Fowler who not only served as my supervisor but also encouraged and challenged me throughout my Master's program. He guided me through this project and never accepting less than my best efforts.

I wish to thank Xiao-Zi (Riny) Yuan through the National Research Council Canada (NRC)-Helmholtz Joint Research Program and the Natural Sciences and Engineering Research Council (NSERC), for valuable suggestions and financial support.

I would like to take the opportunity to thank Dr. Rapeepong Suwanwarangkul, my undergraduate advisor, for supporting me at the beginning of this study. He was the one who encouraged me to study here at University of Waterloo.

I would also like to thank all my friends and my co-op students in fuel cell lab that came up to me and helped me during this work. In particular, Rungsima Yeetsorn who was always with me and gave me guidance to solve all the experimental problems. Vengatesan Singaram for his suggestion on the writing. Marcus Pang for his great assistant, as well as Alisha, Drawn, Jae, Shahab, and Jeff.

Special thanks to Atchariya, Tassanee, Justin, Kadia, Rebecca, and all my Thai friends both undergraduate and graduate students here, for their entertainment keeping me happy during my study abroad.

All my gratefulness goes to my parents, brothers, and all my family in Thailand, especially, my mom for listening, cheering up, and supporting every decision I made. Without you, I could not imagine how I could survive the loneliness here throughout the whole two years.

TABLE OF CONTENTS

LIST OF FIGURES

NOMENCLATURE

a	Activities coefficient of reactant	-
A_{Pt}	Platinum surface area	cm^2
C_{F-}	Fluoride ion concentration	mol L^{-1}
C_{H_2}	Hydrogen concentration	mol m^{-3}
E°	Nernst Potential	V
EAS	Electrochemically active surface area	m^2_{pt} cm^{-2}_{geo}
F	Faraday's constant (96485)	C mol^{-1}
i	Current density	A cm^{-2}
i_o	Exchange current density	A cm^{-2}
i_{H_2}	Hydrogen crossover current	A cm^{-2}
L_{ca}	Platinum loading	mg cm^{-2}_{geo}
N	Number of electrons transferred in an electrochemical reaction	-
N_i	Flux of species i	mol cm^{-2} s^{-1}
p_i	Partial pressure of species i	mmHg
$P_M^{'}$	Permeability of gas through a membrane	A cm cm^{-2} $mmHg^{-1}$
R	Ideal gas constant (8.314)	J mol^{-1} K^{-1}
R_v	Reaction rate	mol m^{-3} s^{-1}
R_Ω	Membrane resistance	Ohms
T	Temperature	K
V_{Cell}	Cell voltage	V
$V_{Cell,OCV\ i}$	Cell voltage at OCV	V
δ	Membrane thickness	µm
η_{act}	Activation loss (overpotential)	V
η_{ohm}	Ohmic loss (overpotential)	V
η_{conc}	Concentration loss (overpotential)	V

A	Electron transfer coefficient	-

LIST OF ABBREVIATIONS

BSE	Backscattering – For scanning electron microscopy method.
CC	Crossover current – A measure of hydrogen crossover.
CCM	Catalyst coated membrane
Cumulative fluoride release	The total amount of fluoride release on either the anode or cathode side.
DI	Deionised water
EAS	Electrochemical active surface area
EDS	Electron dispersive
ESR	Electron spin resonance
Fluoride release rate	The rate of fluoride release or fluoride emission rate on either the anode or cathode side.
GDL	Gas diffusion layer
IR camera	Infrared camera – To observe the thermal profile of the MEA.
LPM	Litres per minute
MEA	Membrane electrode assembly
OCV	Open circuit voltage – The voltage when no current is flowing.
ORR	Oxidation reduction reaction
PEM	Polymer electrolyte membrane
PFSA	Perfluorosulfonic acid
Polarization curve	A voltage versus current density plot used to assess fuel cell performance.
PTFE	Polytetrafluoroethylene
RH	Relative humidity
SE2	Secondary electron emissions – For scanning electron microscopy method.
SEM	Scanning electron microscope – To characterize the morphology of the membrane and to measure the membrane thickness.
SLPM	Standard litres per minute – 0°C, 1 atm.
Stoichiometry	The amount of excess reactant fed to the anode or cathode.

Test station	The unit used to test fuel cell and assess fuel cell performance.
TP50	A single TP50 fuel cell (Tandem Technologies) with an active area of 42.25 cm^2.

CHAPTER 1: INTRODUCTION

1.1 Overview and Objectives

One of the most important issues in the development of polymer electrolyte membrane (PEM) fuel cells is membrane durability [1-3]. Recently, the membrane durability has been focused by many studies, including the development of a dynamic semi-mechanistic chemical degradation model [4], membrane preparation and modification, degradation of membrane electrode assembly, and catalyst layer design [5]. The results show that relative humidity (RH) is one of the major factors with respect to long term fuel cell performance. A limited number of researches have investigated the effects of RH of the reactant streams on PEM fuel cell performance [3]. Change in the RH of the inlet gases has been reported to decay fuel cell performance as an increased membrane resistance by reducing proton conductivity of membrane, decreasing electrode kinetics including electrode reaction, mass diffusion rates, and Pt catalyst utilization, and inducing mechanical failure on the fuel cell components [3, 5].

The objective of this work is to investigate the effect of RH of the reactant streams on PEM fuel cell performance and durability. Chemical and mechanical degradation of the electrolyte membrane via RH cycling are studied. The experiments were performed under an idle condition (i.e. operated at 10 mA cm^{-2}). This experiment is considered as an

accelerated durability testing. The accelerated test is desirable since it is impractical and costly to run a routine lifetime fuel cell test.

1.2 Scope of Work

The scope of this work is to examine the chemical and mechanical degradations of the PEM under a variation in RH. Gore^{TM} 57 catalyst coated membrane (CCM) is used with a single 'TP50' PEM fuel cell. The effect of RH is employed at a constant current density of 10 mA cm^{-2}, under idle conditions. Idle conditions were selected to isolate the RH effect by creating condition with low current stress, and a minimum of chemical degradation. The experiments are performed at a 70 ℃ constant cell temperature. The temperature effect is not included in this work. The test station is operated under high relative humidity (Run 1), under H_2-air RH cycling (Run 2), and under H_2 RH cycling (Run 3).

1.3 Thesis Layout

The chapters of this work will be organized in the following way as summarized below:

Chapter 2: Background of PEM Fuel Cell

In this chapter, an introduction to PEM fuel cell, PEM fuel cell operation, membrane durability including chemical and mechanical failures of the polymer electrolyte membrane, as well as relevant studies of the relative humidity effects from the literature will be presented.

Chapter 3: Experimental

This section will describe the fuel cell test station set-up and experimental procedures, leak testing, crossover testing, and commissioning of the fuel cell. The membrane electrode assembly diagnostic techniques that were used during and after the experiments such as polarization curves, voltage degradation curve, electrochemical impedance spectroscopy, linear sweep voltammetry, ion chromotrography, infrared imaging, and scanning electron microscopy will be mentioned.

Chapter 4: Experimental Results - RH Cycling Effects on PEM Fuel Cell

This chapter will discuss RH effect on PEM fuel cell performance, hydrogen crossover current, fluoride ion release, hot-spot/pin-hole formation, membrane thickness, and membrane morphology.

Chapter 5: Conclusions and Suggestions for Future Work

The comparison of Run 1 (100% RH humidified cell), Run 2 (H_2-air RH cycling cell), and Run 3 (H_2 RH cycling cell) and the suggestions for the future work will be summarized in this chapter.

CHAPTER 2: BACKGROUND

2.1 Introduction to Polymer Electrolyte Membrane (PEM) Fuel Cells

The concept of a *hydrogen economy* has attracted a great deal of attention in society as it holds the promise of zero emission transportation. Hydrogen as an energy carrier can be produced from multiple energy resources like nuclear and renewable clean electricity sources, and then used for end-uses such as transportation or electricity generation. The long term view of the hydrogen economy involves the use of emission free sources of energy and the generation of emission free electricity on demand. In order to address urban air quality and climate change issues a transition of the existing energy system to a more sustainable framework is required. The development of the *hydrogen economy* concept concentrates on the study of the economic aspects associated with the production, distribution and utilization of hydrogen in energy systems [7].

Hydrogen is a desirable energy vector because it can be stored and then used to generate electricity either in stationary or transportation applications. The use of hydrogen in transportation applications will result in decreased urban air pollution and greenhouse gas emissions, as well as diversified energy production and security of energy supply. Most importantly, because it is easily generated and stored, hydrogen is an ideal energy vector

to facilitate the integration of intermittent renewable energy sources (i.e. wind and solar) into an electrical grid where the demand profile is not consistent with the energy supply profile. From the electrical power grid management point of view, the use of hydrogen as an energy carrier is appealing, given its energy storage potential, and where there are technical limitations in electricity distribution such as transmission congestion. Hydrogen in transportation applications, especially light duty vehicles and rail, is an onboard fuel that provides rapid refueling, high reliability, zero emissions, and high conversion efficiency. Hydrogen will become an integral part of integrated energy systems [7, 8].

A fuel cell is an electrochemical energy conversion device that converts the chemical energy of a reaction directly into electrical energy. Fuel cells produce electricity, water, and heat using fuel and oxygen. The fuel is not combusted or burned in a flame or explosion, but oxidized electrochemically. It means that the fuel cells are not constrained by the Carnot limit, the fundamental law that governs heat engines. As the result, the fuel cells can provide high efficiency compared to internal combustion engines [8].

Even though the fuel cells have components and characteristics similar to a typical battery, they differ in several points. The battery is an energy storage device which the maximum energy available is determined by the amount of chemical reactant stored within the battery itself. The battery produces electrical energy when the chemical reactants are consumed. After the reactants are used up the battery must be either recharged or replaced [6, 7]. In contrast, the fuel cell is an energy conversion device which theoretically has the capability of producing electrical energy for as long as the fuel and oxidant are supplied to the electrodes. Furthermore, the fuel cells also have several advantages over batteries including smaller in size, lighter weight, and quicker refuelling [8]. Fuel cells have two or up to three times more efficient than an internal combustion engine in converting fuel to power. The internal combustion engine (ICE) changes chemical energy of fuel to thermal energy, it could be able to generate mechanical and electrical energy at the end.

However, for fuel cells, they can convert chemical energy directly to electrical energy as mentioned earlier. Therefore, the efficiency of internal combustion engines is less than

fuel cells due to the loss in conversion of thermal to mechanical energy. A fuel cell system has an electric energy efficiency range from 40% to 60%, based on the lower heating value of the fuel, as opposed to heat engines in ICEs which are roughly 20% to 25% [6-8].

Critical to the *hydrogen economy* is the ability to transform hydrogen into electricity and this is the role fuel cells play. Many advantages of the fuel cell technology are summarized as follows [7]:

1) High Efficiency

Fuel cells convert chemical energy directly to electrical energy; therefore there is no requirement for a conversion of heat to mechanical energy. The fuel cells operate at a more uniform efficiency under changing load conditions compared to heat engines, and have rapid load following capability.

2) Lower Environmental Burden and Emissions

Fuel cells produce electricity at lower temperatures compared to combustion systems. Since they use hydrogen there is no associated spills of hydrocarbons. Their operation also results in much lower air pollutant emissions and no emissions if hydrogen is the fuel. Emissions of acid rain and smog components, such as SO_x and NO_x, are especially low. Fuel cells also are very quiet in operation.

3) High Reliability

Since there are few moving parts in a fuel cell system, a high reliability can be achieved.

4) Flexibility of Design

Modular installations are used to match loads and improve reliability while providing size flexibility. This makes possible remote and unattended operation.

5) Easily Refuelled

Fuel cells can be quickly recharged or refuelled (unlike a traditional battery), and this can be repeated through a large number of cycles. Fuel cells have many advances over batteries specifically range, refuelling time and durability.

6) Co-generation Capability

High-quality and low-quality heat is available for co-generation, heating, and cooling in residential, commercial, and industrial applications.

Recently, there are many uses for fuel cells, including a wide array of stationary and mobile applications. More than 2500 fuel cell systems have been installed all over the world [7]. Fuel cells in stationary systems, including wastewater treatment plants, utility power plants, office buildings, and landfills are using fuel cells to convert raw materials into electricity, provide supplemental power, and backup for critical areas [6]. With respect to fuel cells in mobile applications, most major automakers are working to commercialize fuel cell vehicles. Currently, the fuel cells vehicles are in development, and several begun leasing in larger quantities. The mobile fuel cells are used in buses, boats, trains, planes, scooters, forklifts, and even bicycles. Furthermore, fuel cells are being designed for use in portable electronic devices such as mobile phones, and laptop computers [6-8].

Nevertheless, several barriers still exist for a widespread of fuel cell commercialization; in particular, cost and durability of fuel cell system. Firstly, the distribution and refuelling infrastructure for hydrogen is not yet in place. Secondly, the amount of rare metals in electrocatalysts (i.e. Pt) must be reduced before mass production. Overall, the capital costs are high, and cost reduction targets still require improved catalysis utilization (or non-noble metal catalyst development), lower cost membrane materials, and high volume production methods.

Enhancing the durability of fuel cells is also one of the key research and development goals being considered for a widespread use of fuel cells. The fuel cells should be able to

resist permanent change in performance over time. Lighter and stronger materials are also needed to be developed for feasible fuel cell applications. While these are current barriers, it is expected that by 2020, which is the earliest by which the hub is expected to be constructed, durability issues will likely have been overcome, and costs for fuel cells will be closer to US Department of Energy's $30/kW target for transportation. Most automobile manufacturers expect to commercialize their fuel cell vehicles by 2015. This will require hydrogen re-fuelling stations to support an initiating hydrogen economy, thereby inevitably leading to a demand of established hydrogen infrastructure by 2020 [6-8].

Although there are six types of fuel cells as shown in the figure below, PEM fuel cells are of the greatest interest to the transportation sector.

	Low-Temperature Fuel Cells			High-Temperature Fuel Cells		
Types of fuel cells	Direct methanol fuel cell (DMFC)	Polymer electrolyte membrane fuel cell (PEMFC)	Alkaline fuel cell	Phosphoric acid fuel cell (PAFC)	Molten carbon fuel cell (MCFC)	Solid oxide fuel cell (SOFC)
Electrolyte	Proton conducting membrane	Proton conducting membrane	Caustic potash solution	Concentrated phosphoric acid	Molten carbonate	Ceramic
Temperature range (°C)	< 100	< 100	< 100	~ 200	~ 650	800 - 1000
Fuel	Methanol	Hydrogen	Hydrogen	Hydrogen	Natural gas, coal	Natural gas, coal
Power ranges	Watts/ kilowatts	Watts/ kilowatts	Watts/ kilowatts	Kilowatt	Kilowatts/ megawatts	Kilowatts/ megawatts
Application areas	Vehicles, small appliances	Vehicles, small generators, domestic supply, block-type heat and power stations	Space	Block-type heat and power stations	Power plants, combined heat and power	Power plants, combined heat and power

Figure 2-1. Types of fuel cells [7].

Figure 2-1 shows that fuel cells are classified primarily by the type of electrolyte they employ. This determines the type of chemical reactions that take place in the cell, the type of catalysts required, the temperature range in which the cell operates, the fuel required, and some other factors. At present, there are several types of fuel cells under development, each with its own limitations and potential applications [8]. This thesis focuses on the PEM fuel cell, which uses of hydrogen and oxygen as reactants and a polymer membrane as electrolyte.

2.2 PEM Fuel Cell Operation

PEM fuel cells are attracting much attention as power sources for many applications. PEM fuel cells use a proton exchange membrane such as Nafion^{TM} as an electrolyte. The PEM fuel cells are a low-temperature fuel cells typically operate at 60 – 80 ^{o}C [8], allowing for fast start up and immediate response to change in the demand of power. They are environmentally friendly energy producers that improve on the internal combustion engine by producing power more efficiently without any harmful emissions. Currently, PEM fuel cells are thus one of the leading clean energy technologies being considered for transportation applications and power generation [6].

In this work, a Tandem TP50 fuel cell, a typical single PEM fuel cell, was used. A schematic of a single TP50 physical structure is shown in Figure 2-2. The TP50 fuel cell consists of end plate, manifold fluid inlet/outlet plate, anode and cathode current collectors, anode and cathode cooling water flow field plates, anode and cathode flow field plates, gas diffusion layers, membrane electrode assembly, electrical/thermal isolation plate, and compression endplate. TP50 fuel cell assembly procedure is presented in Appendix A.

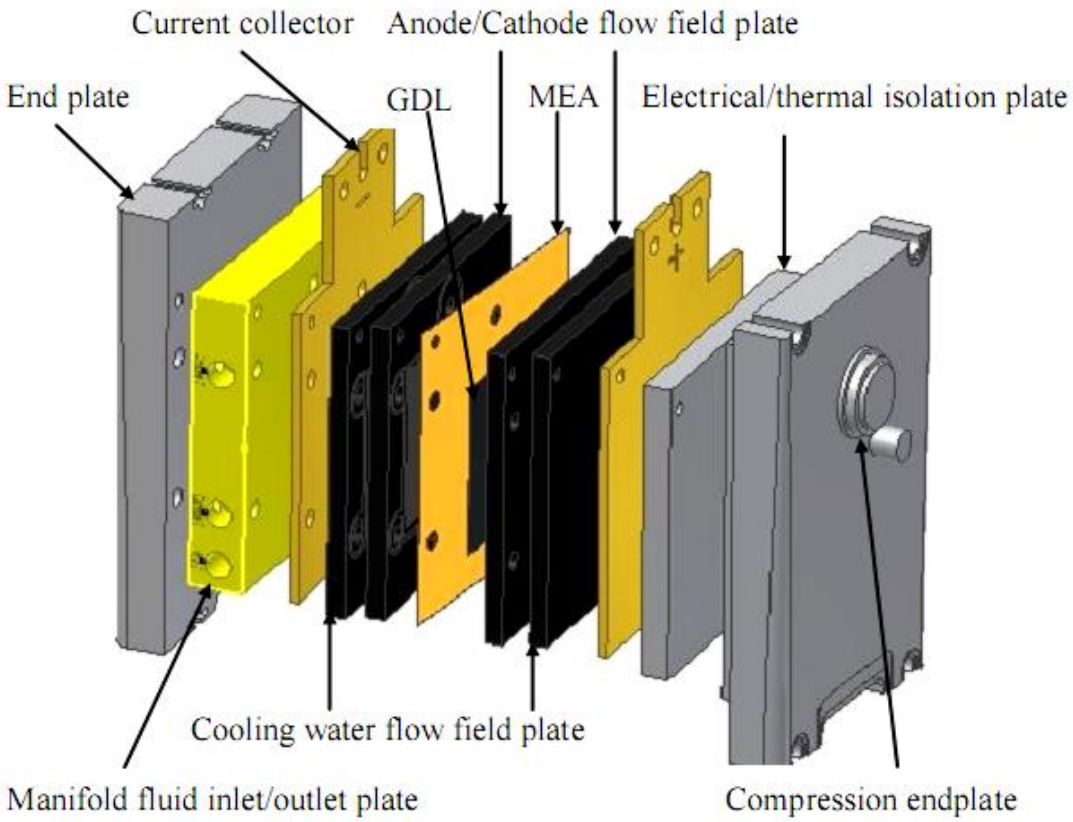

Figure 2-2. Schematic of a single TP50 PEM fuel cell.

An expanded view of a typical PEM fuel cell is shown in Figure 2-3. Note that the combination of the gas diffusion layers (GDLs) on the anode and cathode sides, catalyst electrode layers on the anode and cathode sides, and the membrane electrolyte is commonly referred to as the membrane electrode assembly (MEA). While the composite material formed by the catalyst and electrolyte layers is typically called a catalyst coated membrane (CCM).

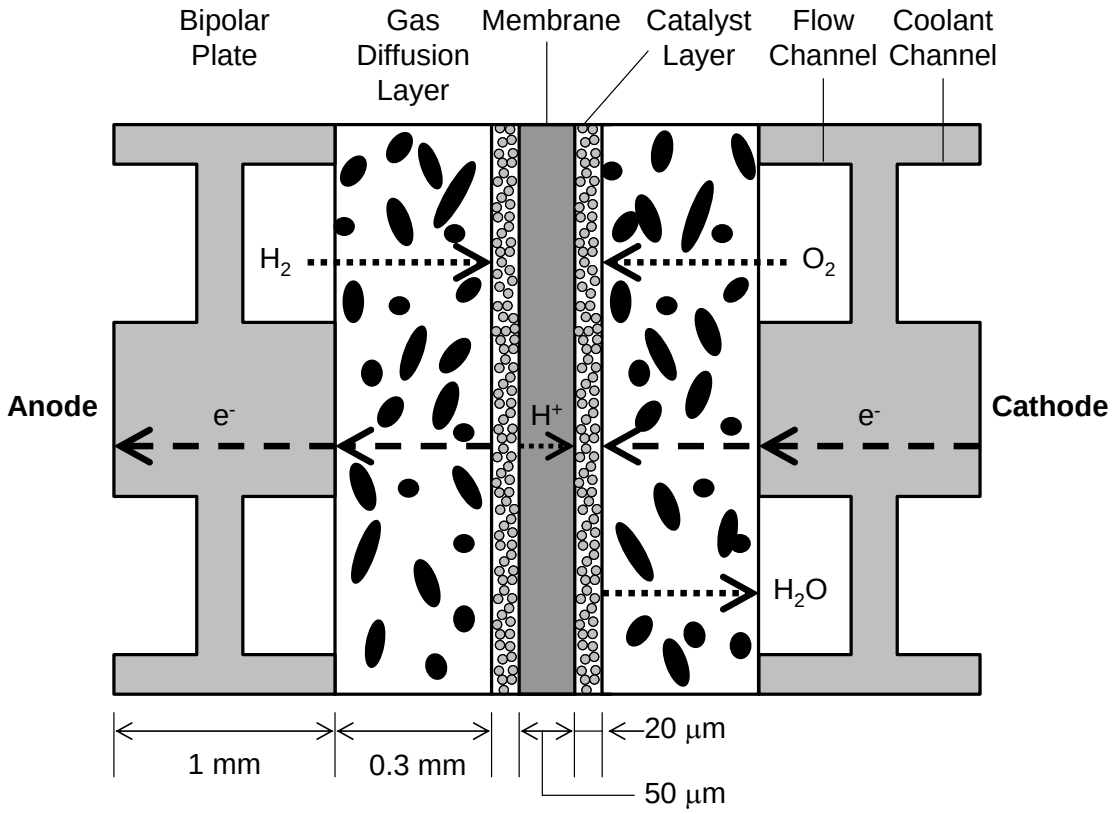

Figure 2-3. Internal components of a typical PEM fuel cell in an expanded view. [9].

Generally, the PEM fuel cell consists of an electrolyte membrane layer in contact with porous anode and cathode on either side. The anode and cathode electrodes are exposed to gas flow channels contacting with fuel or oxidant – hydrogen or oxygen/air [6]. Figure 2-4 shows the basic PEM fuel cell operation. As hydrogen gas flows into the fuel cell on the anode side, a platinum catalyst facilitates the separation of the hydrogen gas into electrons and hydrogen ions. The electrons which cannot pass through the membrane are forced to move around an external circuit and produce power via a motor or other electrical load. Whereas, the hydrogen ions pass through the membrane and with the help of a platinum catalyst on the cathode side, the ions combine with oxygen and the returning electrons. Product water is then produced [8].

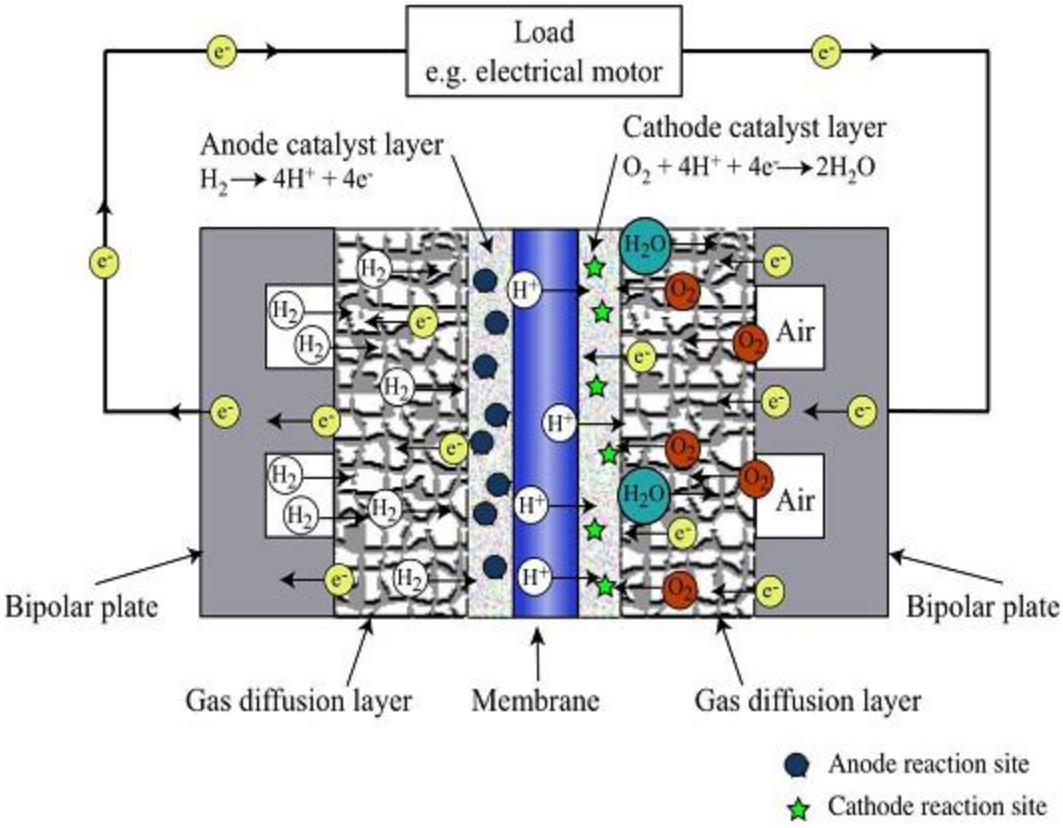

Figure 2-4. Operation schematic of a PEM fuel cell [9].

2.3 Performance of PEM Fuel Cells

Typically, a fuel cell performance is evaluated by a polarization curve. The polarization curve is a plot of cell potential versus current density. Figure 2-5 shows the performance of a single fuel cell operated at 70 ^{o}C without backpressure. The power density produced from the cell is also included in the figure. Changes in the polarization curves can give an indication of what material characteristics or components have been degraded. The curve can be segmented into four regions each characterized by a loss from ideal Nernst potential. The effect of different regions including an open circuit voltage (OCV), an activation loss (η_{act}) region, a linear ohmic loss (η_{ohm}) region, and a mass transfer limited (η_{conc}) region expresses a decrease in voltage output of the fuel cell [8].

Cell potential or cell voltage achieves the maximum voltage value at the OCV where there is no current flow. At low current densities, activation polarization is the major loss of performance. The activation polarization experiences due to the loss in total surface area of active platinum catalyst. The loss of active surface area is typically seen as a downward translation of the voltage. At intermediate current densities, ohmic loss is predominant. The ohmic loss is due to both the ionic conductivity and the electron conductivity of the membrane and gas diffusion layer (GDL), respectively. Moreover, the loss is also related to contact resistances between each of the fuel cell materials resulting in a deviation of slope in the linear region of the curve. At high current densities, the loss is caused by concentration polarization. The loss by mass transfer is limited when reactants cannot be supplied to the active catalyst sites quickly enough. The presence of too much product water on the cathode side will block the pores and add an extra resistance to the flow of oxygen to the catalyst sites. Consequently, a sharp drop can be observed at the end of the polarization curve [8, 10-12].

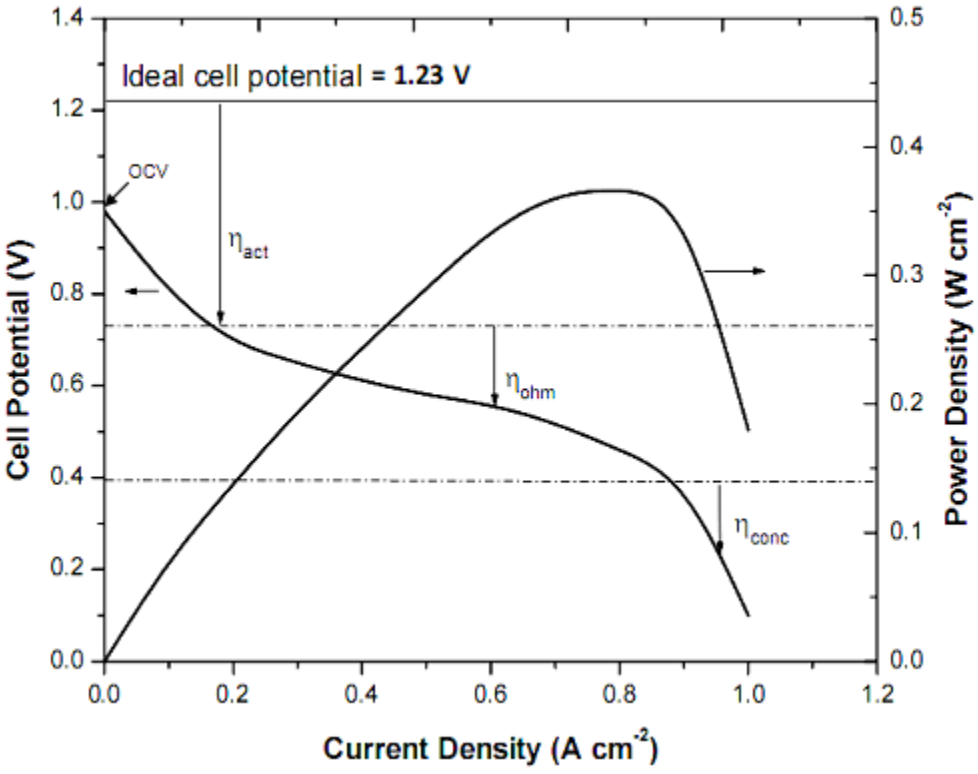

Figure 2-5. Polarization curve of a single PEM fuel cell.

During the fuel cell operation, the cell potential is dependent on several factors such as temperature, pressure, as well as the mole fraction of the reactants [6]. The Nernst equation is a relationship between the cell potential and these variables as expressed in Equation 2-1.

$$\Delta E = \Delta E^{0} - \frac{RT}{2F} \ln \left(\frac{a_{H_2O}}{a_{H_2} a_{O_2}^{1/2}} \right) \qquad \text{Equation 2-1}$$

where R is the universal gas constant, T is the absolute temperature, F is Faraday's constant, and a_{H_2O}, a_{H_2} and $a_{O_2}^{1/2}$ are the activities of water, hydrogen and oxygen, respectively.

In theoretical considerations, the overall electrochemical reaction of a single fuel cell will produce 1.229 V at 25°C room temperature and 1 atmospheric pressure. The cell potential (V_{Cell}) should approach the ideal equilibrium potential (E^o) when there is no current flow. However, internal currents caused by inefficiencies in the cell such as leakage of H_2 from anode compartment to cathode compartment, and Pt oxidation, are believed to lower the open circuit potential below the Nernst potential. Therefore in practice, the highest achievable open circuit voltage for a single fuel cell is approximately lies between 0.95-1 V [11, 13].

When current is actually flowing, the cell voltage will be lower due to the losses associated with current flow, i.e., ohmic resistance through the electrolyte, electrodes and external connections, kinetic limitations of the electrode reactions, and mass transfer limitations of reactants at the electrode surfaces [7, 8, 14].

Overall fuel cell potential can be expressed as follows:

$$V_{Cell} = E^o - \eta_{act} - \eta_{ohm} - \eta_{conc} \qquad \text{Equation 2-2}$$

Activation loss (η_{act}) is the dominant source of energy losses in fuel cell operation. The loss arises due to the slowness of the reactions taking place on the surface of the electrodes. A proportion of the voltage generated is lost during chemical reaction that transfers the electron to or from the electrode which mainly occurs at the cathode. It is a rate limiting reaction. Due to its relationship to reaction rates, the activation polarization is also affected by the total active surface area of the catalyst surface. Losses of the active catalyst surface area during the operation due to phenomena such as particles falling off the electrode backing material or the build-up of solid reaction products on the catalyst particles are the cause of the activation loss [8, 11].

The loss at the cathode from the oxygen reduction reaction (ORR) is related to platinum surface area ($A_{Pt,el}$), platinum loading (L_{ca}), current and exchange current density (i_o) as well as the fuel cell current (i) which can be expressed by Equation 2-3 [8].

$$\eta_{act} = \frac{RT}{n\alpha F} ln\left[\frac{i}{10\cdot(L_{ca}A_{Pt,el})\cdot i_o}\right] \qquad \text{Equation 2-3}$$

where n is the number of electron transferred (in this case 2) and α is the transfer coefficient (taken to be 0.5).

Ohmic loss (η_{ohmic}) is mainly caused by the resistance to ion flow through the electrolyte membrane and the resistance to electron flow through the GDL. It is also due to an increase in contact resistances between the different components as well as electronic resistance through the bipolar plate. In the ohmic loss region, the voltage is simply proportional to the current. The loss can be modeled as a function of current using Ohm's law as given in Equation 2-4 [11].

$$\eta_{ohm} = iR_{\Omega} \qquad \text{Equation 2-4}$$

where R_{Ω} is the ohmic resistance.

Concentration loss (η_{conc}) is predominant in the case where the reactants have a difficulty in increasing the rate of supply quickly to respond to demand. Under high current densities, the kinetic of the electrode reactions is so high that the transport of the reactants to the active catalyst sites limits the rate at which the fuel cell can operate. An empirical equation below (Equation 2-5) is used to express the concentration loss. This approach gives a good fit to the results and appears to be quite widely used in the fuel cell community [11].

$$\eta_{conc} = m \exp(ni) \qquad \text{Equation 2-5}$$

where m and n are constants, m is typically about 3×10^{-5} V, and n is about 8×10^{-3} $cm^2\ mA^{-1}$.

As the above description of the overall cell potential, the fuel cell potential is related to a number of different material parameters. From the beginning and during fuel cell operation, the materials characteristics will inevitably change and start to degrade. As a result, the fuel cell performance, observed by the polarization curve, will drop. Therefore, for a better fuel cell development, it is important to understand how the material properties change with time. In this work, membrane durability of the PEM fuel cell is mainly focused.

2.4 Membrane Durability

The membrane acts as a proton conductor in the PEM fuel cell systems, as well as electronic and physical gas barrier between the anode and cathode. It is required to be well humidified because the proton conduction process relies on transfer of the proton (i.e. H^+) through water and fully hydrated sulfonic acid groups of the membrane. During a fuel cell operation, an additional water flux (electro-osmotic drag) from anode to cathode associated with the migration of protons is present. This electro-osmotic drag will lead to a

depletion of water from the anode interface of the membrane, therefore pre-humidifying the inlet reactant gases is often provided before the gases flowing to the fuel cell [15].

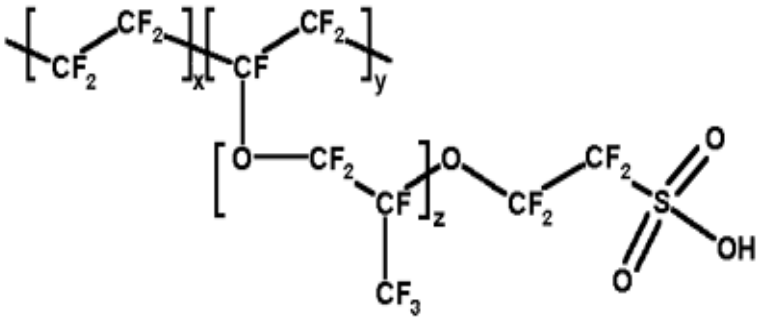

Figure 2-6. Nafion® structure [8].

Nafion®, a polymer in the perfluorosulfonic acid (PFSA) family, is commonly used as a membrane material in PEM fuel cells. It consists of three regions: a polytetrafluoroethylene (PTFE) - like backbone, a perfluorinated side chains which connect the molecular backbone to the third region, and ion clusters consisting of sulfonated (SO_3^-) end groups as shown in Figure 2-6 [8]. Ion conduction can only occur at desired rates when the membrane is hydrated with water. Once the membrane becomes hydrated, the hydrogen ions in the third region will mobilize by bonding to the water molecules and moving between sulfonic acid sites [13]. The water molecules from interconnected acidic domains are the major path for a proton transport across the membrane. Also, as the sulfonic end groups separate into clusters, water uptake will occur and cause swelling of the ionomer. Both the proton conductivity and the swelling are increased by the level of hydration. In contrast, a lower hydration level of the membrane can result in decreased proton conductive, as well as an associated increase in ohmic (IR) losses. With more ohmic losses, there is more heat generated in the membrane and thus more membrane dehydration. During fuel cell operation, the hydration level might change due to a transient state of operation. The changes in hydration, pressure, and temperature will be the driving forces of the degradation inside the membrane [16, 17].

To generate power efficiently via the electrochemical reactions, PEM fuel cells require adequate water content in the electrolyte membrane. With improper water management, an imbalance between water production and water removal from the fuel cell will appear. In the case that the reactant gases at the catalyst sites are not humidified and more water is removed than produced, it will result in membrane dehydration. The membrane dehydration or drying-out of the membrane will lower ionic conductivity of the electrolyte [14, 18]. The dehydration can also accelerate the rate of membrane degradation [19].

Therefore, the fuel cell is normally operated at high humidity for a better performance and a high durability. The higher the hydration state the better the conductance of the membrane [15]. However, too much water in the fuel cell will block the pores in the electrodes or GDLs, which causes membrane flooding (i.e. blocking of the GDL or pores in the electrode) and leads to gas diffusion limitation. This flooding will lower the gas diffusion rates to the electrochemically active layers, causing a loss in overall fuel cell performance [20]. Both the membrane dehydration and the membrane flooding are well-known factors that negatively impact on the PEM fuel cell performance [21].

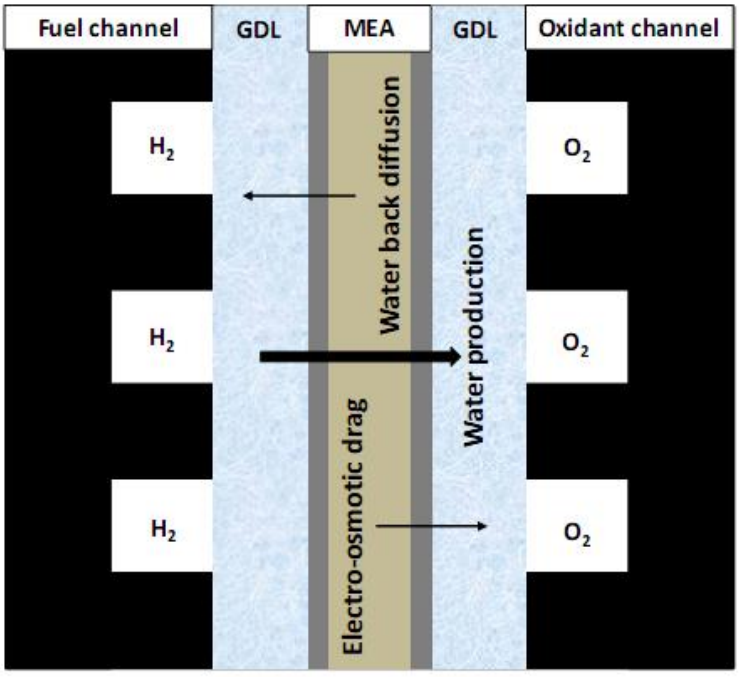

Figure 2-7. Water movement inside a PEM fuel cell.

Water movement inside the PEM fuel cell is shown in Figure 2-7. As already mentioned, the movement of water is related to the fuel cell performance. From the aspect of operation, the water can be supplied to the cell via the reactant gases if external humidification is used [22, 23]. Also, hydrogen ions moving from anode to cathode will pull some water molecules with them. This process is called electro-osmotic drag. Each hydrogen ion usually drags 1 - 5 water molecules. At high current densities operation, however, the electro-osmotic drag can dry-out the anode if there is too much water movement from the anode to cathode [17, 18]. At the cathode side, water is produced by electrochemical reactions. Water production at the cathode can increase water concentration gradient between the anode and cathode. The water concentration gradient will then generate water back-diffusion effect which is the movement of the water from the cathode back to anode driven by the concentration gradient [24, 25].

In a number of studies [3-5, 24-27], the hydration of the fuel cell has been shown to have chemical and mechanical effects on membrane durability. The membrane or the membrane electrode assembly (MEA) becomes weakened by the change in water level inside the MEA. Variation in the MEA hydration leads to membrane failure which is believed to be caused by chemical and mechanical effects acting together. Chemical effects such as hydrogen peroxide formation, cationic contaminants, and reactant gas cross over are all considered to be major factors contributing to the chemical failure of the membrane. Mechanical effects including cyclic stresses and strains are expected to be the mechanical failure in the fuel cell components.

2.4.1 Chemical Failure

Chemical degradation is considered to be one of leading factors for poor membrane lifetime that related to failure of membrane layer [28]. Residual carboxylic end groups from the Nafion^{TM} manufacturing process may be susceptible to be attacked by radical species generated during fuel cell reactions as shown in the following reactions (Reaction 1 – 3) [15]:

$$R\text{-}CF_2COOH + OH\bullet \longrightarrow R\text{-}CF_2\bullet + CO_2 + H_2O \qquad \text{Reaction 1}$$

$$R\text{-}CF_2\bullet + OH\bullet \longrightarrow R\text{-}CF_2OH \longrightarrow R\text{-}COF + HF \qquad \text{Reaction 2}$$

$$R\text{-}COF + H_2O \longrightarrow R\text{-}COOH + HF \qquad \text{Reaction 3}$$

The radical species, such as hydroxyl radicals, are formed by the decay of hydrogen peroxide which is an intermediate of the electrochemical oxygen reduction reaction [15]. Also, it has been proposed that hydrogen or oxygen permeating through catalyst layer may react and also produce peroxide species [29]. As the electrolyte membrane is consumed, the chemical failure of the membrane will cause membrane thinning, release of fluoride ions, increased gas crossover, and voltage degradation. These four main observations are commonly used to identify chemical degradation of the membrane. They are inter-related in a cycle of chemical degradation as shown in Figure 2-8 [4].

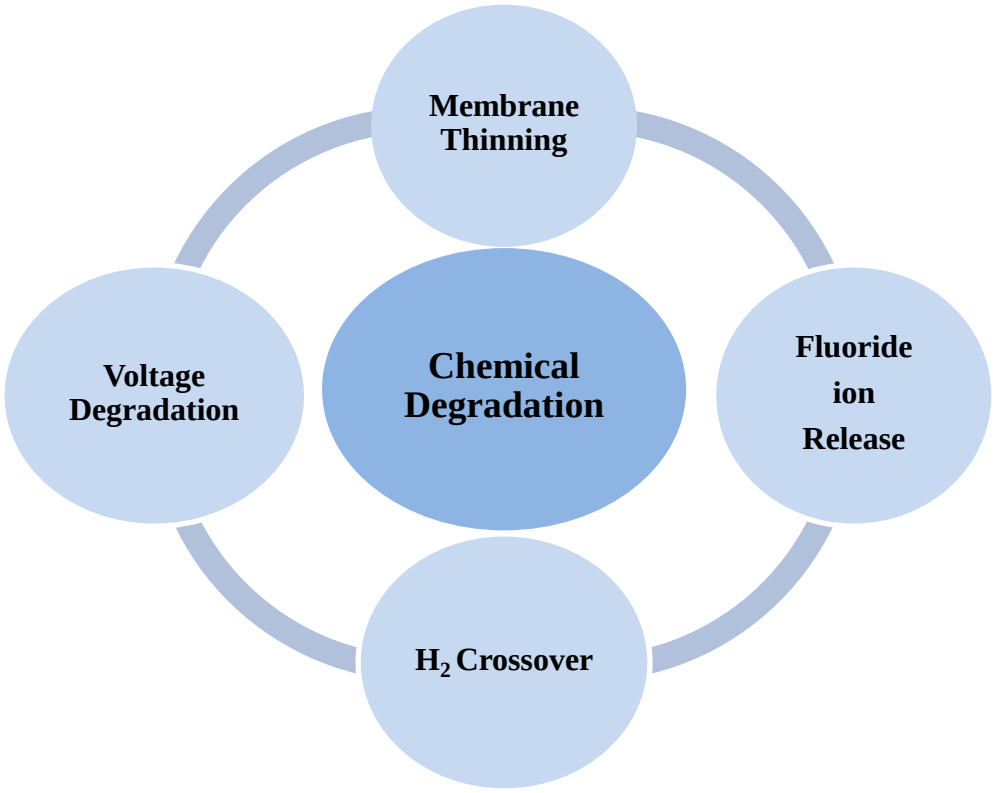

Figure 2-8. Chemical degradation cycle in a PEM fuel cell.

2.4.1.1 Membrane thinning

Observation of membrane thinning is a suitable method to evaluate membrane degradation. The degradation occurs when the membrane is consumed during the fuel cell operation [5]. The membrane thinning can be measured once the fuel cell is dismantled. Scanning electron microscope (SEM) is often used to characterize the morphology of the membrane as well as to measure the membrane thickness. However, the SEM only provides little information into where degradation occurs. It is still hard to distinguish whether the degradation occurs close to the anode or the cathode side [11, 30]. Also, one cannot measure or identify membrane thinning in-situ with respect to an assembled fuel cell.

2.4.1.2 Fluoride ion release

Second observation is the release of fluoride ions in effluent water streams. Measurement of fluoride emission rate (FER) is an alternative method to study the membrane degradation mechanism. As the PFSA membrane is degraded, HF will release as a degradation product and may exit the fuel cell in the effluent water. Most studies have observed the fluoride ion release as a function of time. Measuring the FER from the anode and cathode are the most common way for identifying where the side of degradation is. Even though it is still ambiguous where the most fluoride comes from, many literature studies have found the side where most of the fluoride is released, is related to the side where degradation is predominant [31-33].

The formation of a Platinum (Pt) band has believed to be related to the FER. The Pt band consists of several Pt particles that can be formed by an agglomeration of Pt nuclei. It is found that the location of the Pt band correlated with the magnitude of the FER. The location of Pt band is normally observed at the electrolyte layer either anode or cathode of the membrane. Changing hydrogen and oxygen inlet partial pressures can change the Pt band location. The deposited Pt in the membrane can be observed using SEM. Recently, many studies have investigated the degradation behavior of the MEA by correlating the

location of the Pt band on the electrolyte layer to the side that most of the fluoride is released [31-32].

2.4.1.3 Hydrogen crossover

Hydrogen crossover rate is the third observation used as a measure of the chemical degradation in the membrane. Permeation of reactant from one electrode to the other through the membrane is referred to as crossover. Although crossover of both hydrogen and oxygen occurs, the oxygen crossover generally occurs at a lower rate and thus most often the hydrogen crossover is of interest [34].

Hydrogen crossover is an important factor related to the reduction in fuel cell performance, efficiency and durability. Through a mixed potential, hydrogen and oxygen reactions at the cathode will decrease the cell's OCV. Crossover and internal short circuits impact fuel cell efficiency. The efficiency is lowered because although the reactant is consumed, the electrical work is not captured. The crossover of one hydrogen molecule results in loss of 2 electrons. It is the loss occurred from conducting the 2 electrons from the anode to cathode. From the studies, the hydrogen crossover of 1 mA cm^{-2} equates to a loss in current efficiency of 0.25% at an operating current density of 400 mA cm^{-2} [8, 34, 35].

A condition of severe crossover can accelerate membrane degradation including hot-spot/pin-hole formation via locally generated heat. Clearly, if hydrogen and oxygen are allowed to combine directly and 'combust', heat will be generated. The rate of hydrogen crossover can be determined by Faraday's law in a controlled crossover test. The hydrogen's permeability through the membrane or the crossover current density, i_{H_2} (A cm^{-2}), is related to the actual molar flux of hydrogen permeating through the membrane, N_{H_2} (mole cm^{-2} s^{-1}), as expressed in the following equation (Equation 2-6) [4].

$$N_{H_2} = \frac{i_{H_2}}{2F}$$ Equation 2-6

where F is the Faraday constant (96485 C (electron-mole)$^{-1}$).

In addition, a given hydrogen reactant is a function of the membrane composition, membrane microstructure, and membrane thickness. A PEM fuel cell with a thin membrane will result in higher crossover current than a thick membrane. According to Fick's law, Equation 2-7, exhibits that a decrease in membrane thickness will result in an increase in hydrogen crossover rate [4]. The concentration gradient of the reactant across the membrane is the driving force of the crossover current [36, 37].

$$N_A = \frac{P_M(p_I - p_{II})}{\delta}$$ Equation 2-7

where N_A is the flux of the gas species across the membrane of thickness (δ). P_M is the membrane permeability, and p_I and p_{II} are the partial pressures of the reactant gases on either side of the membrane.

Overall, once the hydrogen crossover begins, a destructive cycle of increasing gas crossover commences, and there is the potential for pinhole formation. This will cause an acceleration of the membrane degradation, lead to the dramatic decay of fuel cell performance, and then quickly lead to a complete failure of the fuel cell.

2.4.1.4 Voltage degradation

Voltage decay rate is also a good indication of the membrane durability study. Voltage drops are normally caused by both electrolyte membrane and catalyst layer degradation [38]. The catalyst layer is a porous reaction zone composed of a mixture of ionomer and carbon-supported platinum particles, which are adhered directly to surface of the

membrane. The ionomer phase allows protons to reach the reactive sites, while the carbon particles provide pathways for electrons. Reactant gas enters into the catalyst layer through the pores, while product water, both vapor and liquid, leaves through the same pores.

As operating time passes, membrane thinning will start to occur due to the loss of materials in the polymeric structure of the membrane. The membrane thinning will accelerate the hydrogen crossover rate and cause the drop in cell voltage [4]. Since the voltage degradation will further result in loss of an overall fuel cell performance, dramatic change in voltage degradation slope is a good estimation of when a severity of the fuel cell failure will occur [5]. This work will focus on fuel cell durability with respect to membrane, and not degradation of the catalyst layer by platinum sintering/dissolution and carbon-support oxidation. During the experiment, the decay of voltage is observed by plotting the cell voltage at a constant current density of 10 mA cm^{-2} versus degradation time.

2.4.2 Mechanical failure

A wide range of studies addressing mechanical issues of membranes have emerged in the last few years. Mechanical failure can occur when the fuel cell is exacerbated by cyclic stresses and strains during relative humidity cycling. As numerous pores, cracks and pinholes are formed, gas crossover across the MEA increases. A pinhole may also form when a membrane thins to the point where crossover can cause a burn-through in a very specific location. The gas crossover and the pinholes can lead to localized heating of the membrane and result eventually in catastrophic failure of the fuel cell [5, 39, 40]. The cyclic stresses and strains on the membrane are mainly caused by compression force, pressure differential force, shear force, and swelling force as shown in Figure 2-9 [4].

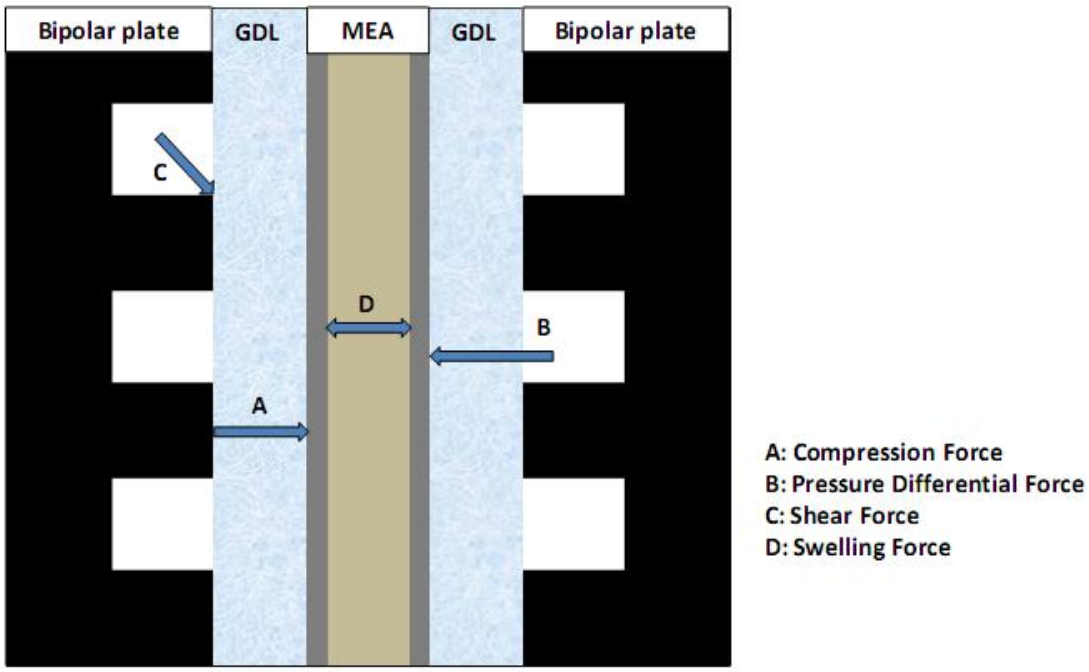

Figure 2-9. Cyclic stresses and strains on the membrane caused by compression force, pressure differential force, shear force, and swelling force in a PEM fuel cell.

2.4.2.1 Compression force

Compression force on the membrane can lead to mechanical failure since a total cell compression is given as an overall pressure on the fuel cell. The cell requires an appropriate cell compression to fix the cell hardware. In order to achieve a good fuel cell performance, selecting a suitable cell compression is important. An insufficient compression will result in improper sealing (leaking between cells or out of the cell itself), and high electrical contact resistances between the cell components. An excess compression can also damage the cell components including flattening of the GDL, destroy of its pore structure, and increase of the stress in localized areas of the membrane [40, 41].

2.4.2.2 Pressure differential force

Forces due to pressure differentials across the membrane are normally controlled to be minimal. The fuel cell is generally operated with anode and cathode partial pressures equal to each other (within 10-20 kPa). However, there are some exceptional instances where large pressure differentials across the membrane can happen. For example, in actual stack operation, different stresses may result in lag time response of reactive feed system such as turbo-chargers on the cathode, and situation of rapid current transitions where hydrogen feed and recycle systems can not respond. Under an operation of polarization curve at high current densities; a large difference between anode and cathode partial pressures can be obtained. The difference in partial pressures will become the pressure differential force across the membrane thickness. Huang and Yoon [42] indicated that an unsteady pressure differential force is related to the platinum band formation. The occurrence of the platinum band is responsible for an increase in H_2O_2 formation and will later accelerate the membrane decomposition [32].

2.4.2.3 Shear force

According to a symmetric geometry of the constrained fuel cell hardware, shear effect is usually not expected to occur inside the fuel cell. However, point-to-point variations in temperature and hydration of the membrane are unavoidable. These two effects will thus create shear force on the membrane material. Current density differential over the area of the MEA will lead to differential heating of the MEA. Also, the membrane tends to have high water level near the outlet of the flow channels as a result of water production when the reactions take place. The maximum values for total strain are near the more hydrated edge of the membrane. The strain developed in the plane of the membrane in the constrained configuration could raise wrinkling issues in the membrane near the edges during fuel cell operation. Creation of a hole in the membrane can possibly be considered as the extreme form of non-uniformity. This non-uniformity of the membrane will induce shear force in the plan of the membrane. This shear force exists when the fuel cell

materials tend to slide across each other in parallel to their interfaces. The slightly movement of the fuel cell materials will finally reduce the membrane integrity [17, 43-45].

2.4.2.4 Swelling force

Under humidified conditions, imbibe water can cause membrane swelling. The membrane swelling force increases stress on the membrane and induces plastization of the membrane that makes the creep issues more prevalent. Unconstrained PFSA membranes will expand with hydration 10-15% in the axial direction, and 20-30% through the thickness of the membrane [44]. Nafion^{TM} membrane, as a polymer, demonstrates time-dependent behavior such as creep and stress relaxation. Creep issue is observed when there is a dimensional change in length of the membrane material over time at an applied force. Water, absorbed by polymer membrane, has been recognized as a plasticizer, which will soften the membrane material and reduce the load carrying capability [43, 44].

Solasi et al. [43] has shown that stress relaxation of the Nafion^{TM} membrane is highly influenced by introducing water in the MEA structure. They suggested that any studies of visco-elastic/plastic model for the Nafion^{TM} should consider hydration effects in the stress model. Benziger et al. [46] proposed that membrane swelling and relaxation processes work as an interfacial contact between the membrane and the catalyst layer. In this case stress relaxation causes the extruded membrane into the electrode to slowly relax and stretch out in the plane of the membrane which later causes the catalyst/membrane delamination. The membrane swells/shrinks to a great extent when exposed to hydration or relative humidity (RH) cycles. Membrane expansion and shrink tension induce stress cycles in the membrane during fuel cell operation [3]. Changes in dimension with the RH effect are found to be orders of magnitude bigger than expected from changes in temperature. This change in the RH is equivalent to mechanical load and it is believed to be a driving force that accelerates the mechanical failure in the fuel cell system [44, 47].

2.5 Relative Humidity

The requirement for hydration of electrolyte membrane means that RH levels of the reactant streams have effects on PEM fuel cell performance. Reducing RH limits the electrode kinetic reactions and increases the membrane resistance inside the fuel cell [3]. Proton conductivity of the membrane and performance of the fuel cell will rapidly decrease when the water content of the membrane decreases, especially if operated with dry reactant gases [48, 49].

2.5.1 External Humidification

To maintain proper membrane humidity, many studies have operated the fuel cell using an external humidification. The external humidification can be achieved by humidifying the incoming reactant gases through a water reservoir or a humidifier. The humidification process will totally or partially saturate the reactant gases with water vapor before entering the fuel cell [23, 50, 51]. A bubble humidification scheme is one type of an external humidification that has been widely used in laboratory environments. In this scheme the reactant gases are bubbled through the humidifier [52].

Recently, a modified bubble humidification was studied by Vasu et al. [52]. In this work, the conventional bubble humidifier was modified to become a continuous bubble humidifier for a better operation in a fuel cell system. Their proposed design showed that the continuous bubble humidifier could maintain high membrane humidity at a constant RH value. By using stack coolant water recirculation, the continuous bubble humidification had some advantages over the conventional bubble humidifier. As such, it could control the RH at a desired value, and there was no liquid carry-over at high gas flow rates and no water vapor condensation at the stack inlet and humidifier exit channel. It was also found that the power output of this continuous bubble humidifier achieved 6-19 % enhancement in stack efficiency.

External humidification, however, has some drawbacks. A significant cost and an overall weight of the humidification subsystem can obstruct the development of portable and

automotive fuel cells. Self-humidifying membrane is thus designed as an alternate option [53, 54].

2.5.2 Self-humidification

By using various preparation methods, many researchers [48, 49, 53, 55-59] have focused on fabrication of a novel self-humidifying membrane. From their studies, the self-humidifying membrane could improve the fuel cell performance without increasing an area of the catalyst layer or the catalyst loading. The performance of the PEM fuel cell was enhanced by showing an increase in the cell voltage and the current density under dry conditions. Also, the self-humidifying membrane could facilitate and help in balancing the water movement and the proton conduction inside the membrane. However, excess water produced at high current densities has the potential to fill channels in the gas diffusion layer and inhibit mass transfer. Contact with liquid water can 'swell' the polymeric membrane, and thus change in hydration levels in the membrane can also create mechanical stresses. The water management within a fuel cell is a complex phenomenon that must be carefully managed.

Some studies [37, 48] therefore synthesized an ultrathin self-humidifying membrane to solve the water management problems. The ultrathin self-humidifying membrane was fabricated to accelerate water back-diffusion from the cathode to the anode. The water back-diffusion could satisfy the need of water at the anode side and meet the requirement of electro-osmotic drag from the anode to the cathode. Also, the thin membrane provided a better water balance compared with a thick membrane. The ultrathin self-humidifying membrane, however, requires some additional membrane preparation steps and usually causes the crossover of the reactants. A very thin membrane could easily lead to a mixed potential and later generate some unsafe problems. The heat generated from the electrochemical reactions combined with the crossover gasses could easily create hot-spots or form pinholes. Overall, it could accelerate the membrane degradation and lower the cell performance. The operation of without humidification may be possible, however for automotive applications (which required higher power densities) the durability and

performance of such membranes have yet to be demonstrated, and thus humidification of the reactant streams remains a reality.

2.5.3 Operating under Low Humidity

A PEM fuel cell system for automobile is generally exposed to low RH (i.e. below 100%) and load cycle conditions. To fundamentally understand the mechanisms of membrane degradation, several studies have examined the degradation mechanisms of the PEM membrane electrode assembly (MEA) under low humidification conditions. At low RH operating conditions, an acceleration of membrane degradation was identified whereas no significant membrane degradation was observed under saturation humidification conditions [3, 60, 61].

By operating a three-cell stack for 1000 hours, Wahdame et al. investigated the impact of low humidity conditions on the PEM fuel cell performance. Using both polarization curve and EIS measurement, they found that high internal resistance under low RH conditions could reduce the stack lifetime expectancy and increase the probability of cell failure [62]. Under low RH conditions, in situ measurements were also conducted by Yu et al. [19, 63]. Using a single PEM fuel cell, polarization curves, hydrogen crossover rate and electrochemical active surface area (EAS) of Pt catalyst were measured. During the operation, there was an accelerated increase in the hydrogen crossover and decrease of the EAS of Pt catalyst. These effects would later cause the decay in voltage and loss in overall cell performance. To ascertain hydroxyl or hydroperoxyl radical generation in the MEA, Endoh et al. performed electron spin resonance (ESR) studies. The catalyst layer of the degraded MEA was observed via the ESR. The results showed that the radical formation under a low humidity could accelerate the MEA degradation [60].

At various humidification levels, Guvelioglu et al. studied the cell performance via hydrogen and air flow rates. Under low RH conditions, the membrane was not properly hydrated resulting in low membrane conductivity and poor membrane life. The RH of the hydrogen and the air as well as their flow rates is critical for the reliability of the

membrane. To prevent membrane dry-out and flooding, the RH and the reactant flow rates are necessary to be controlled [50].

For a long-term operation, a homogeneous reaction distribution inside the fuel cell is also required. Under low humidified conditions, Yoshioka et al. have designed and constructed a cell current measuring distribution system to analyze the stability of PEM fuel cell performance. The cell current measuring system could give information on the change of current density at different location for an entire fuel cell plate. They found that the region of maximum current was localized near the cathode outlet where the membrane had relative high water content. Whereas, the membrane near the cathode inlet was observed to dry-out. The local cell resistance near the cathode inlet was therefore higher than that near the cathode outlet. These were believed to be responsible for the fact that evaporation rate occurred faster than the cell reactions. For the anode side, current density near the anode inlet and outlets declined after 250 hours of operation. The decrease in the current density at the anode was considered to be caused by osmotic water drag. The information achieved from the cell current measuring distribution system was useful for the development of the MEA and the PEM fuel cell design [64].

In addition, a highly durable perfluorinated polymer based MEA was fabricated by Endoh [65]. They found that even operated the PEM fuel cell at a low RH, this new MEA demonstrated a significant strength of its structure than a conventional MEA. It could achieve a good durability and had a long-term operation over 4000 hours at high temperature (120 °C). For economical commercial PEM fuel cell applications, however, cost and lifetime of the cell have to be considered. Adding more catalyst or some other materials could increase the fuel cell lifetime but it also increases the cost. Thus, the cost and lifetime performance of the fuel cell should be balanced. Currently, most researchers have mainly studied on the lifetime of the PEM fuel cell applications. They believed that if the factors that have a significant effect on the fuel cell failure are clearly understood; the fuel cell's lifetime could be enhanced without losing fuel cell performance and increasing cost.

2.5.4 Operating with Dry gases

Operating a PEM fuel cell with completely dry reactant gases is also another option. Under dry gases conditions, it is found to have some advantages over the humidified conditions [26]. For examples, no gas humidification subsystem is needed, the removal of water in vapor form reduces the amount of heat to be removed from the cell, and less condensed water present in the fluid flow channels for the gases in the bipolar plates and GDLs enhances the fuel cell performance [25]. According to the advantages of using dry gases, some researchers have focused on operating a PEM fuel cell with completely dry reactant gases. Results show that operation under such conditions is feasible [48, 53, 54]. With a higher current density, more water is produced on the cathode side and the water back-diffusion effect (water moving from cathode to anode) prevails over the electro-osmotic effect (water moving from anode to cathode), so the cell can be sufficiently humidified to continue and complete the necessary electrochemical reactions [55].

Buchi et al. [54] experimentally operated the PEM fuel cell with dry gases for up to 1800 hours. They investigated the water distribution inside the cell by measuring the amount of product water on the anode and cathode sides. It was found that the back-diffusion of product water is a dominant process for water management in the cell. The back-diffusion water could allow internal humidification preventing drying-out of the membrane. With various reactant humidification levels, Williams et al. [53] performed the experiment at dry and fully humidified conditions. The results showed that cell temperature, pressure gradient between the anode and cathode compartments, anode and cathode stoichiometries had a strong influence on the cell performance under dry conditions. In addition, from the product water calculation, the water back-diffusion produced from the cathode could be able to keep the cell humidified at temperature up to 70 ºC which agreed with the work of Buchi et al. [54].

However, at low current densities, both water back-diffusion and electro-osmotic effects are limited, indicating that the electrolyte membrane might not be sufficiently humidified for the ions to pass through it [2, 17, 18, 20 , 21]. Under dry conditions, an accelerated rate

of membrane degradation could be observed by voltage degradation curve and crossover test. Williams et al. [53] found that using dry cathode inlet while maintaining humidified anode inlet, there was only 5% or 33 mV at 400 mA cm^{-2} (at anode/cathode stoichiometries of 3/4). Whereas, operating dry inlet gases for both anode and cathode resulted more significant loss in cell performance up to 29% or 193 mV at the same current density.

With an intention to improve the performance of the PEM fuel cell using dry reactants, a thin double-layer composite membrane consisting of one layer of Pt/C catalyst dispersed recast Nafion and another layer of plain recast Nafion was investigated by Yang et al. The Pt/C catalyst particles used in the membrane could provide the sites for the catalytic recombination of H_2 and O_2 permeating through the membrane from the anode and cathode to produce water. The water generated could directly humidify the membrane and allow the operation with dry reactants to be possible [48].

Qi and Kaufman [26] designed a double-path-type flow filed channel which had two gas inlets and two gas outlets. The two paths of one inlet flow field were adjacent to the outlet of another flow field. In this way the dry inlet gas could be able to become hydrated by acquiring some moisture from the moist outlet gas. They found that this type of flow field effectively used the product water to hydrate the membrane and the catalyst layers. Under dry conditions, the fuel cell could run stably at a current density up to 330 mA cm^{-2}.

2.5.5 Operating under Relative Humidity Cycling

As fuel cells in certain applications (e.g. automotive) can be subjected to frequent start-stop cycles, prolonged idle conditions, and frequent current cycling due to variation in the demand of power from the overall power demand cycle [11]. Change between low and high power during the transition states could affect the integrity of the cell. During high RH conditions, the ionomeric membrane could swell because of an increase in water uptake. This could lead to compressive stresses in the membrane and result in yield tensile residual stresses during drying. The generated stresses were believed to be a major cause

of the mechanical failure of the membrane [66]. From the recent studies [16, 44], it was found that during drying conditions there was a dimensional change (or strain) of the membrane induced by constrained drying of the MEA. In addition, fluctuations in RH can lead to pinhole formation. When the pinhole is formed, it accelerates the chemical degradation inside the membrane [67].

Currently, RH cycling operating test has become an interesting test to study the PEM durability of the fuel cell. In this work, accelerated durability testing to study different modes of membrane failure via relative humidity cycling under idle conditions is performed. Under idle conditions, the fuel cell is operated at a low current density, so a low chemical degradation rate and minimal electrical load stress are expected. Catalyst degradation is also minimized. Note that, although idle conditions will minimize chemical and catalyst degradation, these two degradation modes will still occur to some extent. Both open circuit conditions and high current density operation have shown to be associated with accelerated chemical degradation of the membrane [4]. However, under RH cycling the membrane is anticipated to degrade by an additional stress from membrane swelling/contraction cycle controlled by RH.

CHAPTER 3: EXPERIMENTAL

3.1 PEM Fuel Cell Test Station

Fuel cell experiments were conducted using a single TP50 fuel cell (Tandem Technologies) with an active area of 42.25 cm^2. The graphite plates contained serpentine path flow channels as shown in Figure 3-1. The flow channels of the cathode and the anode plates differed in that those of the former were wider and deeper than those of the latter to increase the cross-sectional area for reactant diffusion. Although the flow path in this cell may not be optimized for performance, this cell was quick and easy to assemble, providing uniform compression, and flow path with well understood performance.

(a)

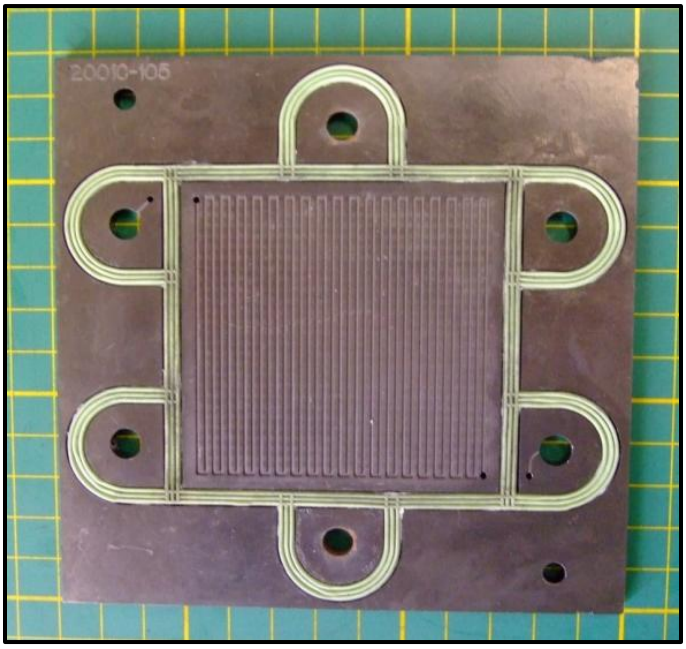

(b)

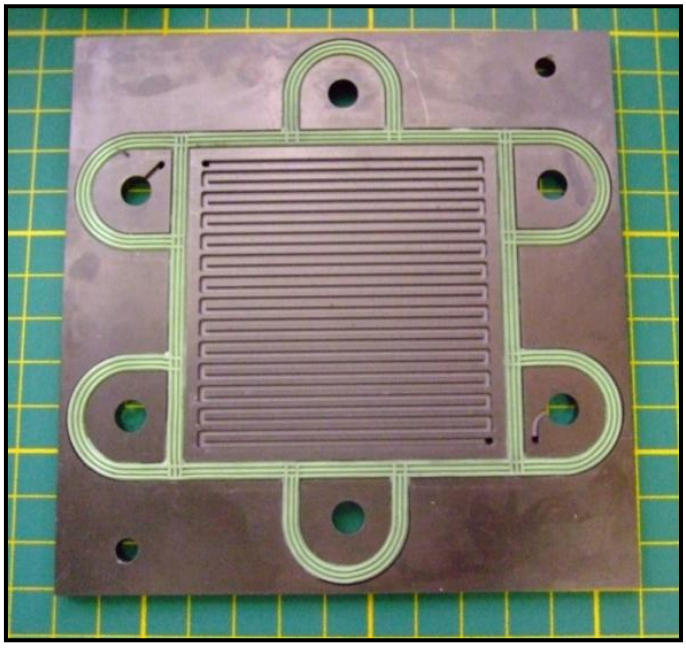

Figure 3-1. Pictures of a 42.25 cm^2 active area graphite bipolar plates with serpentine flow path of (a) anode bipolar plate and (b) cathode bipolar plate.

In this work the cells were assembled using catalyst coated membranes (CCM) and SGL gas diffusion layers (GDL) with microporous layers (MPLs). MPL is a composite of carbon particles and a hydrophobic agent, which is coated on one side of the conventional gas diffusion media and can be used on one or both of the anode or cathode electrodes. The electrolyte membranes contained ePTFE reinforcement layers, as shown in the figure below, which increases mechanical stability of the membrane. The reinforced catalyst coated membrane used in this study consists of several layers. In Figure 3-2, a scanning electron microscope (SEM) image identifying 5 main layers of a Gore™ CCM is shown. The reinforcement layer is a porous ePTFE membrane and is discussed in the literature [68]. Since this layer bisects the electrolyte membrane, the electrolyte close to the anode will be referred to as the anode electrolyte and the electrolyte close to the cathode will be referred to as the cathode electrolyte.

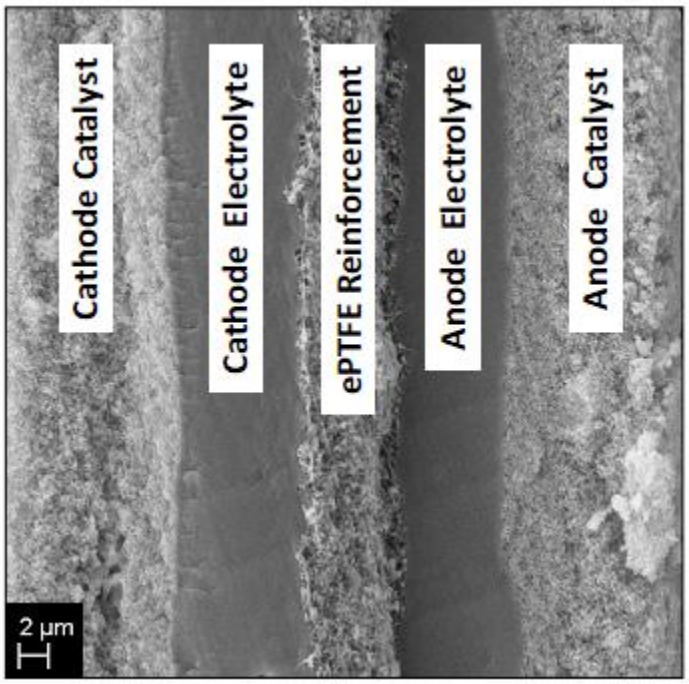

Figure 3-2. Gore reinforced catalyst coated membrane using PFSA for the anode and cathode electrolyte layers and an ePTFE reinforcement layer at the centre.

Gore^{TM} 57 CCM with an overall thickness of 50 µm and a membrane thickness of 25 µm were used. The catalyst loading for both sides was 0.4 mg cm^{-2}. The MEA was assembled using a 150 µm Kapton gasket sandwiched the membrane in the middle and 35 BC SGL gas diffusion layers GDLs were placed on either side as can be seen in Figure 3-3. The Kapton reinforced the CCM so the MEA did not tear at the edge.

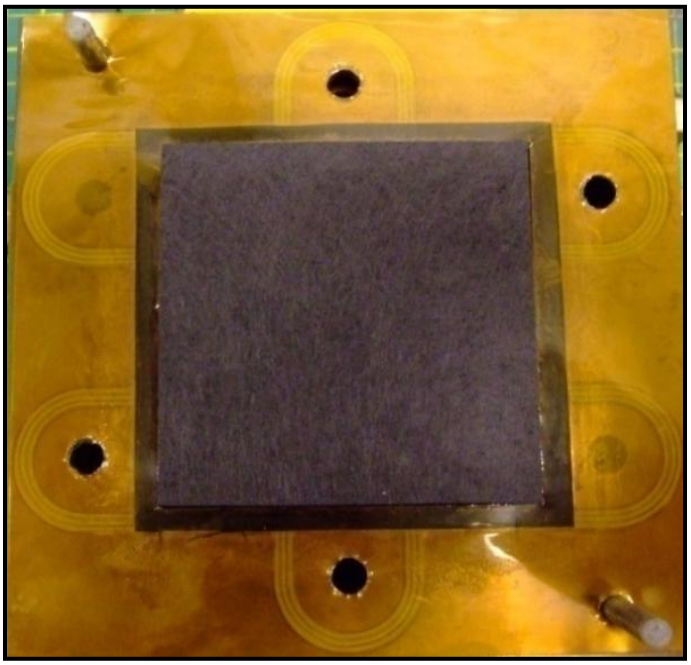

Figure 3-3. Fresh membrane electrode assembly (MEA) and gas diffusion layers (GDLs) with an active area of 42.25 cm^2.

The TP50 fuel cell and a G50 test station were used to investigate RH effects on PEM fuel cell performance. The test station consisted of several parts, as shown in Figure 3-4. Hydrogen and air were supplied as reactant gases to the anode and cathode sides, respectively. The gas lines to both sides were also connected to a nitrogen tank, allowing the system to be purged with nitrogen gas during electroanalytical tests (i.e. linear sweep voltammetry).

(a)

(b)

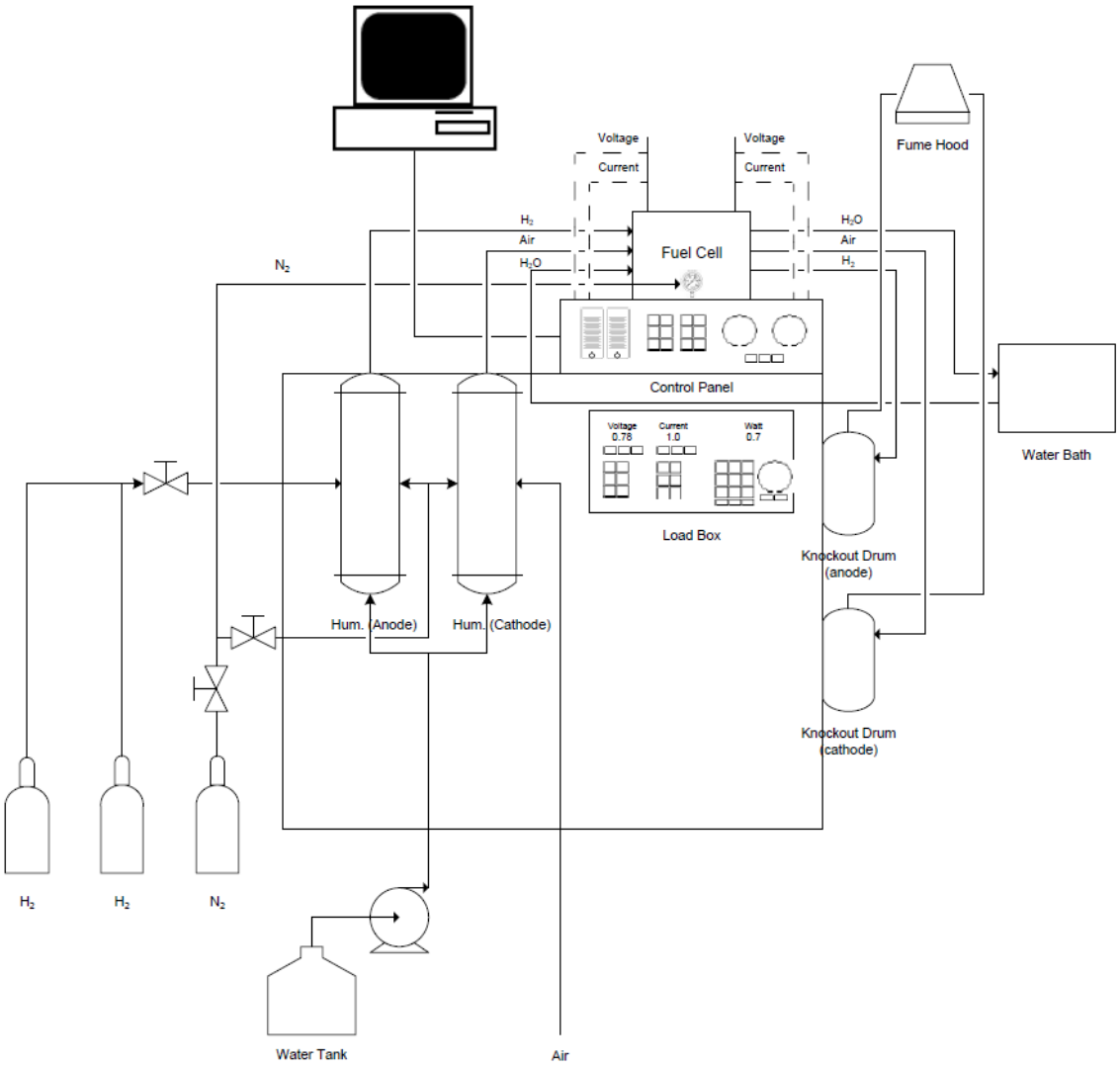

Figure 3-4. G50 PEM fuel cell test station used in this work: (a) Photo and (b) Schematic.

The fuel cell hardware was first compressed using nitrogen gas at 100 psig. Next, a water bath was used to heat the fuel cell to 70 ºC and maintained at that temperature. The reactant gases flowed through Bronkhorst EL-flow meters and pressure transducers before entering the humidifiers. External humidifiers were used in this system to keep the gas streams hydrated before entering the fuel cell so that the flowing gases would not dry out the MEA. A LabView control system and TDI load bank were used to control the load. Figure 3-5 shows screenshot of (a) the control panel and (b) the fuel cell process diagram

of the LabView data acquisition software. By changing the current set points via LabView program, the load could be changed and given in different cell voltages and power generations. At the outlets, the gases left the fuel cell carrying the water generated. Product water was collected in knockout drums that would further be used for fluoride ion release analysis.

(a)

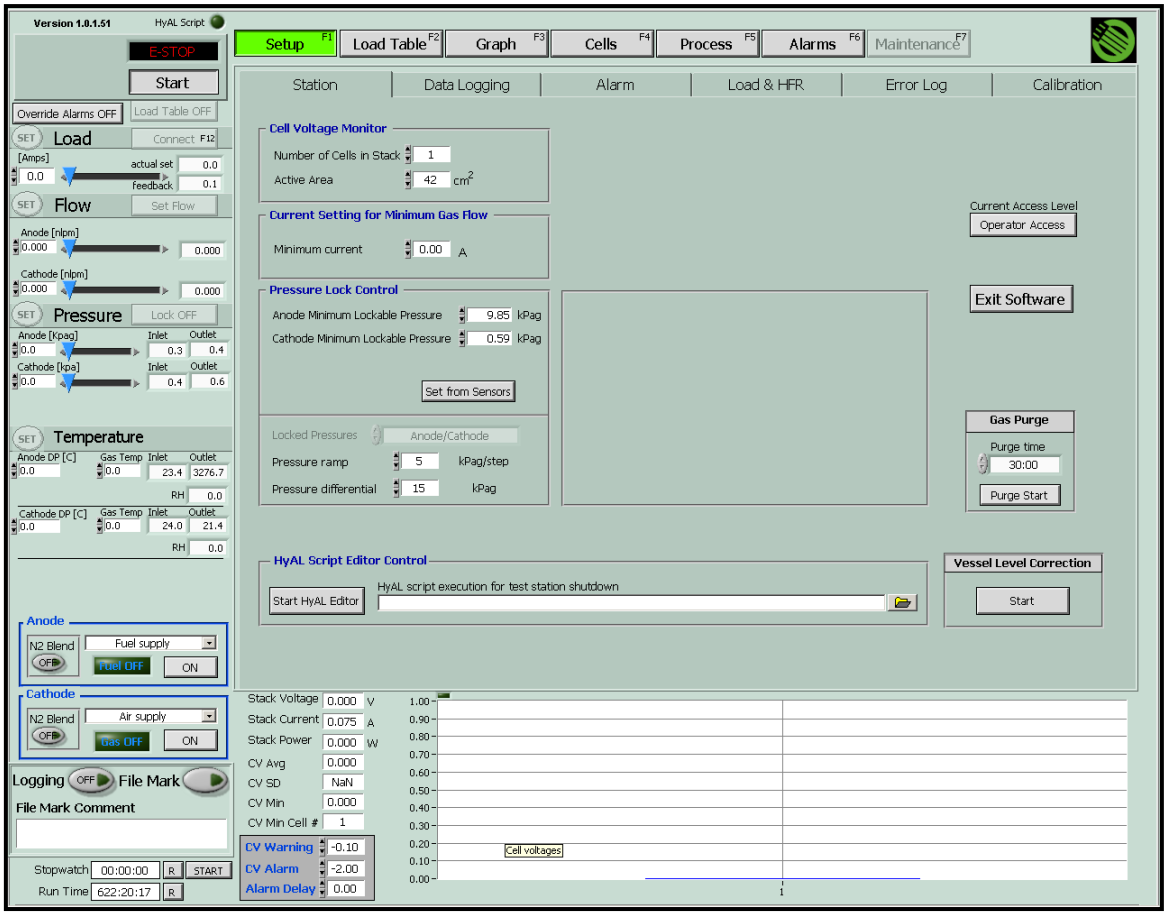

(b)

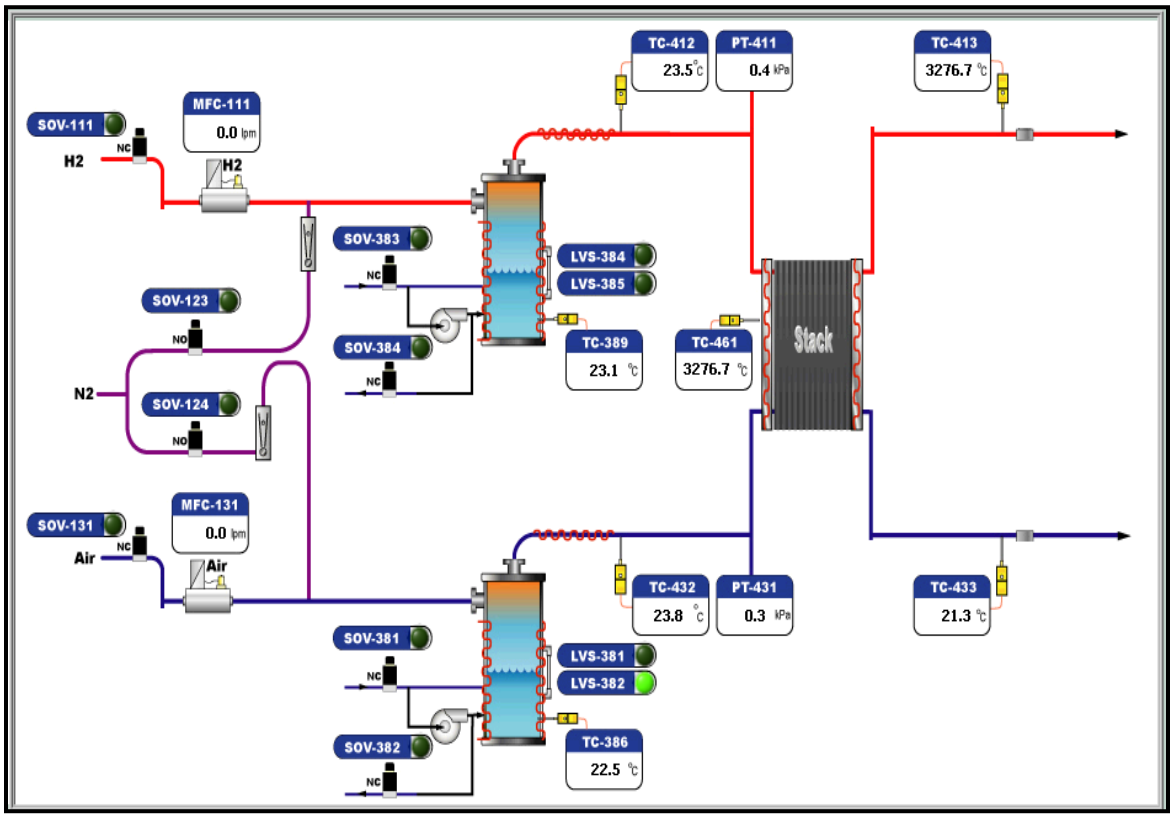

Figure 3-5. Screenshot of the LabView data acquisition software: (a) control panel and (b) process diagram.

Idle conditions at a 10 mA cm^{-2} constant current density were employed for this work. The test station was first used to perform a baseline cell polarization curve under high relative humidity (Run 1: 100% RH). The fuel cell was run at 70 ºC with either at constant 0.113 slpm and 0.358 slpm or stoichiometric flow rates at the stoichiometric ratio of 1.5 and 2.5 for hydrogen gas and air, respectively. The hydrogen gas and in-house air were both set at 100 psig. At the beginning of the cell's life, commissioning processes were carried out, including leak testing, crossover testing, and break-in of the fuel cell. Commissioning was conducted to ensure the cell had no leaks and to allow the cell to warm up and become fully hydrated in order for the chemical reactions to occur.

For the H_2-air RH cycling cell (Run 2), the same conditions and commissioning processes were applied. However, instead of the reactant gases passing through the humidifiers before entering the fuel cell, the gases were supplied directly to the cell for dry reactant conditions. The test station was by-passed to enable dry gas passage using additional valves at both anode and cathode sides. In this case, the commissioning procedure was conducted for 120 hours. During RH cycling, the inlet gases were automatically alternated between dry and 100% humidified conditions every 10 and 40 minutes, respectively. A schematic design of the RH operation during H_2-air RH cycling is shown in Figure 3-6.

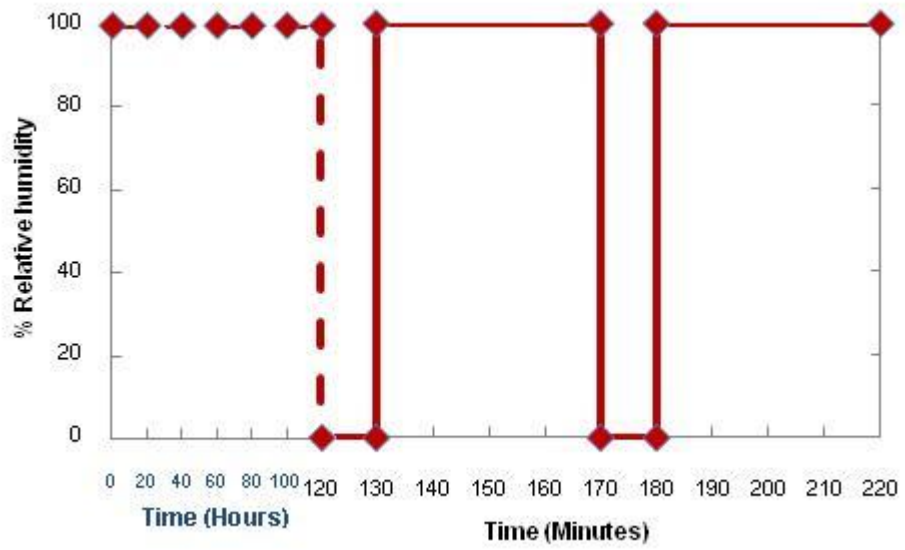

Figure 3-6. Schematic design of the RH operation during H_2-air RH cycling condition.

In addition, for H_2 RH cycling cell (Run 3), anode side of the reactant gas was manually RH cycled between dry and humidified states, while the cathode side was constantly supplied with a humidified gas. It is expected that anode side will be more dehydrated than cathode during dry operation, due to the electro-osmotic drag that move the water molecules from anode to cathode. Similar to Run 1 and Run 2, this H_2 RH cycling cell (Run 3) was also operated under the same conditions (i.e. current density, reactant flow rates). Throughout the experiment, hydrogen gas was alternated between dry and 100% humidified conditions for every 10 and 40 minutes, respectively. The 10 minutes (dry

state) and 40 minutes (humidified state) interval times were designed to conduct the same operation as the H_2-air RH cycling (Run 2) cell for a comparison.

During dry conditions, the hydrogen was controlled to flow through a mass flow controller and then directly fed into the fuel cell, whereas in-house air was provided as a humidified reactant through the humidifier. During the humidified conditions, the hydrogen and air flow were automatically controlled via a LabView program. The hydrogen and air flows were controlled by mass flow controllers, and passed through humidifiers before entering the fuel cell. The Process flow diagram of anode RH cycling cell (Run 3) bypass system is shown in Figure 3-7.

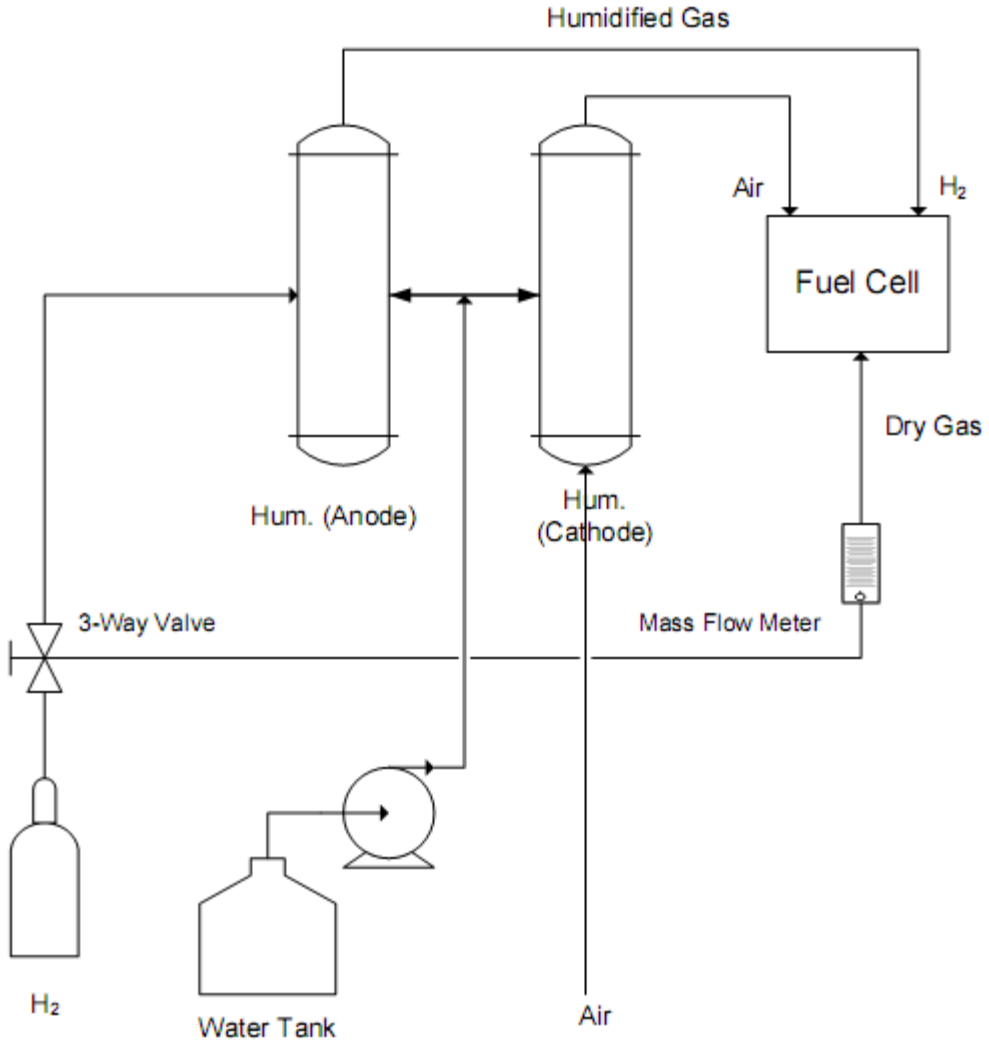

Figure 3-7. Process flow diagram of H_2 RH cycling cell (Run 3) bypass system design.

In this work, some membrane electrode assembly diagnostic methods were performed. In-situ diagnostic methods, including polarization curves, electrochemical impedance spectroscopy (EIS), and linear sweep voltammetry (LSV) were conducted. Also, ex-situ tests, such as ion chromatography, infrared (IR) imaging, and scanning electron microscopy (SEM) were carried out in order to investigate the MEA degradation mechanisms. These in-situ and ex-situ tests were performed periodically during and after the fuel cell operation.

As to be considered, safety issues regarding fuel cell operation is important. Since the PEM fuel cell uses hydrogen and air as the reactants, hydrogen leaks or a direct mixing of the hydrogen and oxygen are the most significant risks. The test station has a safety alarm to send a signal to the central control when there is a hydrogen leak. The alarm is a warning given by a small portable sensor which located above the station. When there is a leak of hydrogen, the orange light will turn on and within 3 minutes all the mass flow controls and the station will automatically shutdown.

3.2 Leak and Crossover Testing

As already mentioned about the safety issues of the hydrogen fuel cell test station, some prior diagnostic tests must be done before starting the test station. To ensure that there are no leak and crossover of the reactant gases; leak and crossover tests are conducted. The tests need to be performed every time a new fuel cell is re-assembled and before fuel cell starts up.

3.2.1 Leak Testing

Leak testing was performed by using a nitrogen gas. The nitrogen was firstly run though the system by clicking on ‘Purge Start’ button on the control screen (to deactivate the solenoid valve) and flow the nitrogen to the test station instead of the reactant gases. All fuel cell fittings and connections were checked by using a soap solution (‘Snoop’)

throughout the system. If bubbles are formed, then a leak is occurring at the location of the bubbles. If the leak occurs at a connection, the leak could usually be fixed by tightening the fittings or replacing them.

For leak testing of the fuel cell hardware, there are two different ways: individual and external leak checks. The procedure of each test is as follows:

3.2.1.1 Individual Leak Check

Before starting the leak check, the fuel cell was firstly compressed by the air to ensure that it was steady at 100 psig. For individual check leak the water line (Port A), connect another air line to Port A1 (water inlet), pressurized Port A1 to 20 psig and then plug Port A2. Port B1 (anode inlet) and C1 (cathode inlet) were individually connected to their own outlets as shown in Figure 3-8.

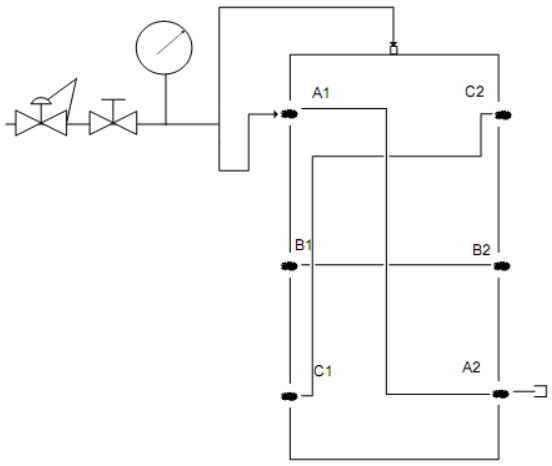

Figure 3-8. Basic circuit of the individual leak test.

Use leak check solution or soap solution to check leak at the sides and the fittings of the fuel cell in order to observe bubbles. If the bubbles emerge, then a gas-tight seal had not been achieved and the fuel cell gasket might have to be replaced. Pressure decay was observed for a minute during the test. For TP50 fuel cell hardware, the maximum pressure

decay allowed is 0.2 psig/minute. After the water line test was finished, all steps were repeated for anode (Port B) and cathode (Port C).

3.2.1.2 External Leak Check

Figure 3-9 shows basic circuits of the external leak test. Again, the fuel cell was compressed by the air to make sure that the bladder pressure was steady at 100 psig. Interconnect all the lines to check for the external leak as the following steps: connected the air to Port A1, connected A2 to B1, connected B2 to C1, and plugged C2. The leak problems could be observed again using the leak check solution or the soap solution. Pressure gauge was again used to observe the pressure decay (the same maximum allowed is 0.2 psig/minute).

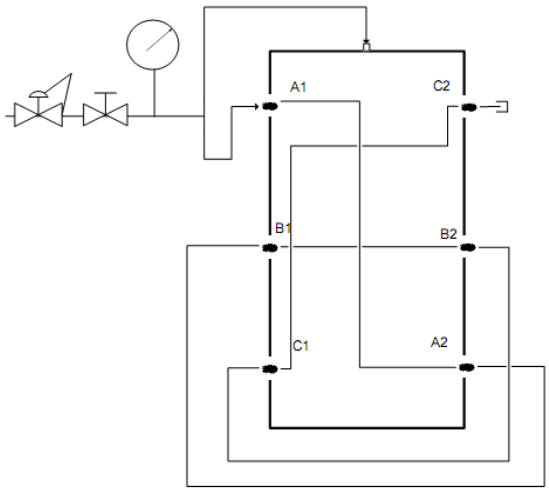

Figure 3-9. Basic circuits of the external leak test.

3.2.2 Crossover Testing

Reactants crossover can degrade fuel cell performance, efficiency and durability. The crossover test was performed before starting the test station. Once the fuel cell was compressed by air or nitrogen, hydrogen to air transfer check could begin as the following steps: connected the air to B1 and pressurized to 20 psig, connected tubing to C1 and

submerged it in a beaker of water, plugged Port B2 and C2, and connected the water line A1 to A2 (Figure 3-10a). If a bubble from the submerged tube in the beaker was seen, the fuel was crossing over. The MEA was unfit for use and it must be replaced. For the water to air transfer check and the water to hydrogen crossover check, all steps were repeated. All the connections were shown in Figure 3-10b and 3-10c.

(a)

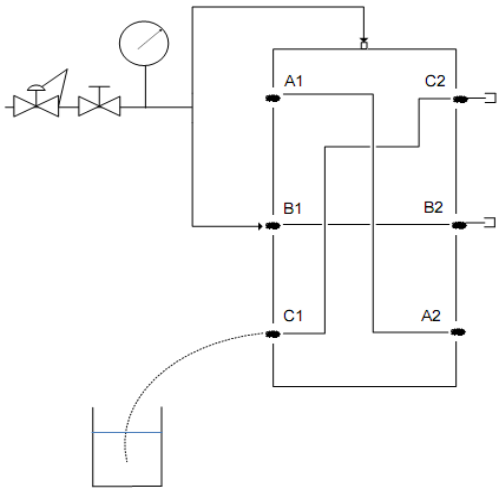

(b)

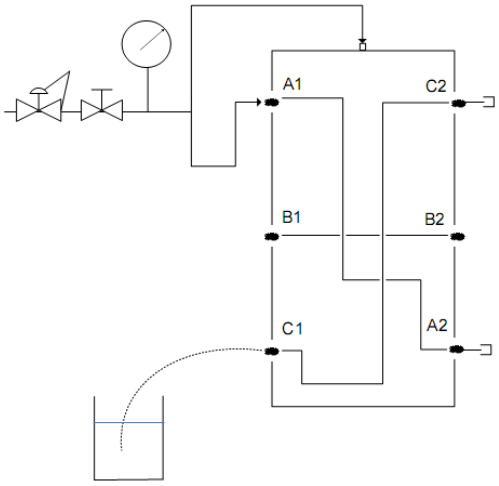

(c)

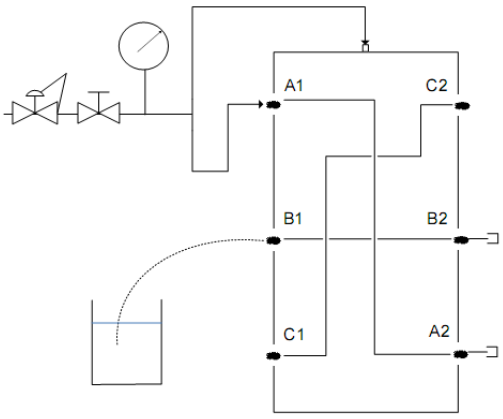

Figure 3-10. Crossover test: (a) Hydrogen to air transfer check, (b) Water to air transfer check, and (c) Water to hydrogen transfer check.

3.3 Commissioning of Fuel Cell

After a fuel cell was assembled, checked leak, and tested crossover, the fuel cell was operated for a commissioning period. The commissioning conditions were performed during the first 12 hours of the operation by the humidified reactant gases in order to activate the fuel cell. During the commissioning period, the cell was cycled by changing the potential from the OCV to the possible lowest potential and return back to the OCV for every minute. Then the cell was kept approximately at 0.6 V until performance was stabilized. The stoichiometries of anode and cathode were set constant at 1.5 and 2.5, respectively. The cell temperature was controlled to be stable at 70 ºC. Once the commissioning procedure was completed, the fuel cell test station was set at constant 10 mA cm^{-2} current density with H_2 and air flow rates of 0.113 slpm and 0.358 slpm, respectively, for 12 hours before the first baseline polarization curve was measured.

3.4 Polarization Curves

Polarization curve is normally used to observe an overall performance of fuel cell. During the polarization curve measurement, current and reactant flow rates were set by using the control panel via the LabView program. The procedures started by setting the current at an OCV which was at a minimum resistance on a TDI loadbox. There was a small increase in the current and then an adjustment H_2 and air flow rates followed by 1.5 and 2.5 anode and cathode stoichiometric ratio, respectively. The current and voltage readings were collected every 1 minute interval. The lowest voltage value achieved was approximately closed to 0.3 V. The details of the polarization curve procedure are described in Appendix C.

3.5 Voltage Degradation Curve

Voltage degradation curve was performed by plotting an average cell voltage versus a degradation time at a 10 mA cm^{-2} current density. Voltage degradation rates of different duration times were calculated from the slope. The degradation rates are used to compare a drop in an overall fuel cell performance between Run 1 (100% RH) and Run 2 (H_2-air RH cycling). The calculations of the voltage degradation rates are presented in Appendix D2.

3.6 Electrochemical Impedance Spectroscopy (EIS)

Electrochemical impedance spectroscopy (EIS) is considered to be a powerful technique for investigating electrochemical system, with its ability to distinguish in the frequency domain the individual contributions. The EIS is generally used to examine ohmic resistance, charge transfer resistance, and mass transport resistance of a PEM fuel cell. In the PEM fuel cell system, the electric circuit of the MEA is a combination of anode and cathode catalyst layers plus the membrane. The anode and cathode catalyst layers are treated as the electric circuit (capacitor) whereas the membrane is considered as a resistor. These three components are connected in series and served as a whole electrical equivalent circuit [69].

A typical impedance spectrum is usually plotted with real part of impedance against the imaginary part that gives a Nyquist plot as shown in Figure 3-11. The Nyquist plot is usually semi-circular: the intersection of the impedance data with the real part of the axis at the high frequency end gives the ohmic resistance and at the low frequency gives the charge transfer resistance. The diameter of the semi-circle is the kinetic loop. The relationship between the real (Z_{re}) and the imaginary (Z_{im}) impedances is expressed as follows [68, 69]:

$$|Z|^2 = (Z_{re})^2 + (Z_{im})^2 \qquad \text{Equation 3-1}$$

$$\emptyset = \tan^{-1}\frac{Z_{im}}{Z_{re}} \qquad \text{Equation 3-2}$$

$$Z_{re} = |Z|\cos\emptyset \qquad \text{Equation 3-3}$$

$$Z_{im} = |Z|\sin\emptyset \qquad \text{Equation 3-4}$$

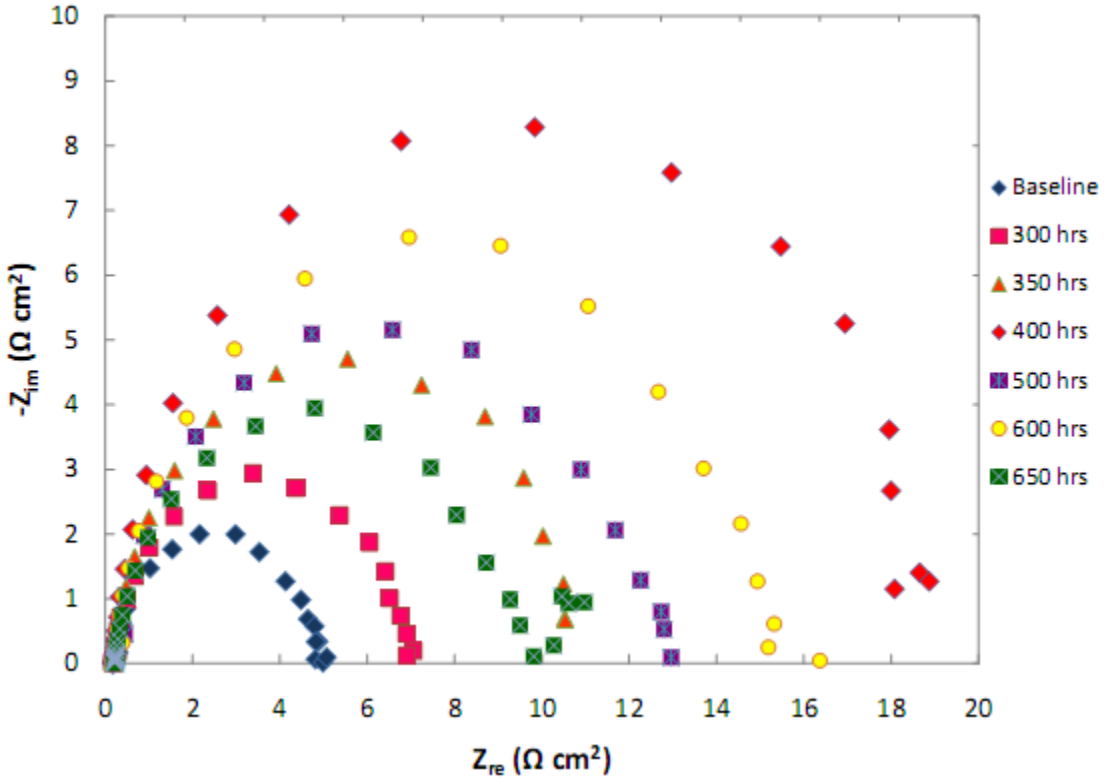

Figure 3-11. Nyquist plot of a single PEM fuel cell at different operating times. The cell with an active area is 42.25 cm^2, operated at 10 mA cm^{-2}, 70 ºC under humidified conditions. H_2 and air flow rates are 0.113 and 0.358 slpm, respectively.

In this experiment, the EIS was performed at 0.85 V (for Run 1) and at OCV (for Run 2 and Run 3) by using Autolab Potentiostat Model PGstat 30 with a frequency response analyzer (FRA) software. An AC impedance spectrum was measured in the constant-voltage mode by sweeping frequencies over the 0.01 – 10,000 Hz range and recording 65 points/decade. The modulating voltage was set at 10 mV.

Figure 3-12. Autolab Potentiostat Model PGstat 30 used to examine ohmic and charge transfer resistances and for a measurement of hydrogen crossover current of a single PEM fuel cell.

Autolab Potentiostat Model PGstat 30 used to perform the EIS and linear sweep voltammetry (LSV) measurement is shown in Figure 3-12. The LSV measurement will be later mentioned in the following section (section 3.7). For both techniques (EIS and LSV measurement), a four-electrode cell was used to analyze processes occurring within the electrolyte, between two measuring electrodes separated by an electrolyte membrane. The oxygen electrode and hydrogen electrode served as the working electrode and the counter electrode, respectively. The counter electrode was used as the reference electrode and the sensor electrode was connected at the oxygen electrode side to complete the process. The oxygen electrode (cathode reaction) was mainly focused and used as the working electrode since the anode reaction is significantly faster than the cathode side. The electrical circuit of the anode can be neglected and used as the reference. Therefore, the charge transfer resistance obtained through the AC impedance study primarily could be attributed to the oxygen reduction reaction (ORR) [69].

3.7 Linear Sweep Voltammetry (LSV)

An electrochemical test, a linear sweep voltammetry (LSV), was performed using AutoLab Potentiostat Model PGstat 30 with GPES software (Figure 3-12). Hydrogen crossover current was measured by the LSV technique. To experimentally determine the hydrogen crossover, nitrogen inert gas was used to purge the fuel cell cathode while hydrogen was passed through the fuel cell anode. The potential of the fuel cell cathode (i.e. the working electrode) was swept by means of a linear potential scan to potentials at which any hydrogen gas present at the fuel cell cathode was instantaneously oxidized under mass transfer limited conditions. At the potential higher than 0.4 V, H_2 oxidation current density is purely limited by the H_2 permeation rate [70]. The crossover current measurements were performed by scanning the working electrode versus the counter/reference electrode from 0.05 to 0.6 V with a sweep rate of 2 mV s^{-1}. Note that polarization to anodic potentials higher than 1 V can lead to irreversible damage of the fuel cell electrode resulting from carbon corrosion and catalyst oxidation [4].

The rate of hydrogen crossover from the anode to the cathode through the membrane is determined by an output of working electrode current density versus potential which is simply expressed by Faraday's Law (Equation 2-6) [8]. Typically, the current attains either a constant or linearly increasing value with increasing electrode potential. As the potential is increased, the constant current indicates that the cell still has high electrical resistance which means there is no internal shorting. Whereas the linearly increasing current shows that the cell has a finite resistance due to internal shorting. The hydrogen crossover measurement is a good diagnostic for membrane durability study. In this work, the crossover experiment was conducted periodically under humidified conditions. Figure 3-13 shows a hydrogen crossover measurement of a single PEM fuel cell.

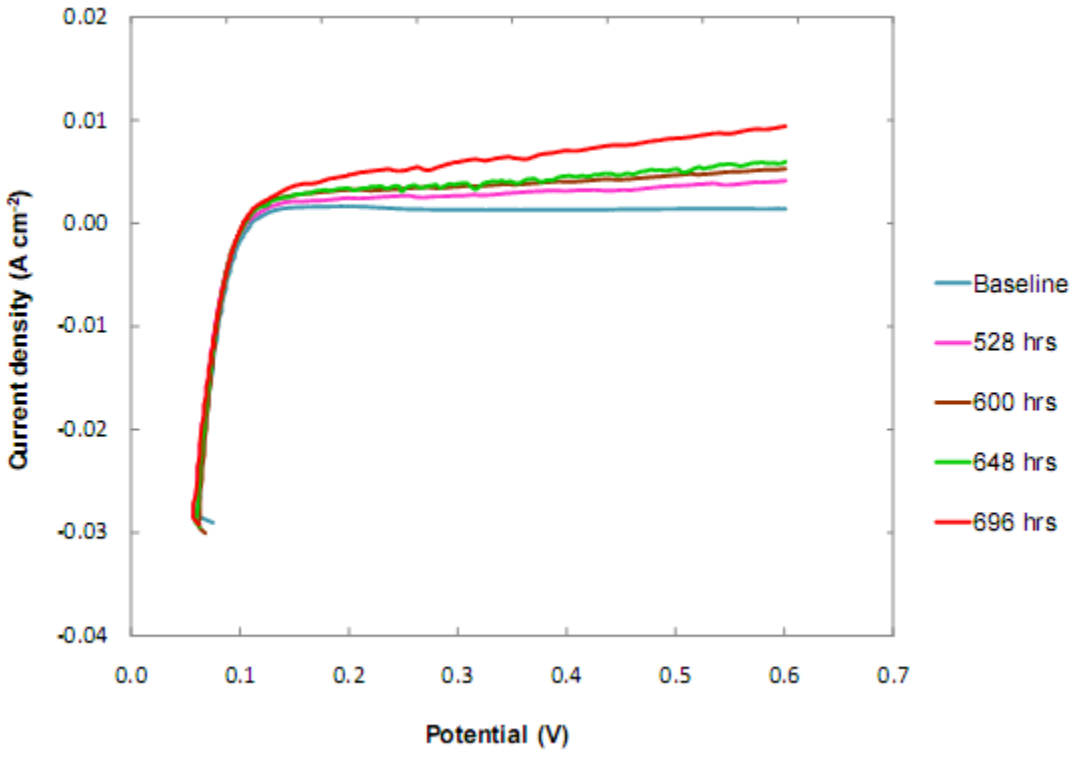

Figure 3-13. Hydrogen crossover measurement of a PEM fuel cell. The cell with an active area of 42.25 cm^2, operated at 70 ºC under humidified conditions. H_2 and N_2 flow rates are 0.3 slpm.

3.8 Ion chromatography

Fluoride ion analysis was carried out with a Dionex ED40 electrochemical detector working with a Dionex GP40 gradient pump (Figure 3-14). A minimum detectable fluoride ion concentration of the instruments is 0.011 ppm. During the fuel cell operation, water vapor that flows out from the fuel cell will condense and it was collected in anode and cathode knockout drums. The water was daily collected and measured its volume during a collection period. By using the technique of ion chromatography, an analysis of the effluent water for the fluoride ions was then conducted. Fluoride release rates and cumulative fluoride release from the anode and cathode sides could be determined. The sample data and calculations for cumulative fluoride release are shown in Appendix D3.

Figure 3-14. Dionex ED40 electrochemical detector and Dionex GP40 gradient pump for fluoride ion analysis.

3.9 Infrared (IR) Imaging

Infrared imaging was performed to measure the heat radiated by the MEA. The molecule movement in the MEA generates the heat. This is based on the heat output from the chemical reaction between anode and cathode inside the fuel cell. The higher the temperature is, the more the molecules move and the more infrared produces. Heat sensed by the IR camera can be measured and evaluated the relative severity of heat-related problems [71].

In this experiment, the IR camera was used to observe the thermal profile of the MEA including fresh and degraded MEAs. Basically, at the location that has higher reactant crossover where hot spot or pinhole was generated, the IR images displayed higher temperature distribution. Figure 3-15 and Figure 3-16 show the pictures of the IR camera (InfraTech GmbH) and a specially designed cell (50 cm^2 active area) with an open cathode, respectively. The designed cell was opened at the cathode to allow a sufficient air for the reaction. For the anode, hydrogen supply was provided. In the experiments, two levels of hydrogen concentration were used: 100% pure hydrogen and 20% H_2 in N_2.

To observe the temperature distribution of the MEA, the fresh or degraded MEA was assembled in the designed cell. Pure hydrogen or diluted hydrogen was passed at 30 ml min^{-1} through the anode inlet at room temperature with a pressure of 5 psi. Then the IR camera was set towards the open cathode. The IR images were displayed via IRbis online 2.4. To view the saved image or adjust parameters of the image, VarioAnalyze was used.

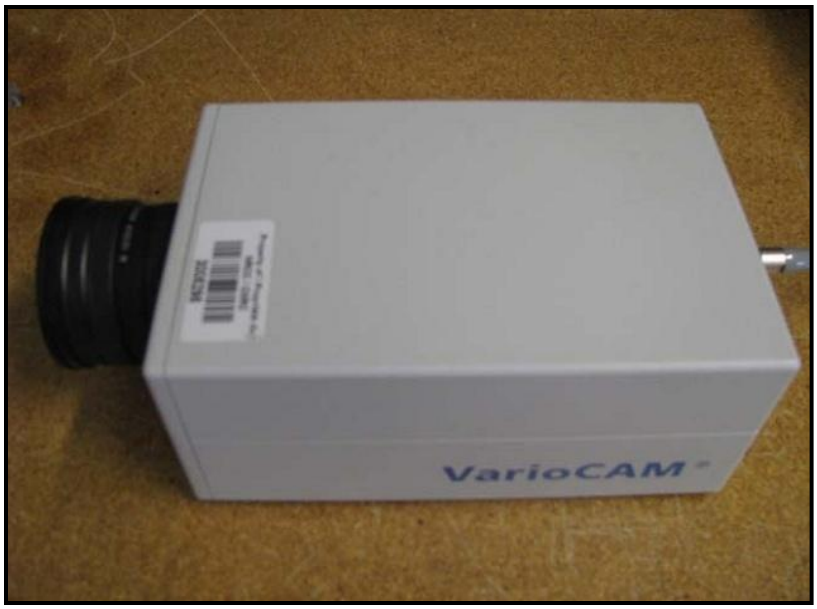

Figure 3-15 IR camera (InfraTech GmbH) [71].

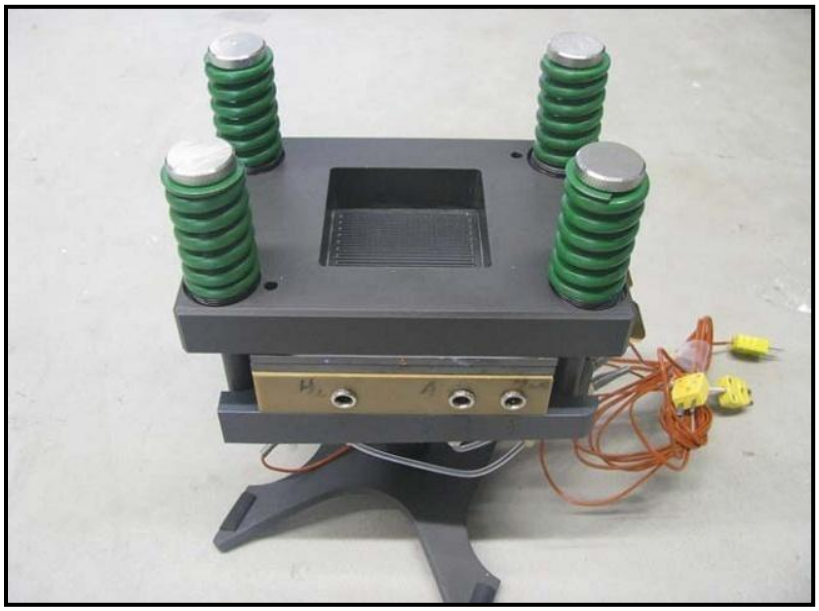

Figure 3-16. Specially designed fuel cell with an open cathode and active area of 50 cm^2 [71].

3.10 Scanning Electron Microscopy (SEM)

Scanning electron microscopy (SEM) is a powerful tool to characterize the morphology of the MEA sample. The sample's surface is investigated by scanning it with a high-energy beam of electrons. The electrons emitted from an electron gun in the microscope hit the sample under investigation and produce signals that contain information about the object's surface topography and composition. The SEM is able to produce very high-resolution images of the sample's surface. The high-resolution achievable with the SEM and a large depth of field provided make the instrument become useful to examine the effect of different processing techniques on material morphology; MEA layers in particular [4].

In this work, the SEM was used to compare and investigate the microstructure of fresh and degraded MEAs under two different conditions, i.e., changing RH by using 100% RH and RH cycling conditions. Three types of signals were generated by the SEM, including secondary electron emissions (SE2), backscattering (BSE), and x-ray emissions. SEM imaging allows observation of general surface defects, thickness of each layer, desperation between the MEA layers, and presence of metal contaminants and relative concentration of elements [4].

The SEM analysis was carried out using LEO 1530 SEM with field emission Gemini Column as shown in Figure 3-17.

Figure 3-17. LEO 1530 SEM with field emission Gemini Column for SEM analysis

Before fixing the MEA samples to an aluminum stub, the MEAs were first separated from the GDLs. Liquid nitrogen was used to separate the MEAs as well as to freeze the MEA for sample preparation. The samples were prepared and cut approximately into 0.5 x 0.5 centimeters squares and then fixed to the stub with a double sided tape for the surface analysis as shown in Figure 3-18.

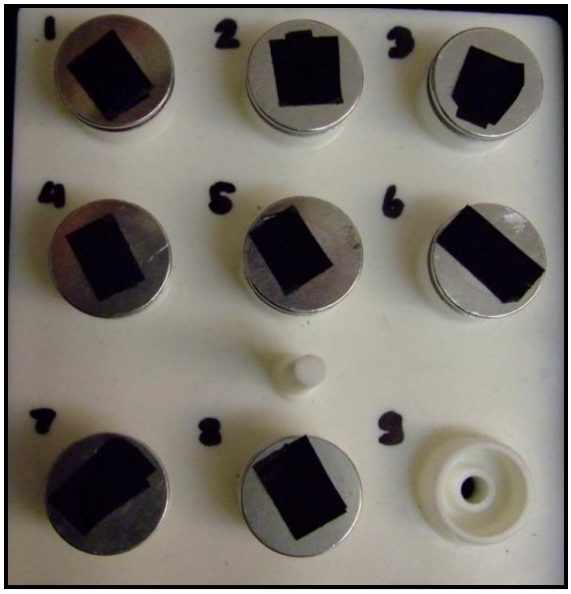

Figure 3-18. MEA samples mounted on aluminum stubs for SEM surface analysis.

For the MEA cross-sectional analysis, the sample was sunk into the liquid nitrogen for a period of time. Once frozen, the sample was fractured in half while still submerged under the liquid nitrogen. Then, one of the halves was mounted upright on the sides of a nut and the nut was tapped on the stub for SEM analysis as displayed in Figure 3-19.

Figure 3-19. MEA samples mounted upright for SEM cross-sectional analysis.

For each run, the SEM images were observed eight evenly distributed locations over the membrane samples. To get a better SEM imaging, all the sample's surfaces were coated by gold using The Desk II Denton Vacuum Gold coating (Figure 3-20). The dispersion with 10 mm in thickness of the gold will enhance the sample conductivity for a clear SEM imaging.

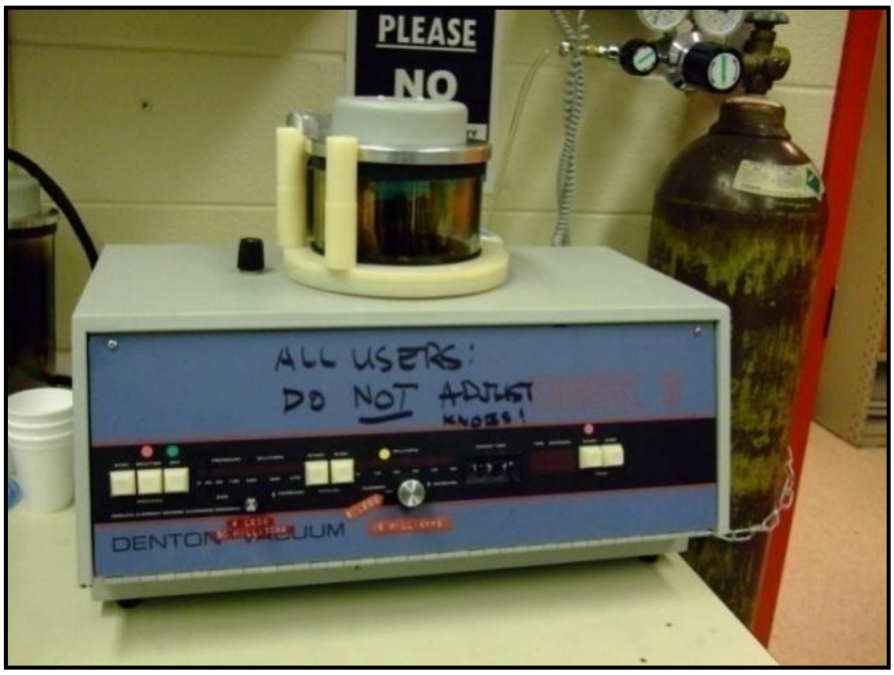

Figure 3-20. The Desk II Denton Vacuum Gold Coating.

The SEM imaging was analyzed at standard magnifications, adjusted by the user. The magnifications used were 100, 500, 1000, 3000, 5000, 8000, and 10000X magnification. Both surface and cross-sectional analysis typically did not adjust beyond 10000X magnification. The electron gun voltage was set between 5 - 10 keV to prevent charging in the materials and damaging the samples. The use of 10 keV was generally high enough for x-ray microanalysis to detect all the elements of interest.

In addition, x-ray compositional analysis was also performed using an electron dispersive (EDS) collector manufactured by EDAX. The EDS collector was conducted to observe the

element compositions on the degraded MEA and also used to confirm an agglomeration of Pt particles that lead to the Pt band formation. The detection limit of the EDAX system is equal to an atomic weight or larger than carbon.

CHAPTER 4: EXPERIMENTAL RESULTS

RELATIVE HUMIDITY (RH) CYCLING EFFECTS

In this study, three fuel cells were operated under idle conditions. The first cell received fully humidified reactant gases, the second cell received H_2-air relative humidity (RH) cycling, and the third cell received H_2 RH cycling while fully humidified air is provided. The experiments are operated at a constant current density of 10 mA cm^{-2}. During the experiments, the second and third cells were conducted via the RH cycling, cycled alternately between dry and humidified conditions. Thus, these latter two cells were tested under the accelerated operating condition of RH cycling. The chemical degradation of both runs was minimized with the use of idle conditions (i.e. low current stress).

The degraded membrane electrode assemblies (MEAs) and gas diffusion layers (GDLs) of (a) Run 1: 100% RH cell with 840 hours, (b) Run 2: H_2- air RH cycling cell with 622 hours, and (c) Run 3: H_2 RH cycling cell with 440 hours are compared in Figure 4-1. Overall, there is no visible burns, rips or tears on the membranes for all the three runs as observed during the cell disassembly as shown in Figure 4-1.

(a) (b)

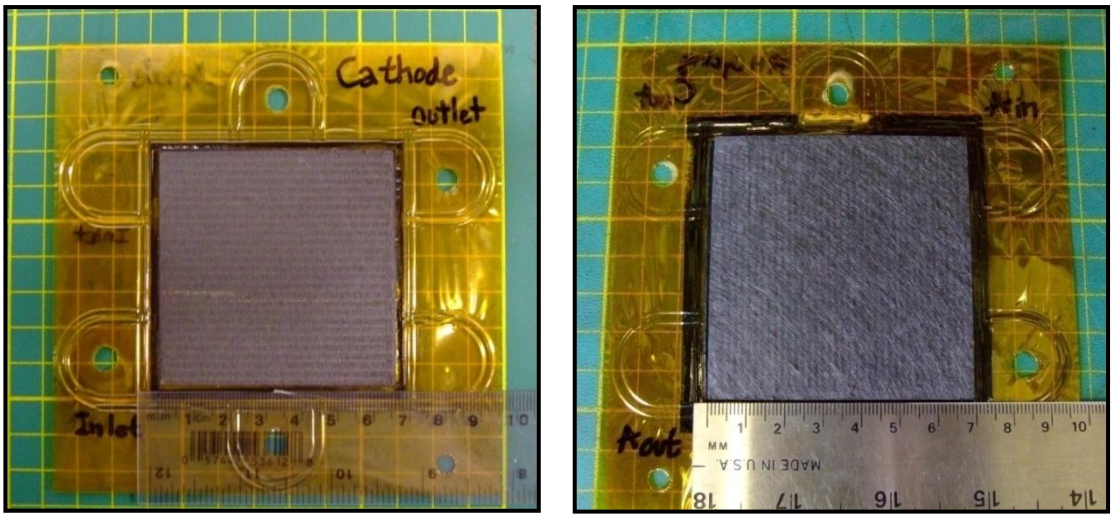

(c)

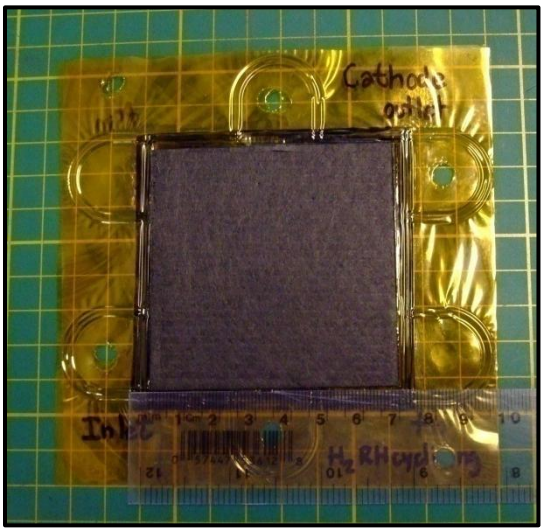

Figure 4-1. The degraded membrane electrode assemblies (MEAs) and gas diffusion layers (GDLs) with 42.25 cm^2 active area of (a) Run 1: 100% RH cell, (b) Run 2: H_2-air RH cycling cell, and (c) Run 3: H_2 RH cycling cell.

From the experimental results, change in relative humidity (RH) has been found to decay PEM fuel cell performance due to an increase in membrane resistance, hydrogen crossover current, hot-spot/pin-hole formation, and fluoride ion release concentration. The RH cycling effects on PEM fuel cell performance can be summarized as follows:

4.1 RH Effect on PEM Fuel Cell Performance

Polarization curves of the three fuel cells' performance at 70 ºC without backpressure are shown in Figure 4-2a (Run 1: 100% RH cell), 4-2b (Run 2: H_2-air RH cycling cell), and 4-2c (Run 3: H_2 RH cycling cell). Changes in polarization curves can indicate what material characteristics have been degraded [72]. A curve can be segmented into four regions – open circuit voltage (OCV), activation loss, linear ohmic loss, and mass transfer limitation – each characterized by a drop from the ideal Nernst potential. The effects on these different regions indicate a decrease in a fuel cell's voltage output. In Figure 4-2a, the 100% RH cell has a lifetime of 840 hours. In this work, the cell was operated until complete failure, in that the cell was deemed to have failed when it was not possible to draw current from the cell anymore. From the initial stage until at 456 hours of operation, there was some translation down on the polarization curve indicating some loss of catalytic activity, likely due to catalyst aging. There is an obvious change in the slope of the polarization curve at 456 hours, which might have been caused by ionic capacity loss, membrane aging, hydrogen crossover, or early mass transfer limitation.

In the case of the H_2-air RH cycling cell, 130 cycles were completed over a cell lifespan of 622 hours (Figure 4-2b). RH cycling began after 120 hours of commissioning. The curve starts to deviate from the original trend at 312 hours. There is also a voltage dip at the higher current densities, which is thought to be the result of mass transfer limitations inside the cell leading to concentration overpotential.

(a)

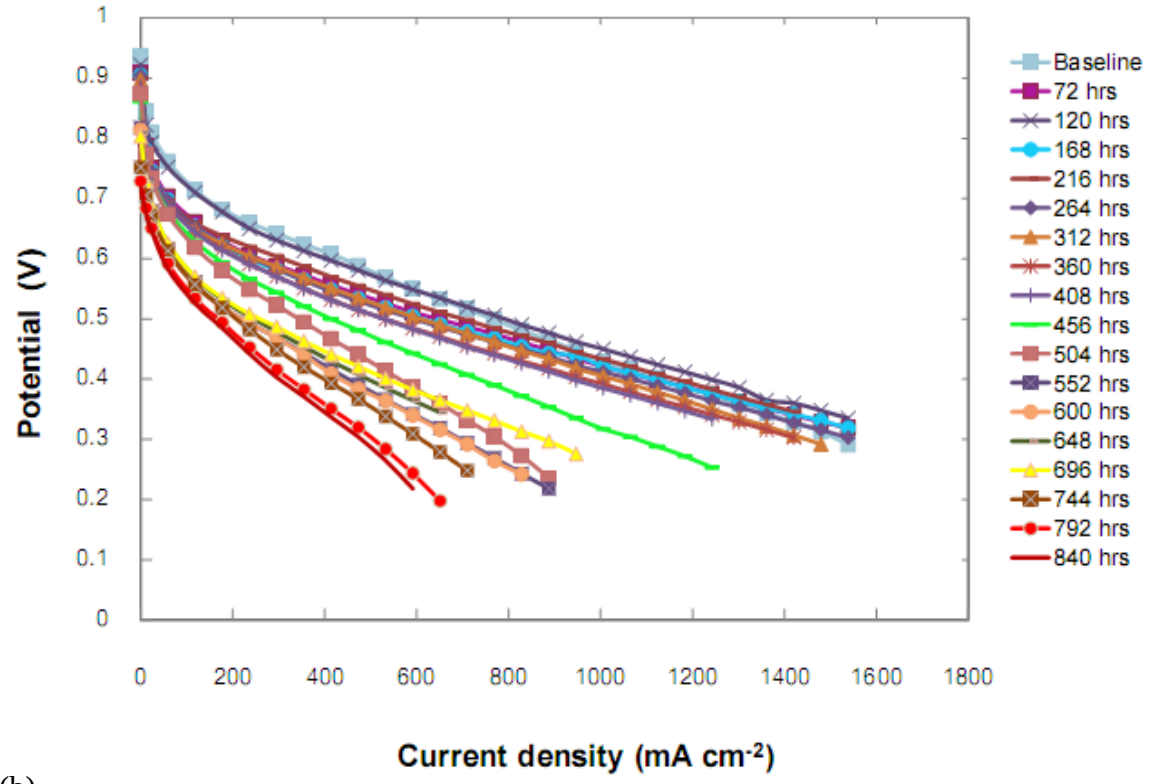
Potential (V)
Current density (mA cm-2)
Baseline
72 hrs
120 hrs
168 hrs
216 hrs
264 hrs
312 hrs
360 hrs
408 hrs
456 hrs
504 hrs
552 hrs
600 hrs
648 hrs
696 hrs
744 hrs
792 hrs
840 hrs

(b)

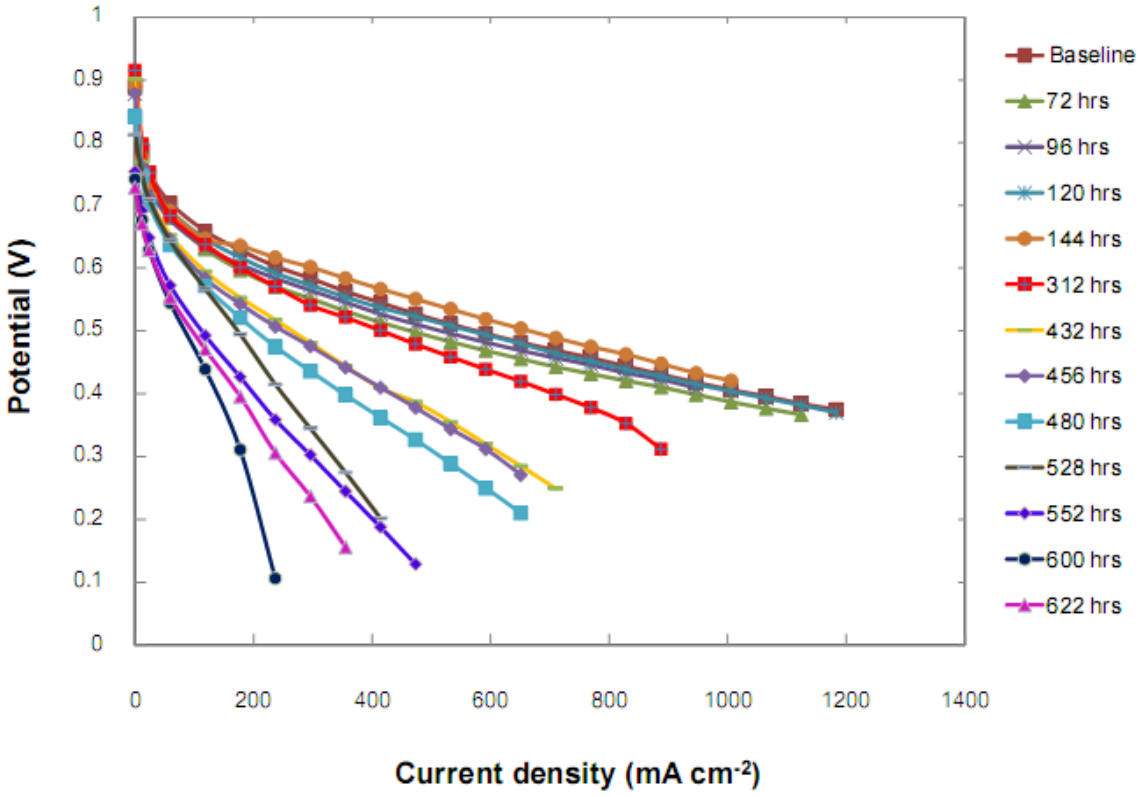
Potential (V)
Current density (mA cm-2)
Baseline
72 hrs
96 hrs
120 hrs
144 hrs
312 hrs
432 hrs
456 hrs
480 hrs
528 hrs
552 hrs
600 hrs
622 hrs

(c)

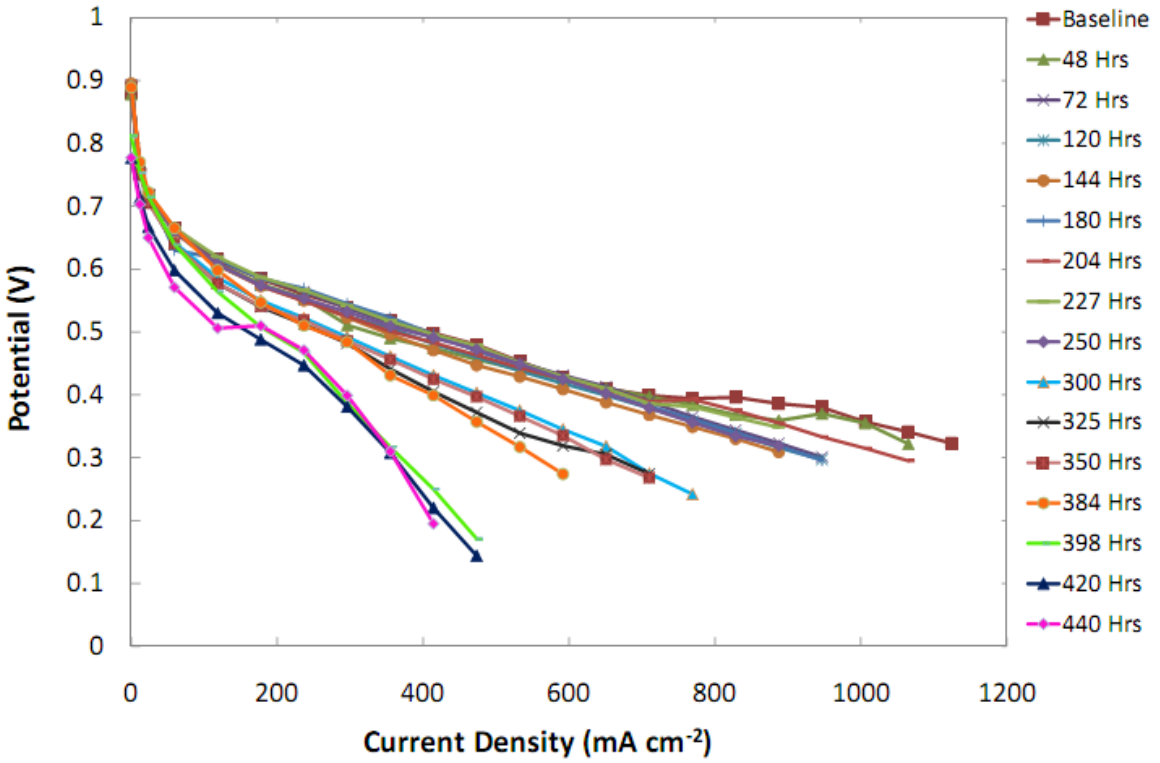

Figure 4-2. PEM fuel cell performances of (a) Run 1: 100% RH cell, (b) Run 2: H_2-air RH cycling cell, and (c) Run 3: H_2 RH cycling cell. The cells are operated at 70 ºC and constant current density of 10 mA cm^{-2} without backpressure. MEAs active areas are 42.25 cm^2; H_2 and air flow rates are set at stoichiometric ratio of 1.5 and 2.5, respectively.

For the H_2 RH cycling cell (Run 3), 100 cycles were completed over a cell lifetime of 440 hours. From the baseline up until at 250 hours, the polarization curves have the same trend. There is a drop of cell voltage along with an increase in current density. At 300 hours, there is a noticeable change in the slope of the curve. The slope starts to deviate from its original trend which might have also been caused by membrane ionic conductivity loss, membrane aging, hydrogen crossover, or mass transfer limitation. A marginal drop of the curve can be observed from 300 to 380 hour of operation. After 380 hours there was a rapid decline in the polarization curve observed. This might have arisen from the irreversible changes in the membrane and catalyst layer at anode side during cycling. In addition, after 400 hours, the cell reaches its final stage mostly probably from membrane failure, likely pinhole formation.

Voltage degradation curves for 100% RH cell (Run 1), H_2-air RH cycling cell (Run 2), and H_2 RH cycling cell (Run 3) are shown in Figure 4-3a, 4-3b, and 4-3c, respectively. Potential is plotted at a constant current density of 10 mA cm^{-2} versus degradation time. As can be seen, each curve is separated into three regions; commissioning region, steady state region, and highly decayed region.

The 100% RH cell (Figure 4-3a) and H_2-air RH cycling cell (Figure 4-3b) show a quite similar change in cell voltage: it increases somewhat after the commissioning procedure (after 120 hours) and then slowly drops along the trend line. Note that the data collected during the commissioning period is not indicative of the trend and is not included in the calculations. At the steady state region, cell voltage degradation rates are 0.13 mV h^{-1} (100% RH) and 0.074 mV h^{-1} (H_2-air RH cycling). The voltage degradation rate of the 100% RH cell is higher than the H_2-air RH cycling cell due to a longer degradation time and a uniformly degraded distribution throughout the MEA. So it is though that there is some slow increase in degradation with time so the rate near the end of this period degradation is at a higher rate because the membrane is thinner. Also, at 100% RH, there is on average more water in the cell than the RH cycled cell. In other works reported earlier this increase in water in the cell led to an increase in catalyst aging and more rapid formation of the Pt band. This can be confirmed via IR images as will be discussed further in Section 4.5, RH Effect as observed by IR Imaging.

At approximately 620 hours for the 100% RH cell and 460 hours for the H_2-air RH cycling cell, a significant drop of the cell voltages is observed. The voltages start to deviate from the trend and enter the highly decayed region. As calculated from Figure 4-3a and 4-3b, the degradation rate of the 100% RH (0.53 mV h^{-1}) is lower than the H_2-air RH cycling (0.70 mV h^{-1}). In addition, the overall cell degradation rates are found to be equal to 0.18 mV h^{-1} (100% RH) and 0.24 mV h^{-1} (H_2-air RH cycling).

(a)

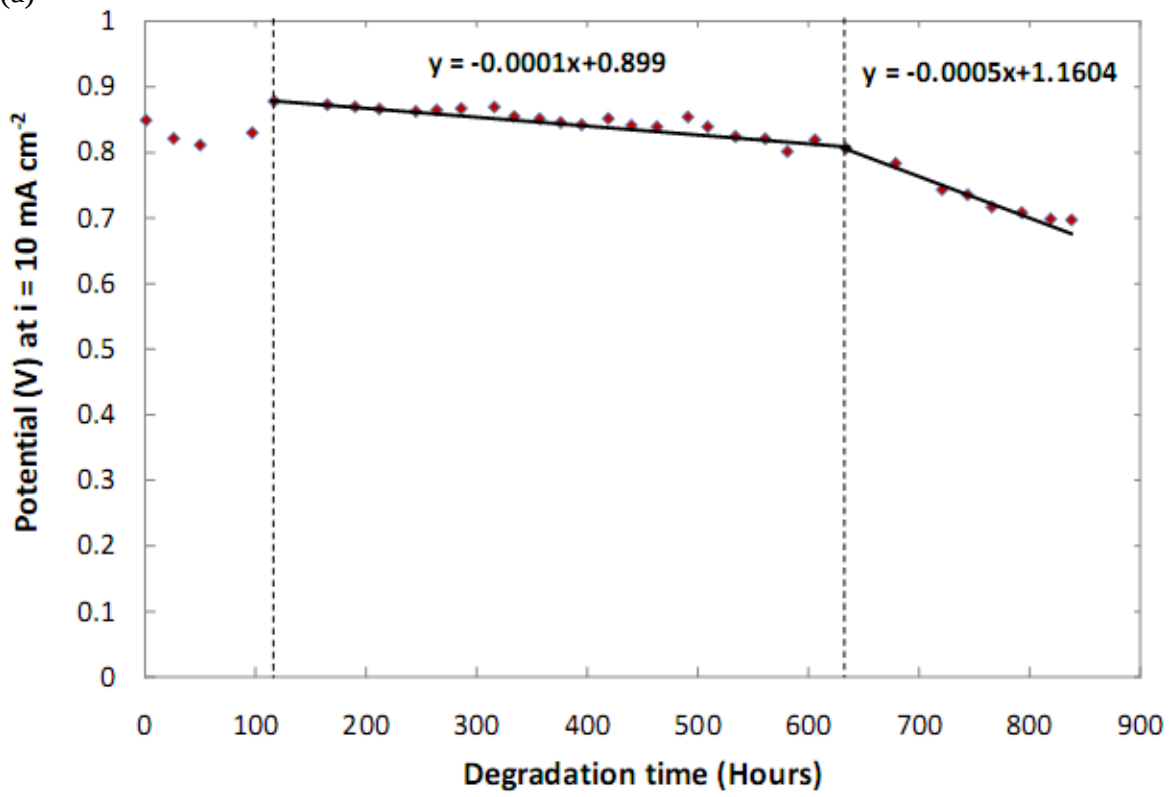
y = -0.0001x+0.899
y = -0.0005x+1.1604
Potential (V) at i = 10 mA cm-2
Degradation time (Hours)
0
0.1
0.2
0.3
0.4
0.5
0.6
0.7
0.8
0.9
1
0
100
200
300
400
500
600
700
800
900

(b)

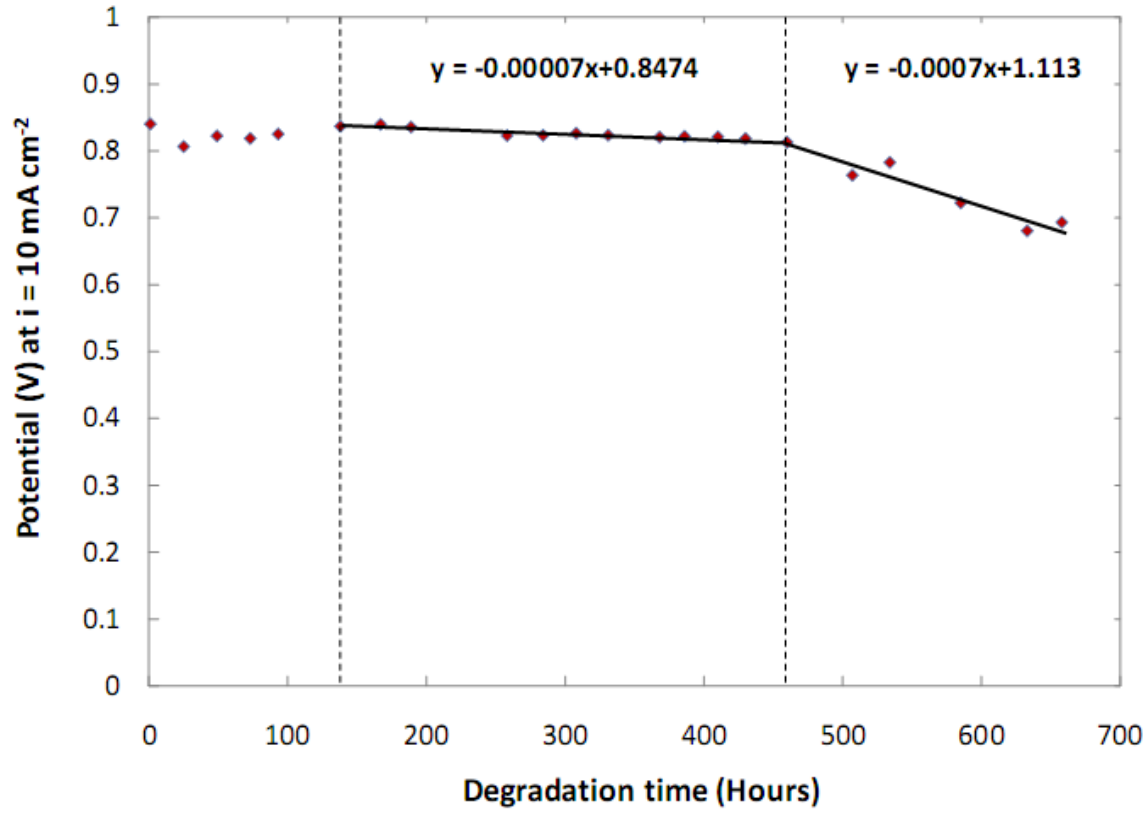
y = -0.00007x+0.8474
y = -0.0007x+1.113
Potential (V) at i = 10 mA cm-2
Degradation time (Hours)
0
0.1
0.2
0.3
0.4
0.5
0.6
0.7
0.8
0.9
1
0
100
200
300
400
500
600
700

(c)

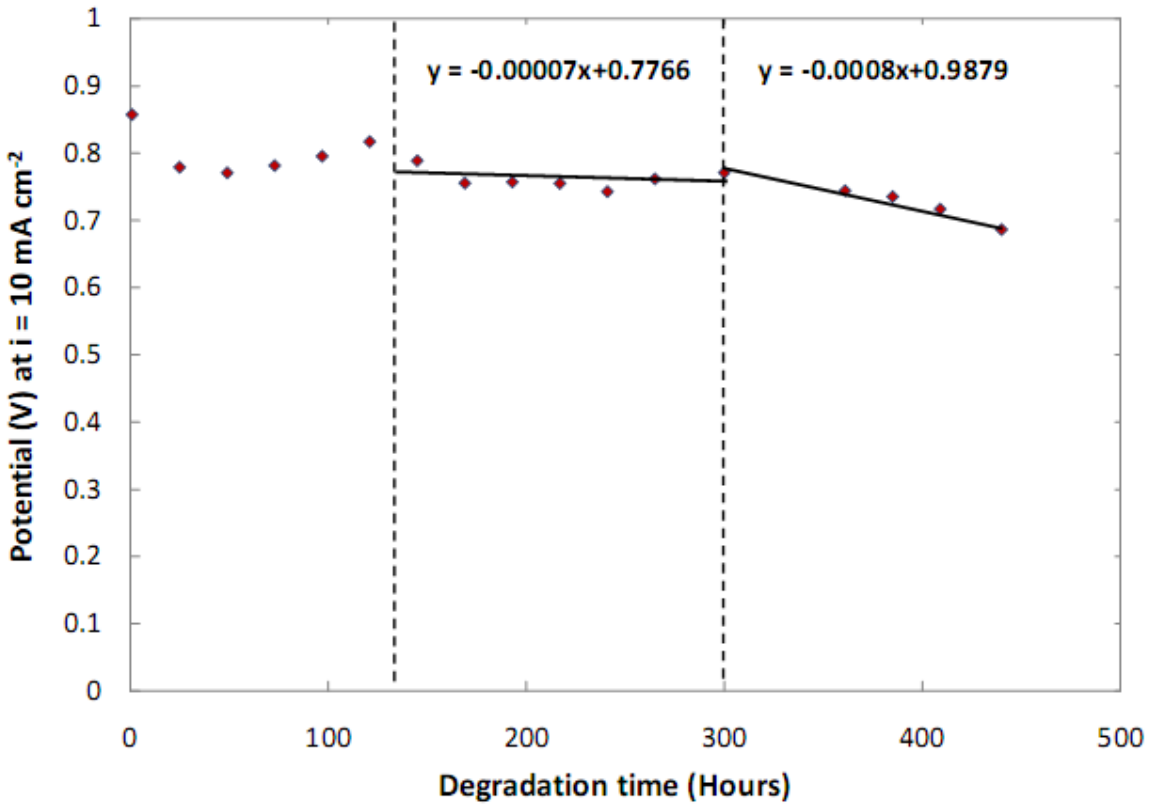

Figure 4-3. Voltage degradation curves of (a) Run 1: 100% RH cell,(b) Run 2: H_2-air RH cycling cell, and (c) Run 3: H_2 RH cycling cell. The cells are operated at 70 ºC and constant current density of 10 mA cm^{-2} without backpressure. MEAs active areas are 42.25 cm^2; hydrogen and air flow rates are 0.113 and 0.358 slpm, respectively.

For H_2 RH cycling cell (Figure 4-3c), a steady state region is considered from 120 hours to approximately 300 hours of the operation. A highly decayed region is after 300 hours until the end of cell's lifetime. At steady state region, cell voltage drops with a rate of 0.07 mV h^{-1} which is lower than the humidified cell (0.13 mV h^{-1}) and H_2-air RH cycling cell (0.074 mV h^{-1}). During the steady state degradation, the RH cycling at anode side might be expected to cause the slow degradation of ionomer in the catalyst layer that can reduce the three phase boundary and a steady decrease in voltage. In contrast, at the highly decayed region, the H_2 RH cycling cell shows a significant drop of the cell voltage with a high rate of 0.80 mV h^{-1} while the humidified and H_2-air RH cycling cells have a cell degradation rates of 0.53 mV h^{-1} and 0.70 mV h^{-1}, respectively. From a calculation of the

slope, the H_2 RH cycling cell has an overall cell degradation rate of 0.3 mV h^{-1}, it is very high when compared with the humidified cell (0.18 mV h^{-1}) and H_2-air RH cycling cell (0.24 mV h^{-1}). Since there is a higher partial pressure of hydrogen (i.e. because there is no water in the stream) during dry condition along-with easy diffusion through catalyst layer may cause a higher cross over of reactant, the overall degradation of the cell run under H_2 RH cycling (Run 3) is higher than the humidified cell (Run 1) and H_2-air RH cycling cell (Run 2).

Based on the results from the polarization curves and overall cell voltage degradation rates, Run 2 clearly showed higher cell voltage degradation rate than Run 1. It is believed that a high failure rate of the H_2-air RH cycling cell and humidified cell take place at approximately 460 hours and 620 hours, respectively. Moreover, the voltage of H_2 RH cycling cell decreased right after the hydrogen cycling is started. The rate of cell degradation is increased and accelerated at the highly decayed region. It is believed that a high failure rate of the H_2 RH cycling cell take place at approximately 300 hours. At 300 hours, the fuel cell failure is noticeable.

Overall, the duration times of the fuel cell degradation for these three runs are consistent with the polarization curve and also other electrochemical diagnostic measurements including an electrochemical impedance spectroscopy and a linear sweep voltammetry that will be further discussed.

4.2 RH Effect as Observed by EIS

The electrochemical impedance spectroscopy (EIS) is a powerful tool used to observe the change in internal resistance of a fuel cell under different operating conditions. In a long term operation of a fuel cell, the resistance changes due to the change in inherent properties of the fuel cell materials. At high frequencies, the imaginary impedance (Z_{im}) is zero and the resistance equals electrolyte resistance. Whereas, at low frequencies, the resistance is the sum of the electrolyte resistance and charge transfer resistance [67].

Figure 4-4 shows Nyquist plot of (a) Run 1: 100% RH cell, (b) Run 2: H_2-air RH cycling cell, and (c) Run 3: H_2 RH cycling cell. The EIS were carried out at 0.85 V for Run 1 and at OCV for Run 2 and Run 3. The humidified cell (Run 1), Figure 4-4a, shows an increasing in diameter of the semi-circle from the baseline until at 400 hours. But there is a small change of the value at the high frequency; in other words, the ohmic resistance which is the real part of the x-axis at the high frequency is quite constant while the charge transfer resistance is increased during the first 400 hours period. The increase in diameter of the semi-circular curve is believed to be caused by a slow of the kinetics of the oxidation reduction reaction (ORR) during a long term operation. After 400 hours, the diameter of the AC impedance tends to reduce. The reduction of the charge transfer resistance is thought to be resulted from the membrane thinning and an increase in hydrogen crossover current. Because of the thinning of the membrane can lead to a better hydration state inside the cell from a water back diffusion of the cathode to anode. The thinning of the membrane will reduce the charge transfer resistance as well as enhance the proton conductivity of the membrane.

(a)

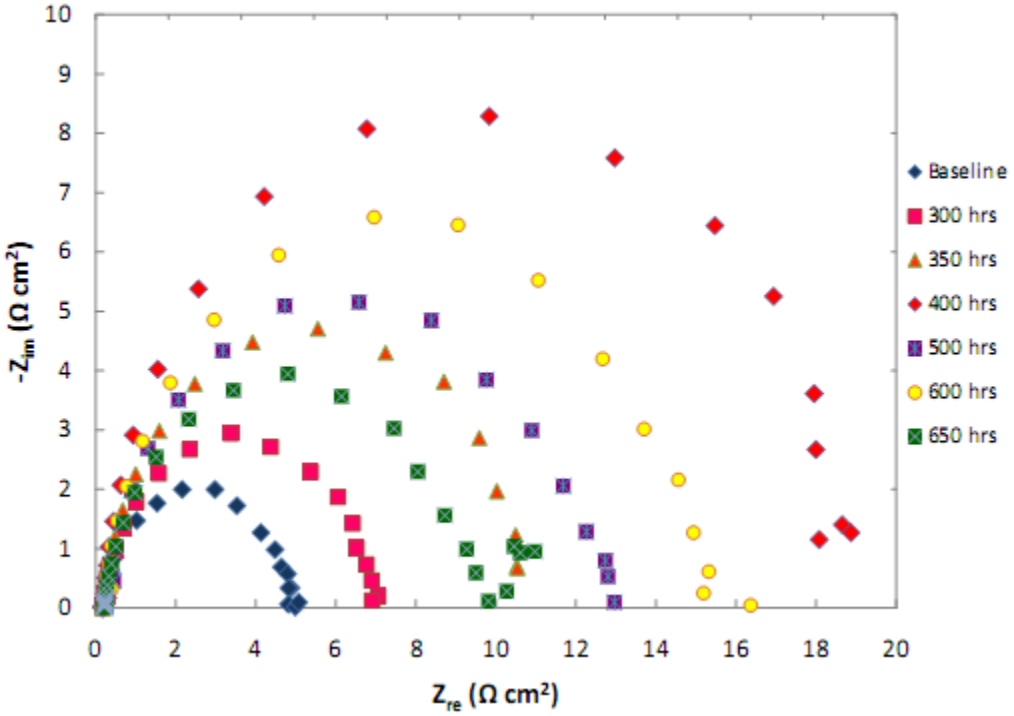

(b)

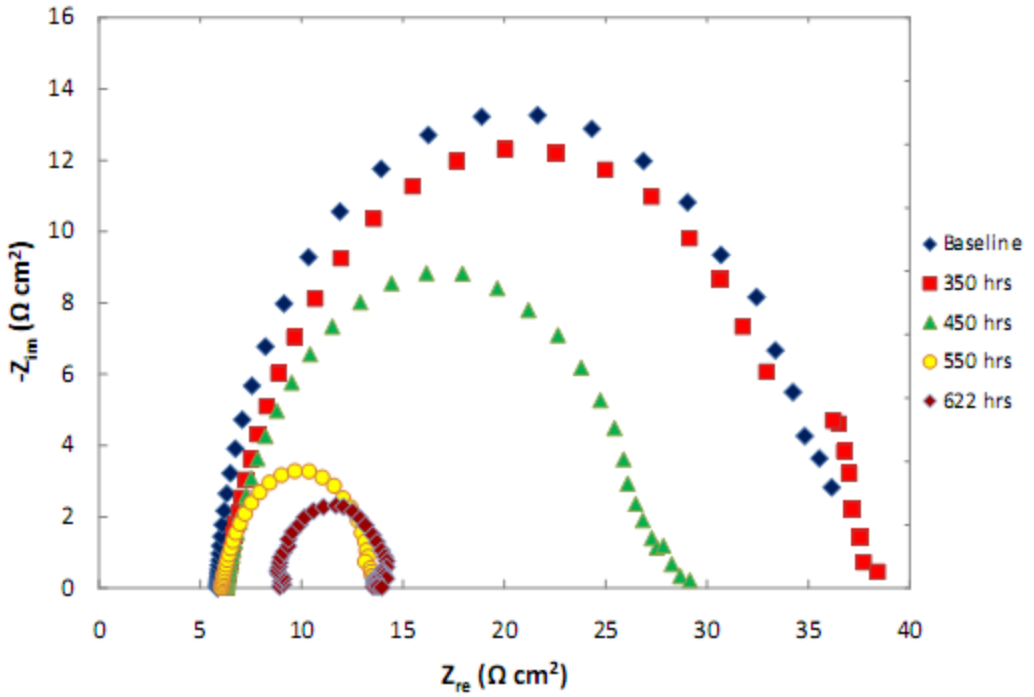

(c)

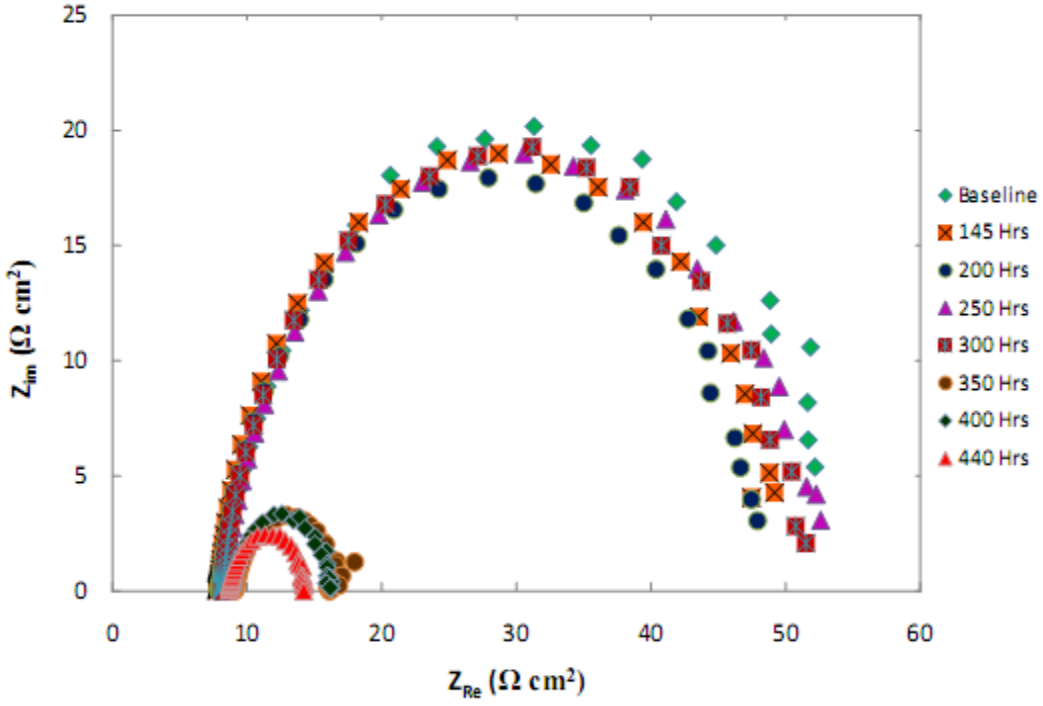

Figure 4-4. Nyquist plot of (a) Run 1: 100% RH cell, (b) Run 2: H_2-air RH cycling cell, and (c) Run 3: H_2 RH cycling cell. The EIS are carried out at 0.85 V for Run 1 and at OCV for Run 2 and Run 3. The cells are operated at 70 ºC and constant current density of 10 mA cm^{-2} without backpressure. MEAs active areas are 42.25 cm^2; hydrogen and air flow rates are 0.113 and 0.358 slpm, respectively.

The results for Run 2 (Figure 4-4b – for H_2-air RH cycling cell) presents in a different manner. The AC impedance shows a decreased semi-circle diameter from the baseline up until the end of cell's life. Again, the decrease in diameter of the semi-circular curves is thought to be due to the increase in membrane thinning and hydrogen crossover current. At 350 hours, there might be an initial state of membrane failure caused by the membrane thinning and crossover current. At 450 hours, membrane delamination might start to generate and lead to a severe degradation of the membrane at the end of cell lifespan. For the ohmic resistance, it is quite constant until at 622 hours, where a rapid increase of the ohmic resistance is observed. A shift of the semi-circular diameter is shown. The movement of the diameter is expected to be caused by a completely degraded membrane structure from the membrane delamination.

Figure 4-4c shows Nyquist plot of the H_2 RH cycling cell (Run 3). From the baseline up until at 300 hours, Nyquist plots present big loops of the semi-circle curves as well as high values of the real impedance (Z_{Re}). The results can be interpreted that at the beginning of cell's life, the H_2 RH cycling cell has a slow rate of the oxidation reduction reaction (ORR) and high in the charge transfer resistance since the impedance analysis was done at OCV condition. However, a huge reduction in the diameter of the impedance can obviously be observed after 300 hours. The decrease of the impedance is believed to be caused by a membrane thinning and an increase in hydrogen crossover current after a long-term operation.

Not only the decrease in the impedance loop is seen, but there is also a shift of the ohmic resistance at 350 hours. The ohmic resistance can be measured at high frequencies where the imaginary impedance (Z_{im}) is zero. The Nyquist plot shows that the ohmic resistance is increased. The increased ohmic resistance is expected to result from a failure of the membrane structure (i.e. membrane delamination) and/or loss in membrane proton conductivity. Finally, the impedance of the cell is exposed with a very small semi-circle when the membrane is completely degraded and becomes very thin or failed with a pinhole. The cycling of the RH on the anode side alone would have caused the anode electrode to swell and contract, while the cathode electrode and the membrane electrolyte

did not. This could have led to a rapid separation of the layers. Also the performance of Run 3 is much less stable than the two earlier runs. This also could be indicative of delamination as a result of the membrane and electrode swelling and contracting. Sometimes the electrode gets good contact with the electrolyte and sometimes not.

From the previous results of the 100% humidified cell (Run 1) and H_2-air RH cycling cell (Run 2), the H_2 RH cycling cell (Run 3) has higher charge transfer resistance with a shorter operating time than those two runs. This might be due to the loss of ionomer in catalyst layer that causes the discontinuity in the proton conduction network. Also, Run 3 shows a slower rate of the ORR kinetics. Moreover, at the final stage of the cell's life, although Run 2 has a huge reduction in the semi-circular circle and a shift in the ohmic resistance similar to Run 3, a highly decayed state of Run 3's membrane failure occurs earlier than Run 2.

One side of the reactants RH cycling or the H_2 RH cycling will generate unsymmetrical pressure distributions across the membrane. This can increase an unbalance force, enhance stresses, and alter a water movement inside the cell. From a mechanical degradation point of view, it is believed that the unsymmetrical pressure distributions across the membrane from the H_2 RH cycling could accelerate the rate of membrane failure more than symmetrical pressure distributions generated from both side of the reactants RH cycling or the H_2-air RH cycling cell.

In conclusion, as expected the conductivity of the electrolyte membrane is related to its water content, thus, an alternation in RH inside the cell directly affects the fuel cell performance. During the RH cycling conditions, water content at the interface of each fuel cell components is varied. A high water level can limit the reactant transport which will reduce the ORR kinetics by altering proton conductivity in the electrode. While a low water level can reduce surface contact of the catalyst with the ionomer and also decrease the proton conductivity of the membrane. An improper humidification will result in a huge increase of ohmic resistance and charge transfer resistance; especially in these particular experiments, the fuel cells were operated at very low current density (i.e. 10 mA cm^{-2})

where there is a very limited amount of water generated from the electrochemical reaction inside the cells. Certainly, RH cycling is an accelerated durability test that leads to rapid membrane failure as result of mechanical failure. As will be confirmed with other examination shown below this mechanical failure is likely due to pinhole formation, although the RH cycling of an anode side only may have led to membrane delamination. The slope of the voltage degradation curve with time certainly is indicative of a pinhole formation and this cell performance testing is easy to operate, requires no additional sensors or hardware, and thus makes it for a useful cell diagnostic in operating stacks.

4.3 RH Effect as Observed by Hydrogen Crossover Current

Using linear sweep voltammetry measurements, the hydrogen crossover currents of (a) Run 1: 100% RH cell, (b) Run 2: H_2-air RH cycling cell, and (c) Run 3: H_2 RH cycling cell are shown in Figure 4-5 where potential is plotted against current density. Figure 4-5a shows a slight increase in hydrogen crossover current of Run 1 as the operation time passes. It can be seen that there is no significant change of slope for this humidified cell. On the other hand, the H_2-air RH cycling cell (Run 2) shows a rapid change in the slope after approximately 460 hours (Figure 4-5b).

Hydrogen crossover current of the H_2 RH cycling cell (Run 3) is shown in Figure 4-5c. It can be seen, there is no change of slope from the baseline up until at 300 hours. After 300 hours, the hydrogen crossover current significantly increases and exceeds 10 mA cm^{-2} where is the value indicates membrane failure. The crossover current increase accelerates to 40 mA cm^{-2} at the end of cell's lifespan. This is mainly due to the membrane failure that might have caused by thinning of catalyst layer or pinhole formation which would accelerate the hydrogen crossover and subsequent degradation of the membrane. As the potential is increased, the linearly increasing current expresses that the cell has loss its durability.

(a)

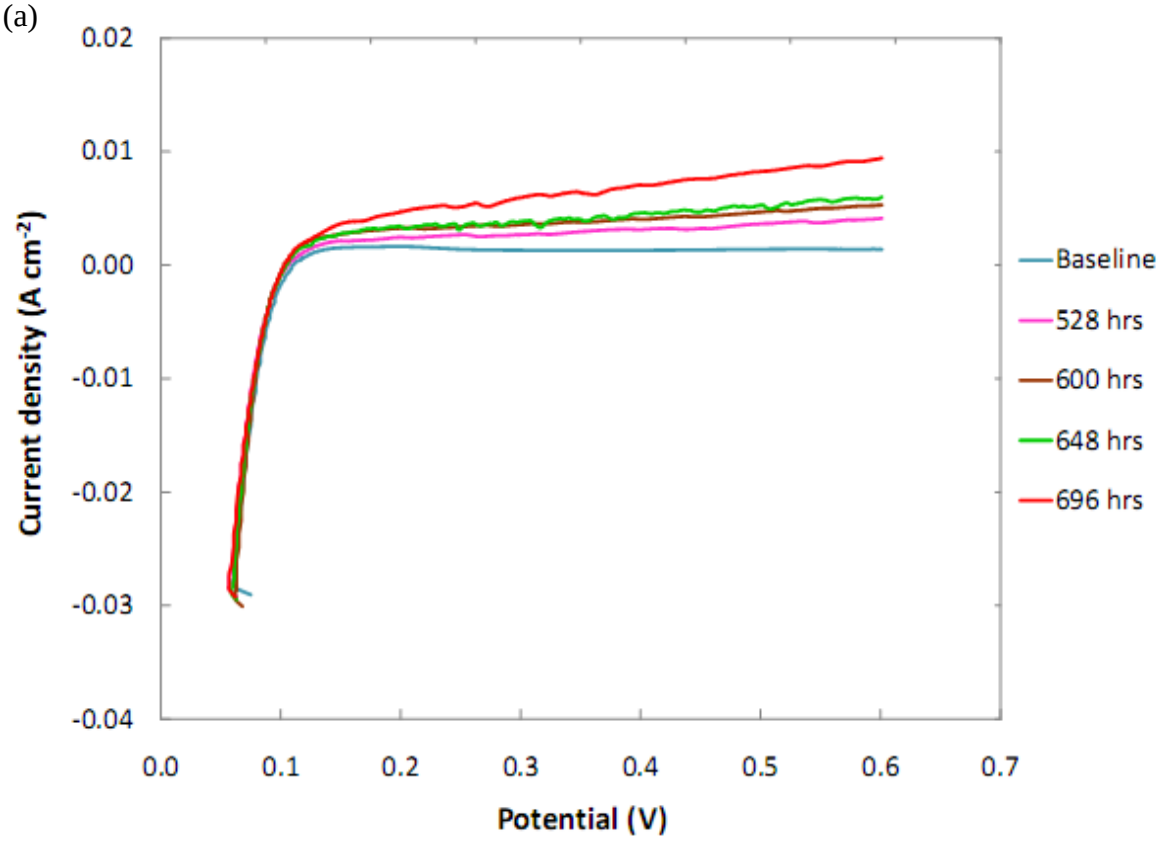
0.02
0.01
0.00
-0.01
-0.02
-0.03
-0.04
Current density (A cm-2)
0.0
0.1
0.2
0.3
0.4
0.5
0.6
0.7
Potential (V)
Baseline
528 hrs
600 hrs
648 hrs
696 hrs

(b)

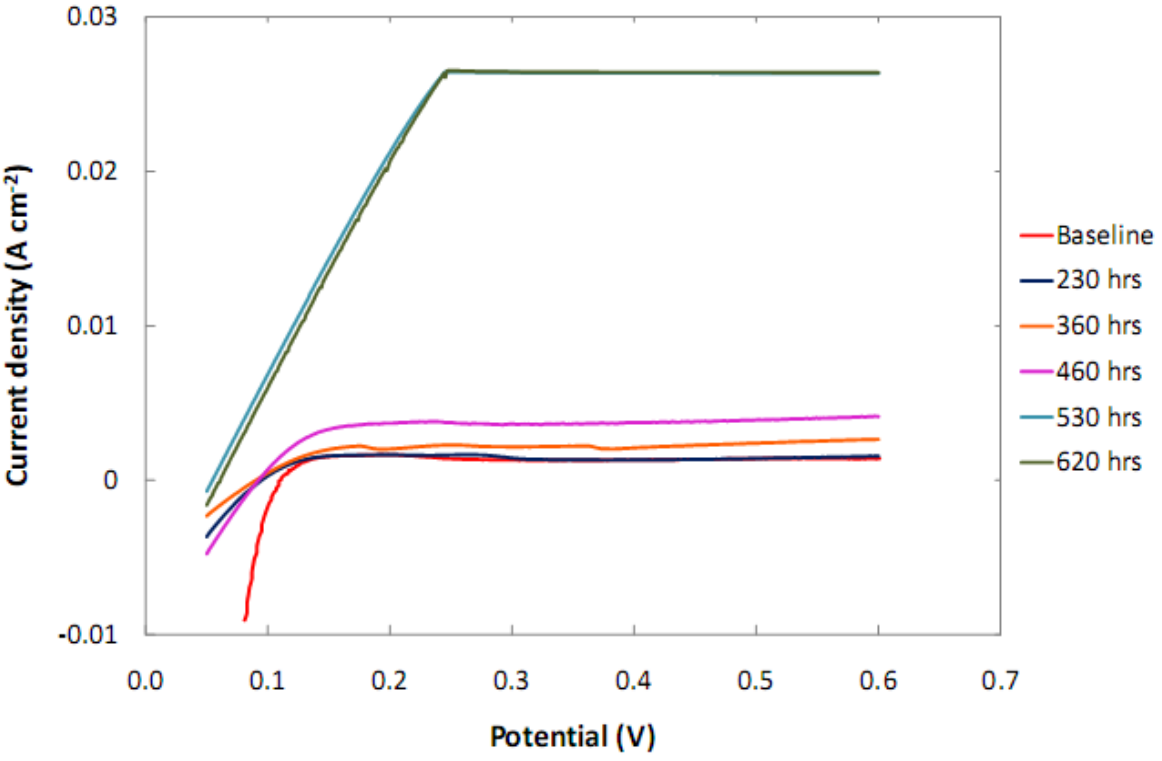
0.03
0.02
0.01
0
-0.01
Current density (A cm-2)
0.0
0.1
0.2
0.3
0.4
0.5
0.6
0.7
Potential (V)
Baseline
230 hrs
360 hrs
460 hrs
530 hrs
620 hrs

(c)

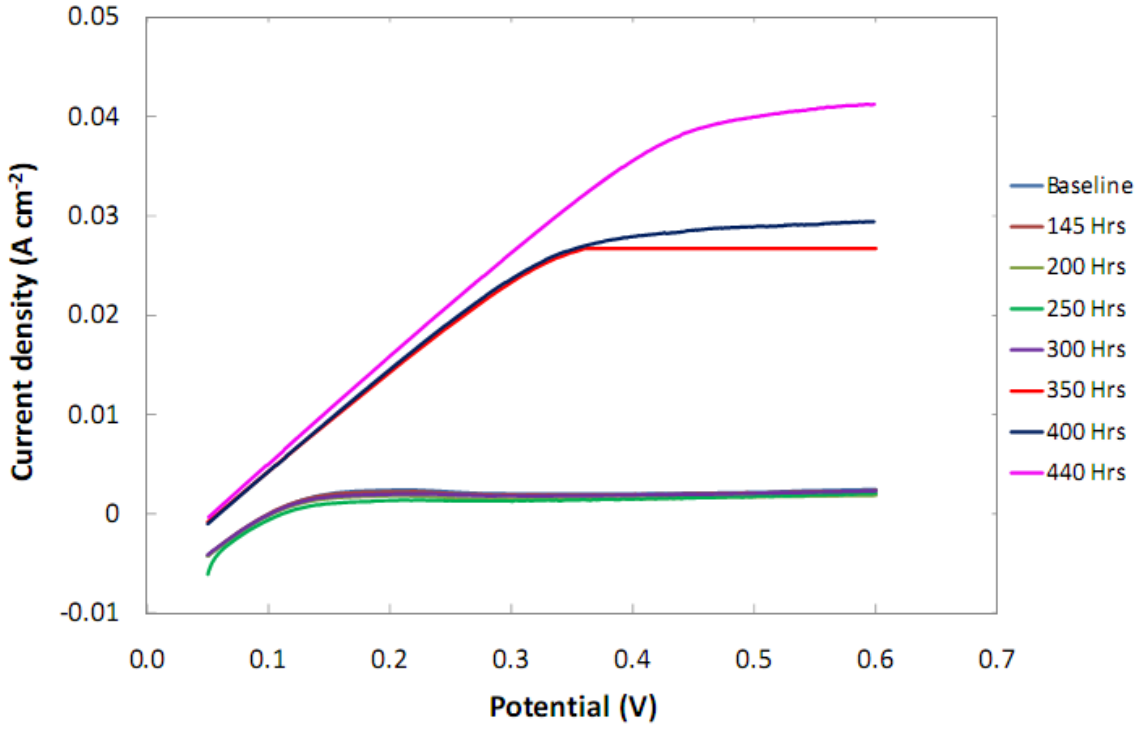

Figure 4-5. Hydrogen crossover measurement of (a) Run 1: 100% RH cell, (b) Run 2: H_2-air RH cycling cell, and (c) Run 3: H_2 RH cycling cell. The cells are operated at 70 ºC and constant current density of 10 mA cm^{-2} without backpressure. MEAs active areas are 42.25 cm^2; H_2 and N_2 flow rates are 0.3 slpm.

In a simple manner, Figure 4-6 compares hydrogen crossover currents of Run 1: 100% RH, Run 2: H_2-air RH cycling, and Run 3: H_2 RH cycling as a function of time. The crossover current of the humidified cell gradually increases until 400 hours when the increase accelerates to reach 10 mA cm^{-2}, which indicates membrane failure [20]. Whereas the H_2-air RH cycling cell's crossover current starts to increase gradually after 200 hours and exceeds 10 mA cm^{-2} at approximately 460 hours and then increase rapidly. Clearly, during Run 2 with the RH cycling at both anode and cathode membrane integrity was compromised at about 460 hours of operation. On the other hand, the hydrogen crossover current of H_2 RH cycling cell rapidly increases after 300 hours. This early stage of membrane failure during Run 3 could be caused by the unsymmetrical stresses that arise from the uneven reactant humidity between anode and cathode compartments in addition to high reactant crossover. Once the anode electrode delaminated in run 3 this

would weaken the overall structure of the MEA and thus a pinhole could more easily form. The crossover current of Run 3 is extremely high compared with Run 1 and Run 2. For instance, at 400 hours, the hydrogen crossover current of Run 3 is 30 mA cm^{-2} whereas Run 1 and Run 2 are 3 mA cm^{-2} and 4 mA cm^{-2}, respectively.

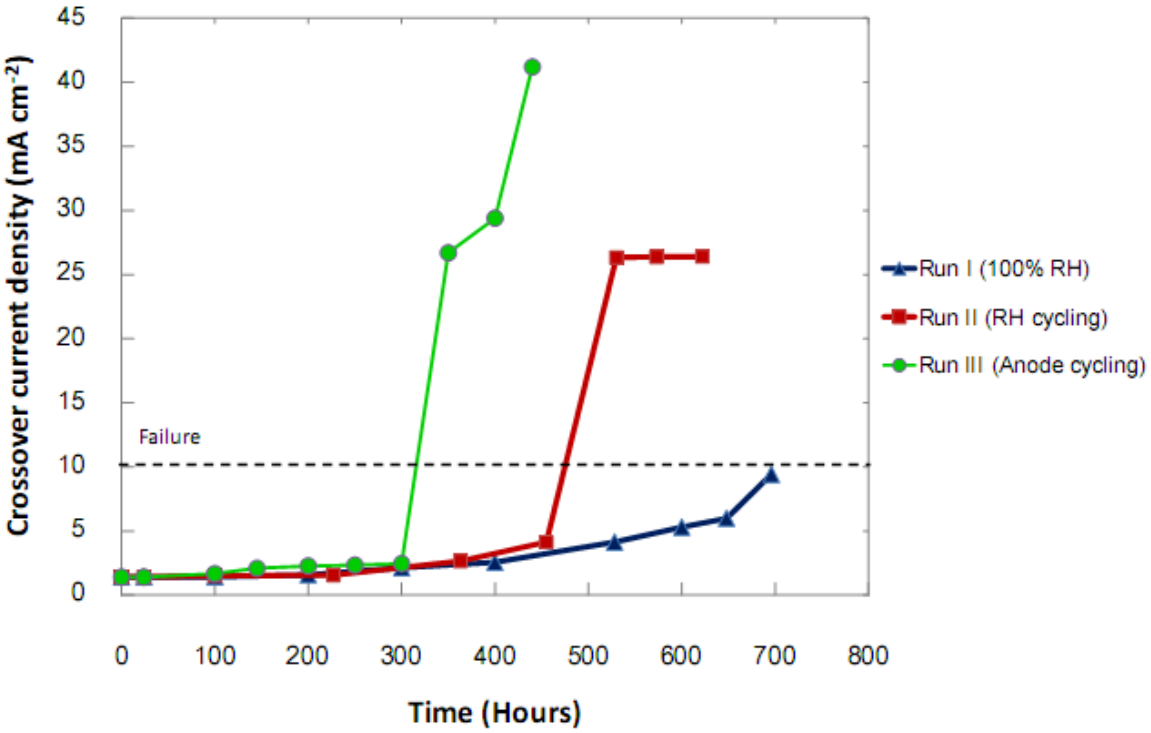

Figure 4-6. Comparison of hydrogen crossover current density of Run 1: 100% RH cell, Run 2: H_2-air RH cycling cell, and Run 3: H_2 RH cycling cell.

The results from the polarization curves, voltage degradation curve, electrochemical impedance spectroscopy, and linear sweep voltammetry are well in agreement and elucidated a severe membrane failure occurs at 620 hours, 460 hours, and 300 hours for the humidified cell (Run 1), H_2-air RH cycling cell (Run 2), and H_2 RH cycling cell (Run 3), respectively. The author believes that membrane failure of Run 1 results primarily from membrane thinning due to the degradation of membrane structure after a long-term operation. While an early membrane failure of Run 2 and Run 3 is mainly caused by variation of reactant partial pressures along with membrane and catalyst layer drying during the RH cycling operation. Changing in RH can alter the reactant partial pressures

which are believed to be a good driving force of the gases to cross over from one side of the fuel cell to the other.

Variation in the RH increases the hydrogen crossover current because crossover is a function of hydration and temperature [20]. The RH also influences reactant partial pressures, membrane permeability, and membrane thickness [42]. During the RH cycling, a change in reactant partial pressures can drive the gases to cross over from one side of the fuel cell to the other. Partial pressure differentials in the reactants can also create localized stress on the membrane, leading to gas crossover. The membrane's permeability to the reactant gases typically increases along with the RH which will increase either hydrogen or oxygen concentration [11, 46, 47]. A higher driving force for hydrogen permeation over oxygen permeation attributes the degradation of membrane [4]. It is believed that the crossover current through the membrane might increase by the effects of reactants changing from dry to fully humidified.

During dry conditions, hydrogen partial pressure changes while air partial pressure is constant. An increase of reactant partial pressure differential will accelerate the crossover current, localized stresses, rips and tears, and hot-spot/pin-hole formation on the membrane. Once pinholes arise, the crossover rate increases rapidly [21, 28, 54, 56]. Also, as time passes, the electrolyte membrane is degraded and consumed; resulting in membrane thinning that allows the gases to easily cross over to either side. In effect, these will generate a harsh mechanical failure of the membrane. In addition, the mechanical failure will lead to chemical degradation inside the membrane. Combining mechanical and chemical effects together, it finally results in a loss of fuel cell performance.

In this work, the RH cycling experiences membrane thinning (slow increase in crossover), and then a pinhole formation at about 460 hours for Run 2 and 300 hours for Run 3. This would indicate that cross over current test in-situ is a suitable 'diagnostic' test (none destructive) for indication of pinhole formation in the cell. Note that it is anticipated that with a stack of many cells the results will be confounded from cell to cell and thus more

difficult to interpret. In the run without RH cycling there is also a rate of membrane thinning (i.e. Run 1).

4.4 RH Effect as Observed by Fluoride Ion Release

Fluoride ion release is a good indicator of overall membrane degradation [25]. The membrane degradation mechanism is believed to be loss of material as the membrane's polymeric structure deteriorates. When a PFSA membrane degrades, it releases peroxides and hydrogen fluoride (HF). Over the cell's operation time, these acidic byproducts can also degrade the cell components and cause failures such as cracks or pinholes. If such failures develop, leakage and crossover may increase, thereby degrading the fuel cell's performance and shortening its lifespan [8, 20, 68]. However, the integrity failure seen in other tests was not indicated in this diagnostic.

In this study, effluent water from anode and cathode sides was collected during fuel cell operation. Ion chromatography was then used to measure the fluoride ion concentration arising from degradation of the membrane structure. By measuring the total amount of water produced, the fluoride ion release rate and the cumulative amount of released fluoride ions could be determined. Fluoride ion release rate of Run 1, Run 2, and Run 3 are plotted as a function of time in Figure 4-7a, 4-7b, and 4-7c, respectively.

Over the time, the fluoride ion release rates are scattered around; however, the rates of anode and cathode peak at approximately 120 hours. It shows that the fluoride release rate increase once the RH cycling is started for both Run 2 and Run 3; mainly due to ionomer leaching. At this stage, the time of peak appearance is close to the results from the previous experiments Run 1 which are occurred at around 150 hours. Also, it is consistent with the result reported by Liu et al. [8] and Kundu et al. [20] using Gore^{TM} membranes. Throughout the three runs, fluoride release rates at the cathode side are higher than the anode side as can be seen from Figure 4-7. This is mainly due to the high amount of water at the cathode side that carries the fluoride ions easily.

(a)

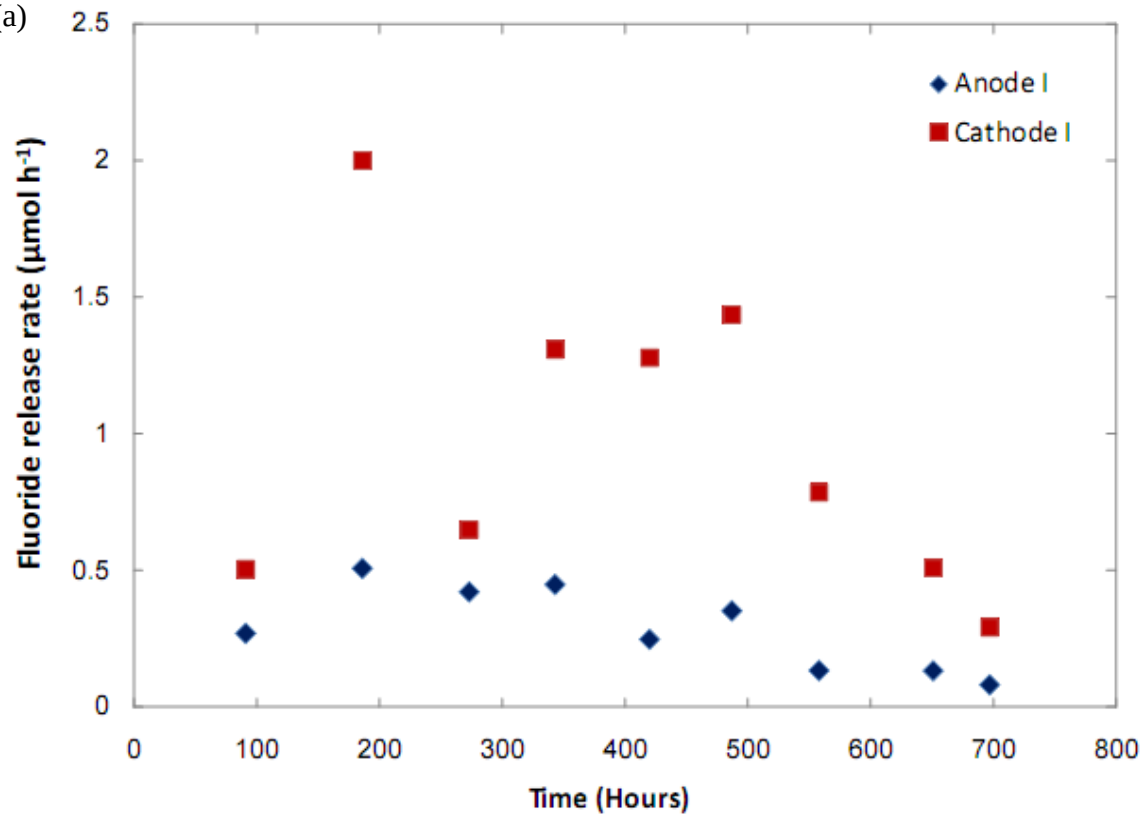
Anode I
Cathode I
Fluoride release rate (µmol h-1)
Time (Hours)
0
0.5
1
1.5
2
2.5
0
100
200
300
400
500
600
700
800

(b)

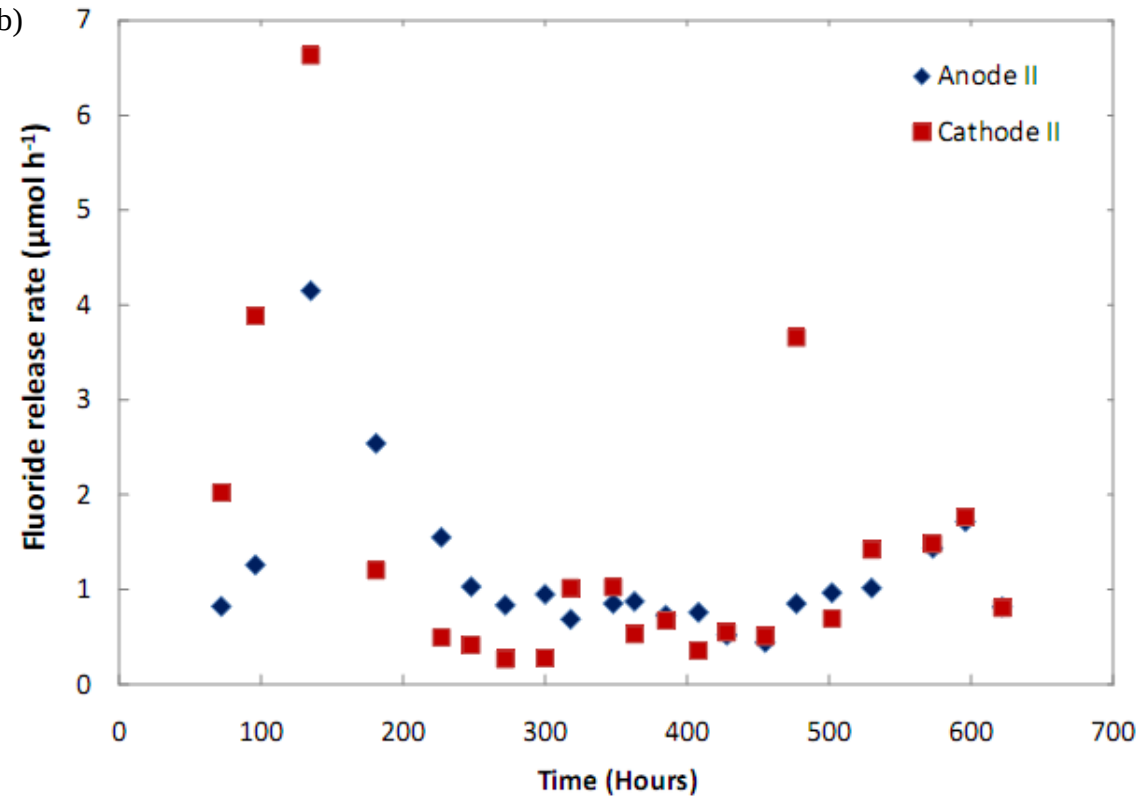
Anode II
Cathode II
Fluoride release rate (µmol h-1)
Time (Hours)
0
1
2
3
4
5
6
7
0
100
200
300
400
500
600
700

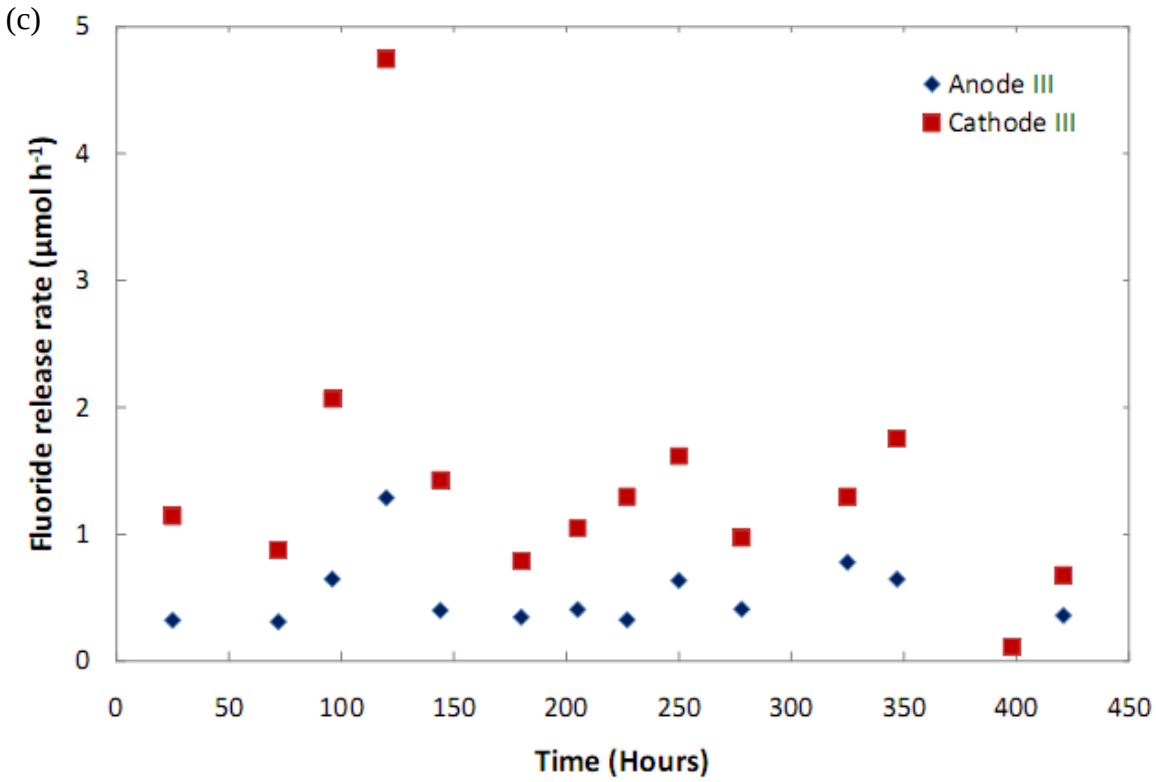

Figure 4-7. Fluoride ion release rate of (a) Run 1: 100% RH cell, (b) Run 2: H_2-air RH cycling cell, and (c) Run 3: H_2 RH cycling cell.

For Run 2 (Figure 4-7b), after RH cycling starts, some points show a higher fluoride release rate at the anode side than at the cathode side. This is thought to be due to the change in RH that occurs when the difference between the reactants' partial pressures increases. The drying of the membrane may allow for some increased crossover and some increase in membrane degradation. Variation in RH will alter the water drag characteristics between the anode/cathode interfaces. Alternating the water drag characteristics increases anodic fluoride release and decreases cathodic release [15, 41, 47, 53]. These results are consistent with this conclusion.

Cumulative fluoride ion releases of Run 1: 100% RH, Run 2: H_2-air RH cycling, and Run 3: H_2 RH cycling are compared in Figure 4-8. All the curves seem to rise exponentially at the beginning between 100 to 150 hours of the operation time. Then the curves change to a

linear increase and reach an upper limit at the end. At the cathode side, the H_2 RH cycling cell (Run 3) has the highest cumulative fluoride ion release than the other two runs. For example, at 200 hours, the cumulative fluoride ion releases of Run 3 is 18 µmol cm^{-2}, while 13 µmol cm^{-2} and 6 µmol cm^{-2} for Run 2 and Run 1, respectively. In contrast, at the anode side, the H_2-air RH cycling cell (Run 2) has the highest cumulative fluoride ion releases which are 9 µmol cm^{-2}, 5 µmol cm^{-2}, and 2 µmol cm^{-2} for Run 2, Run 3, and Run 1, respectively.

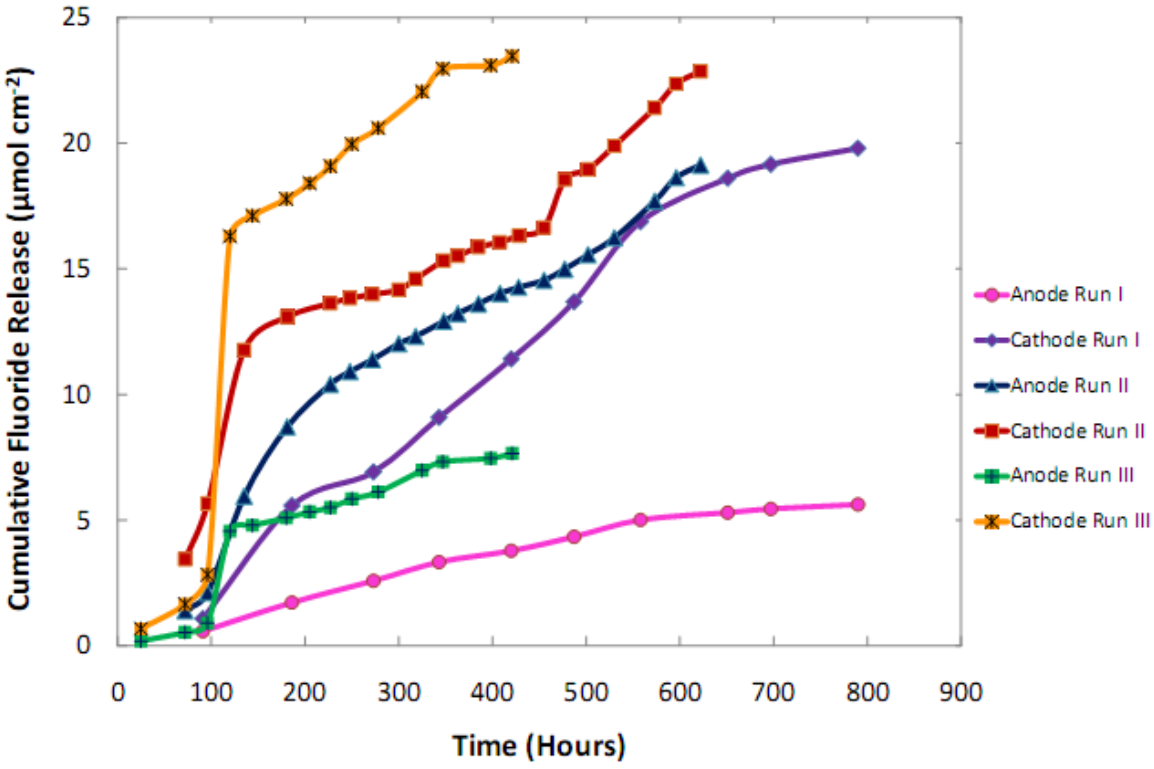

Figure 4-8. Cumulative fluoride ion release of Run 1: 100% RH cell, Run 2: H_2-air RH cycling cell, and Run 3: H_2 RH cycling cell.

From the above fluoride ion release results, the fluoride release changes according to different RH conditions provided to each experiment. Change in RH will lead to an alternation in reactant partial pressures and water balance inside the cell, in particular, Run 2 and Run 3 experiments. From the cumulative fluoride ion releases, Run 3 shows higher fluoride ion releases at the cathode side than Run 2, this is believed to result from a

significantly relative increase in hydrogen partial pressure during H_2 RH cycling conditions, which would lead to greater radical formation and thus more chemical attack on the cathode side. Also note, since the performance of the cell is lower in run 3 because of the delamination, there is less hydrogen dedicated to the electrochemical reaction, so more hydrogen is available to cross over. A difference in partial pressures of the reactants will drag water from anode to cathode. At the cathode, water removed is more than water produced from the cell. This is due to high in hydrogen partial pressure and also less water production since the experiment is operated at low current density. Water balance inside the cell is confirmed by measuring the effluent water of both anode and cathode.

Once at the reaction site, the hydrogen will react with oxygen to form peroxide species which will then form radicals (i.e. OH radicals). As the radicals are created, they will degrade the polymer electrolyte membrane producing fluoride ions as a product. The water movement must be involved in transporting fluoride ions across the membrane. During dry operation of the cell, the water concentration gradient across the membrane will cause the back diffusion of water from cathode to anode. Despite, the net water transport across the membrane will be more towards cathode side due to electro-osmotic drag process. This will make the cathode streams with high fluoride concentration. It is further believed that the membrane degradation moves from the cathode electrolyte slowly through the reinforcement layer, and then begins degrading the anode electrolyte layer [4]. In addition, a high cumulative fluoride ion release at the cathode in all the experiments is thought to be the radical generated close to cathode catalyst/ionomer interface [4, 25, 32]. The failure of membrane is also supported by the SEM observation (Section 4.6) which suggests that the cathode electrolyte has higher rate of membrane degradation than the anode electrolyte.

Although this specific diagnostic was not clearly indicative in this work, and was difficult to co-relate with diagnostic tests, it may be useful for assessment of membrane degradation in general. This is also a more difficult diagnostic to implement on stack in power modules as there is not normally a method to easily collect water discharge from the stack (i.e. most of the water leaves with cathode exhaust as steam), and after collection

the water samples have to be sent to a lab for fluoride ion analysis which would be difficult for an end user.

4.5 RH Effect as Observed by IR Imaging

By using IR camera (InfraTech GmbH), IR imaging was performed. The IR images can distinguish the level of temperature distribution between fresh and degraded MEAs of each run. Variation in temperature distribution is thought to be due to the change in the level of reactant crossover through the MEA. As the reactant crossover increases, more heat is generated resulting in higher temperature distribution on the MEA [65]. To diagnose MEA degradation, the temperature distribution through IR images is used for comparing the RH effect of Run 1, Run 2, and Run 3.

After running approximately at 650 hours, Run 1 was dismantled for IR imaging. Two different hydrogen concentrations were used for this run. Pure hydrogen was first provided by flowing in the top right side of the MEA image at 5 psi and 30 ml min^{-1}. Figure 4-9a and 4-9b show the IR images of fresh and degraded MEAs, respectively. It can be seen that the maximum temperature of the degraded sample is about 2 ºC higher than the fresh sample. The decayed sample shows hot-spots that are generated close to the cathode outlet in the particular area.

At the end of cell's lifetime (840 hours), the temperature distribution on the MEA was observed by using 20% H_2 in N_2 (Figure 4-9c and 4-9d; the IR images of fresh and degraded MEAs, respectively). In this case, diluted hydrogen was used to avoid burning of the degraded sample. The hydrogen was fed at the top right side of the MEA with the same rate and pressure. From Figure 4-9d, the IR image visibly shows a new hot-spot occurring at the bottom right side of the image which is believed to be close to the cathode inlet region. This is the location of a pinhole. Additionally, there is a uniform MEA degradation throughout the sample which is displayed in a yellow color distribution

starting at cathode outlet and at cathode inlet afterward. The uniform degradation is thought to cause by membrane thinning during the idle condition degradation test.

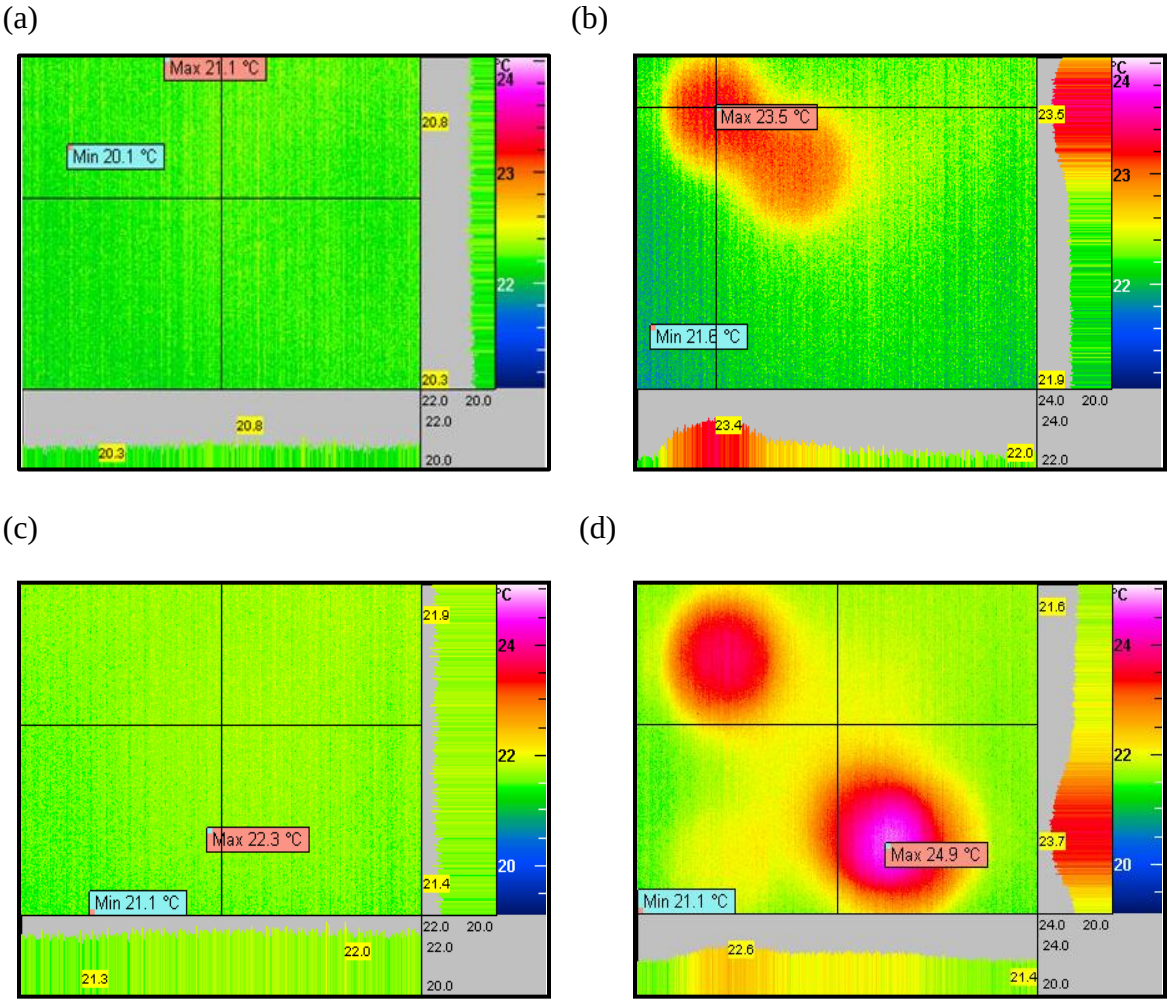

Figure 4-9. IR camera images of Run 1 (100% RH cell): (a) fresh and (b) degraded MEAs at 650 hours and (c) fresh and (d) degraded MEAs at 840 hours. Pure hydrogen and diluted hydrogen (20% H_2 in N_2) are respectively used for the MEAs at 650 hours and at 840 hours. Hydrogen is flowed in the anode inlet of the MEAs at 5 psi and 30 ml min^{-1}.

For the H_2-air RH cycling cell (Run 2), the IR imaging was conducted using 20% diluted H_2 in N_2 with 5 psi and 30 ml min^{-1} under the same conditions as Run 1. After 130 complete cycles, one big hot-spot/pin-hole formation appears close to anode and cathode inlets where dry/humidified reactants alternately enter as shown in Figure 4-10b. Comparing with the fully humidified cell, the H_2-air RH cycling cell differentiates pinhole

formation of the shorter operating time without the uniform MEA degradation throughout the sample. In other words, Run 2 has a smaller rate of membrane thinning than Run 1. This can also be confirmed by the SEM images which will further be mentioned in the next section (Section 4.6).

(a) (b)

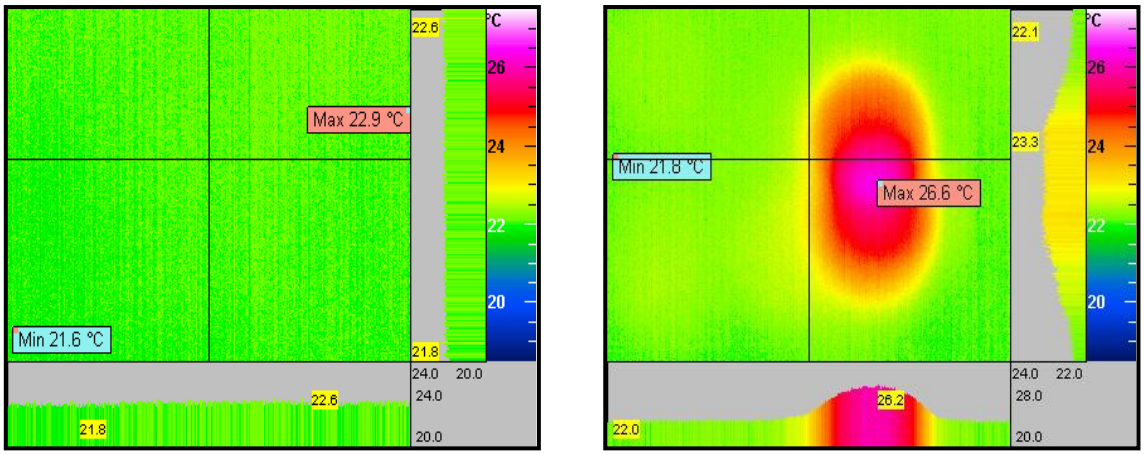

Figure 4-10. IR camera images of Run 2 (H_2-air RH cycling cell): (a) fresh and (b) degraded MEAs at 622 hours. Diluted hydrogen (20% H_2 in N_2) is used by flowing in the anode inlet of the MEAs at 5 psi and 30 ml min^{-1}.

In the case of H_2 RH cycling cell (Run 3), the IR imaging was tested using 20% diluted H_2 in N_2 with 5 psi and 30 ml min^{-1} under the same conditions as the previous runs. Figure 4-11a and Figure 4-11b show fresh and degraded MEAs, respectively. After 100 cycles, two hot-spots generally occur close to the gas outlets as shown in Figure 4-11b. The hot-spots are believed to cause by unsymmetrical pressure distributions and stresses that generated across the membrane during the H_2 RH cycling. In addition, the degraded sample shows a small rate of membrane thinning (observed by a yellow color distribution). Note that the membrane thinning should further be confirmed via the result from the SEM image.

(a) (b)

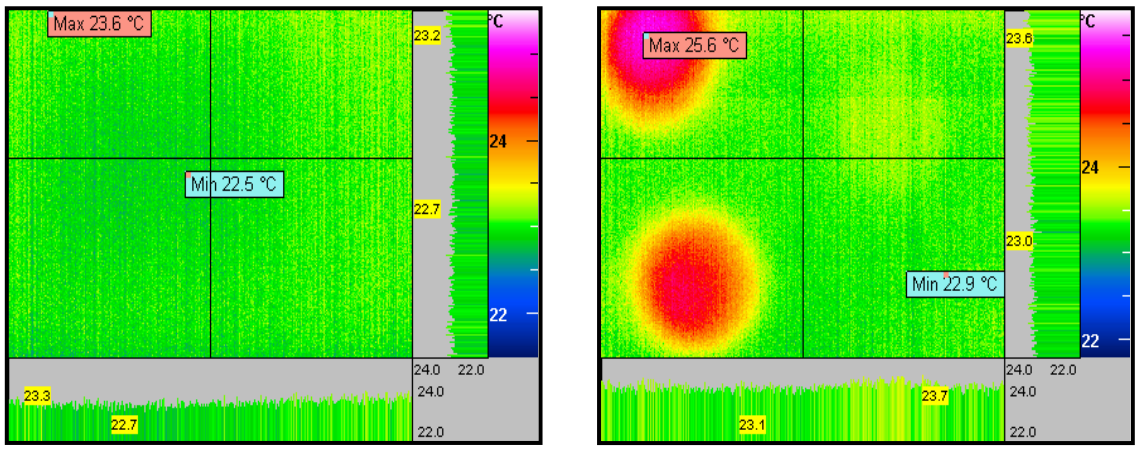

Figure 4-11. IR camera images of Run 3 (H_2 RH cycling cell): (a) fresh and (b) degraded MEAs at 440 hours. Diluted hydrogen (20% H_2 in N_2) is used by flowing in the anode inlet of the MEAs at 5 psi and 30 ml min^{-1}.

Based on the results, the maximum temperatures of the degraded samples are 24.9 ºC for Run 1, 26.6 ºC for Run 2, and 25.6 ºC for Run 3. The RH cycling cells display higher maximum temperature distribution than the fully humidified cell. Change in RH is thus believed to has an effect on the temperature distribution of the MEA due to a highly increase in reactant crossover and hot-spot/pin-hole formation. These results are consistent with the other diagnostics in that membrane thinning was observed in all runs, and the pinhole formation was the cause of cell failure. IR imaging is a useful diagnostic in the lab, however this is an ex-situ destructive test, so has little application on actual stacks.

4.6 RH Effect as Observed by SEM Imaging

After operating for 840 hours (Run 1: 100% RH) and 622 hours (Run 2: H_2-air RH cycling), the MEAs were removed from the fuel cell hardware. The membranes were separated from the GDL using liquid nitrogen. Overall, there is no visible rips or tears on the membranes for both Runs. Note that the results from scanning electron microscopy were completed only for Run 1 and Run 2 within the time allowed.

SEM images were taken from eight different locations over the membrane area for both surface and cross-sections. Samples of surface images of fresh Gore^{TM} 57 membrane, degraded membrane from Run 1, and degraded membrane from Run 2 are shown in Figure 4-12. The surface images of fresh membrane (Figure 4-12a) and Run 1 membrane (Figure 4-12b) are quite similar. A tiny crack all over the membrane surface is observed. The crack is believed to be generated during fabrication, storing, handling, and assembling of the membrane. The small crack over the surface is also noticed from Run 2 membrane (Figure 4-12c); however, there is a huge crack of catalyst layers at its surface. The breakdown of this crack is thought to be caused by mechanical stresses generated during the RH cycling conditions which lead to membrane swelling and contracting.

(a)

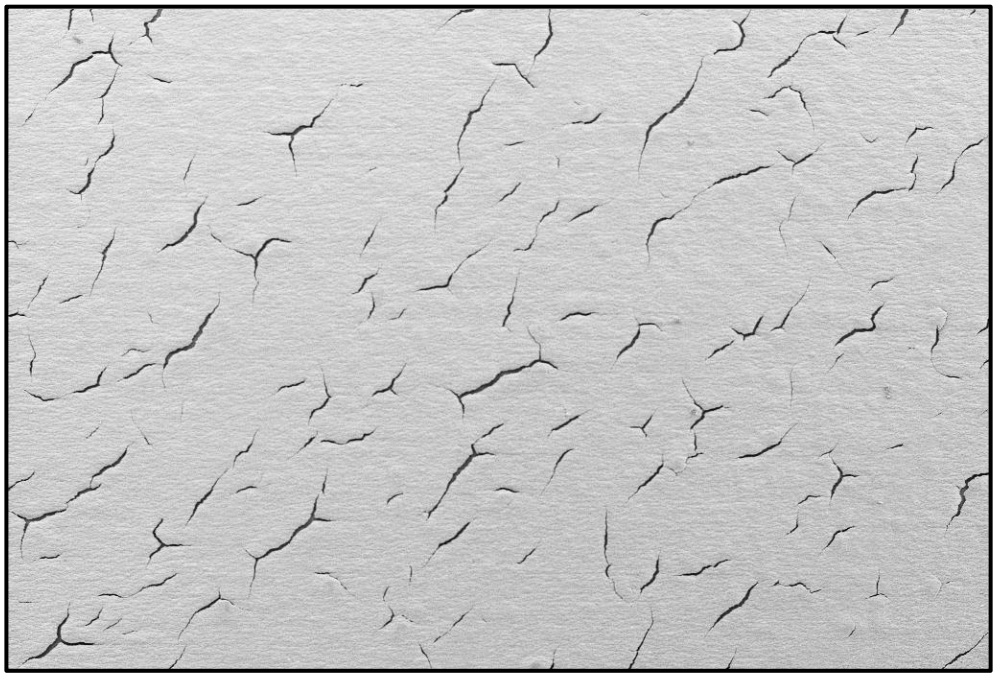

(b)

(c)

Figure 4-12. SEM surface images of (a) fresh Gore^{TM} 57 membrane (100x magnification), (b) 100% RH cell (Run 1) with 840 hours operation (100x magnification), and (c) H_2-air RH cycling cell (Run 2) with 622 hours operation (100x magnification).

To measure the thickness and observe the morphology changes of the membranes, the cross-sectional layers of the membranes from the SEM were also performed. Figure 4-13 shows the cross-sectional layers of fresh Gore^{TM} 57 membrane consisting of cathode and anode catalyst layers, ePTFE reinforcement layer, and cathode and anode electrolyte layers. Initially, cathode and anode catalyst layers have similar thickness measuring between 12 – 14 µm. Cathode and anode electrolyte layers range between 9 – 10 µm. The reinforcement layer thickness is between 6 – 7 µm. The fresh Gore^{TM} 57 membrane thus has an overall thickness of approximately 50 µm.

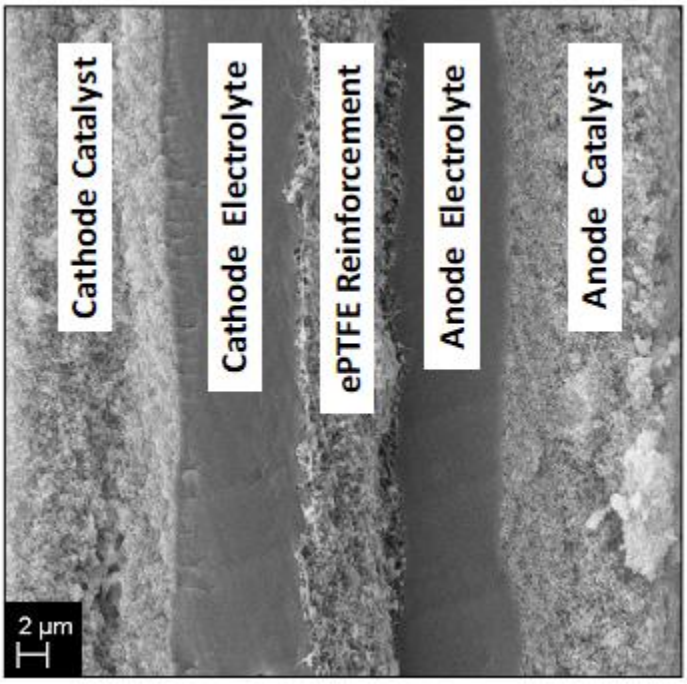

Figure 4-13. SEM cross-sectional layers of a fresh Gore^{TM} 57 membrane with 50 µm thickness (5000x magnification).

Figure 4-14a shows the cross-sectional layers of the membrane from Run 1. In this case, the cathode catalyst layer and cathode electrolyte layer are significantly reduced. From overall, the CCM thickness is reduced to 27.5 µm which is almost half of the original fresh CCM. Membrane thinning at the cathode side is visibly observed for the humidified cell. The membrane thinning is a good method for observing membrane degradation since

the degradation occurs when the membrane is degraded from chemical attack associated with radical formation [34].

Moreover, there is an appearance of a platinum (Pt) band (see Figure 4.14) which can be seen as white specks within the cathode electrolyte layer. The location of the Pt band is correlated to the cathode side where most of the fluoride ion is released. The membrane degradation is believed to initially take place at the cathode electrolyte layer and later degraded at the anode electrolyte layer. By using an electron dispersive (EDS) collector the Pt band formation can be confirmed as shown in Figure 4-15. The Pt band is believed to be accelerated by H_2O_2 production from reactant crossover, and then the radial formation enhances the membrane decomposition [25].

(a) (b)

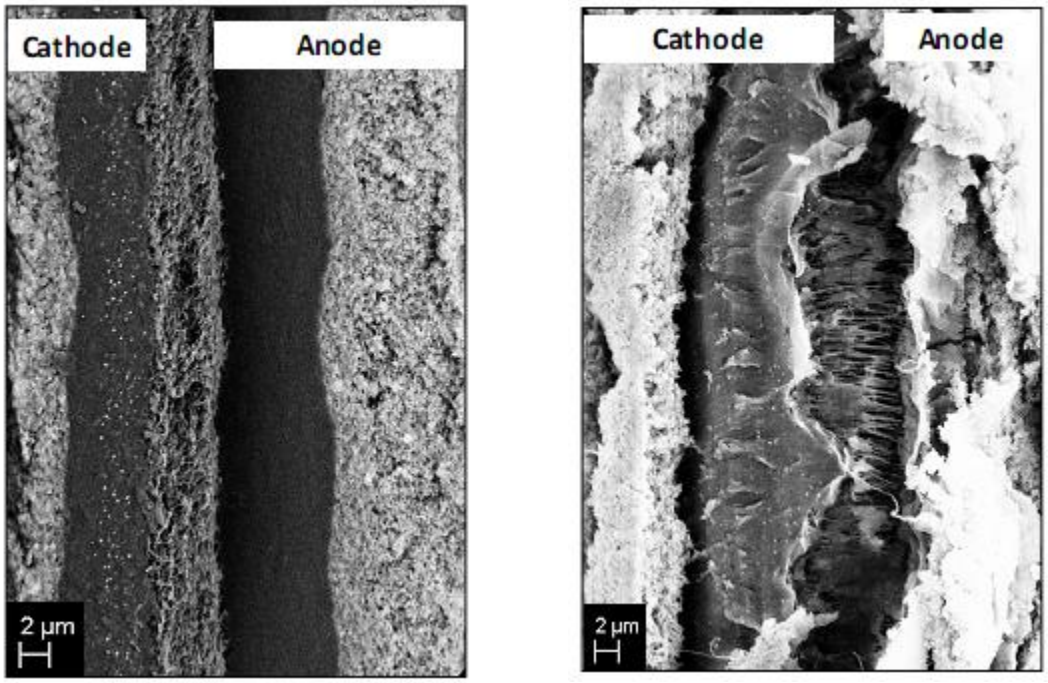

Figure 4-14. SEM cross-sectional layers of (a) 100% RH cell (Run 1) with 27.5 µm thickness (5000x magnification) and (b) H_2-air RH cycling cell (Run 2) with 34 µm thickness (5000x magnification) of Gore^{TM} 57 membranes.

For Run 2, thinning of the membrane is also observed from the cross-sectional layers; however, the thickness of the reactant RH cycling membrane is reduced not as much as the humidified cell. Note that this MEA was operated about 25% less gross time. As there was simply less time to thin the MEA, the CCM thickness is reduced to 34 µm. Importantly, the RH cycled cell shows there is a crack of the catalyst layers combined with a fusion of the membrane and the electrode as can be seen from Figure 4-14b. The fusion of the polymeric membrane and the electrolyte layers are believed to be caused by an increase of heat inside the cell during dry conditions, as well as stresses from membrane swelling/contraction during the RH cycling. The heat generated could melt the membrane and the electrode layers along with the stresses generated might later cause catalyst/membrane delamination [36]. The delamination between the catalyst and the electrolyte membrane at the cathode side can clearly be observed via the SEM cross-sectional image. The delamination or the separation of the membrane layers could lead to increased membrane resistance (there was a small amount observed at end of life as discussed earlier), loss in membrane durability and drop in overall fuel cell performance.

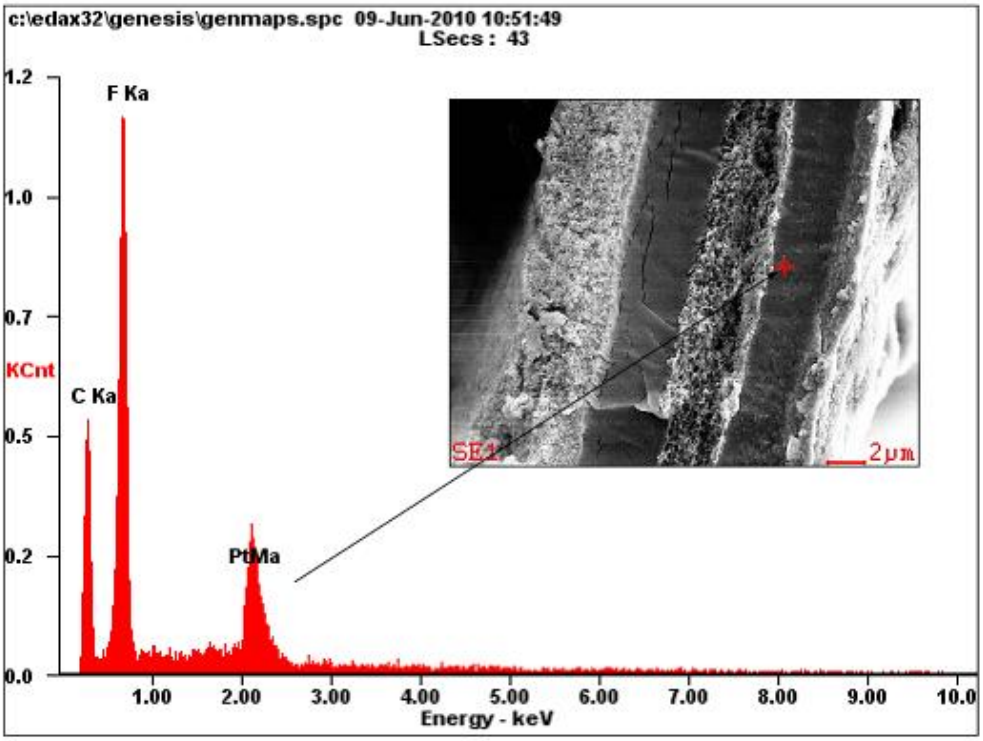

Figure 4-15. Electron dispersive (EDS) collector shows a Pt band formation of 100% RH cell (Run 1) with 27.5 µm thickness (5000x magnification).

CHAPTER 5: CONCLUSIONS AND SUGGESTIONS FOR FUTURE WORK

5.1 Conclusions

Polymer electrolyte membrane (PEM) fuel cells in certain applications (e.g. automotive) can be subjected to frequent start-stop cycles, prolonged idle conditions, and frequent current cycling due to variation from the overall power demand cycle. Hydration of the membrane and relative humidity (RH) of reactant streams are important in the development of PEM fuel cell technology. To improve the membrane durability, RH cycling operating test has currently become an interesting test. However, it is impractical and costly to run full lifetime fuel cell tests, thus accelerated durability test (i.e. operating at an idle condition to isolate impact of RH cycling, and the rapid RH cycling) is thus used to observe the effect of RH on PEM fuel cell performance. This testing method is an alternative to longer term and more costly durability testing. Key to this study is that a number of different in-situ and ex-situ diagnostic tests were used and the results of each test have been co-related. All the diagnostics confirmed membrane thinning under both idle conditions (i.e. not accelerated testing), and when the cell was RH cycled (i.e. the

accelerated test). Pinhole formation was accelerated with the RH cycling, and pinhole formation led to cell failure in both cases.

In this work, the performance of a 100% RH humidified cell (Run 1) was compared with that of RH cycling cells (Run 2 and Run 3). The results showed that the overall cell voltage degradation rates were 0.18 mV h^{-1} (Run 1), 0.24 mV h^{-1} (Run 2), and 0.3 mV h^{-1} (Run 3). An in situ test, electrochemical impedance spectroscopy was conducted to examine ohmic resistance and charge transfer resistance of these three cells. The three experiments had high charge transfer resistances due to the experiments were operated at very low current density. However, there was an increase in proton conductivity of the membranes at approximately 500 hours of Run 1, 460 hours of Run 2, and after 300 hours of Run 3. Membrane thinning and crossover current were believed to be major causes of a decrease of membrane resistance and an improvement in the membrane conductivity. Under RH cycling conditions, Run 2 and Run 3 had very high charge transfer resistances. Also, there was a shift of an increase in the ohmic resistance which was expected to mainly result from the delamination of catalyst/membrane layers.

Moreover, linear sweep voltammetry was performed to diagnose hydrogen crossover current. Clearly the RH cycling cells (Run 2 and Run 3) had a higher crossover current than Run 1; the crossover current of Run 2 and Run 3 rapidly increased and exceeded 10 mA cm^{-2}, defined as the point of membrane failure at approximately 460 hours (Run 2) and 300 hours (Run 3) of operation as indicated by a sharp rise in crossover current, and an increase in the degradation rate. These observations are thought to be indicative of pinhole formation and could be developed into a diagnostic for prediction of membrane failure (and thus stack failure).

Ion chromatography also showed that Run 2 and Run 3 had a high fluoride ion release concentration, arising from degradation of the membrane structure. Note that there was no sharp change in the fluoride release rate indicated that this diagnostic was not representative of the sudden integrity failure (i.e. a pinhole formed), although the rate was generally higher during this test. In addition, the results from infrared (IR) and scanning

electron microscopy (SEM) images illustrated that the RH cycling enhanced the stresses on the membrane by showing hot-spot/pin-hole formation, membrane thinning, membrane fusion, and membrane delamination.

Overall, the duration times of the fuel cell degradation for these three runs are consistent with the polarization curve and also other electrochemical diagnostic measurements as already discussed. The deviation of the polarization curves showed that a high failure rate of the humidified cell (Run 1) took place at approximately 620 hours. The curves also clearly presented that the RH cycling cells (Run 2 and Run 3) had expressed in high rate of membrane degradation. It was believed that the membrane failure rapidly degraded at around 460 hours and after 300 hours for the H_2-air RH cycling cell (Run 2) and H_2 RH cycling cell (Run 3), respectively.

As the results show, variation in RH dramatically reduces the overall fuel cell performance, and is a valid accelerated degradation test. It is equivalent to mechanical load which is believed to be a major driving force that could accelerate mechanical failure of the membrane in a PEM fuel cell system. The slope of the voltage degradation curve is a useful cell diagnostic for the prediction of pinhole formation which will lead to cell failure, and this failure mode has been confirmed by a number of other diagnostic tests.

5.2 Suggestions for Future Work

5.2.1 Improvement of apparatus and procedures

During running the experiments, the fuel cell test station was sometimes needed to shutdown due to a safety considerations, instability of the station, a lack of deionized water, or an unavailability of the electrochemical instrument. In effect, these led to a discontinuous relative humidity (RH) cycling condition at some times. Although in real applications, an interruption can simply occur due to a variation in the demand of power, a

non-stop RH cycling would still require for a better understanding of how the RH actually has an effect on fuel cell degradation mechanism.

For the safety issues, a web cam together with a remote desktop control could be constructed at the test station to monitor and control the station, in particularly during an unintended night time operation. This can ensure that if anything goes wrong, the station could be shut down or brought back to its normal state as soon as possible before the cell is getting damaged. Also, throughout the RH cycling tests (i.e. Run 2 and Run 3), the test station has been by-passed to operate between completely dry and humidified conditions. During dry condition with a 10 minutes operating time, H_2 anode inlet partial pressure of Run 2 starts to drop from 15 kPa to 0.5 kPa whereas the H_2 anode inlet partial pressure of Run 3 exponentially increases from 15 kPa to 150 kPa. The change of the H_2 anode inlet partial pressures of both runs are thought to be related to the variation of the water level inside the cell. However, the author also believed that the additional by-passed systems can have an effect on the inlet partial pressures. The additional by-passed valves that was used during the RH cycling conditions might affect the station's original system. Also, the by-passed systems of both runs were using different mass flow controls, this could lead to an unsteady reactant flow rates. For Run 3, a manual mass flow control was used to flow the H_2 during the H_2 RH cycling dry conditions. The H_2 by-passed valve was manually switched on/off by the author; this could cause the lag of response time and transition during the RH cycling conditions. Thus, to examine the instability of the system and further solve its problems, repeating an experiment is necessary. With different runs, the test station should be able to operate by using the same mass flow controls to ensure that the fuel cells receive exactly the same flow rates. An automatic timer and an AutoHotKey program could also be constructed to automatically control the by-passed valves. These automatic controls will give a precise dry/humidified operating time during the RH cycling of both runs.

In addition, for a more realistic durability test, the test station should also be further designed for different variation in RH values. For example, during RH cycling condition, it should be able to cycle the RH between 0 and 100% which is normally encountered in

an automobile system. Testing could also be conducted at different temperatures and higher pressures that may be experienced in automotive applications.

5.2.2 Future experiments

Previously, the effect of RH cycling in both anode and cathode gases will generate symmetrical pressure distribution across the membrane. The symmetrical wet and dry cycling on both anode and cathode induced degradation collectively, which is difficult to separate the impact of individual electrode component on the failure during cycling. However, identifying the exact cause of failure modes will be of interest, since it provides deep understanding on degradation mode. To achieve this, it can be further studied to cycle only at the cathode side or air RH cycling, whereas keeping the other side constantly at full humidification. The H_2 RH cycling and air RH cycling will generate unsymmetrical pressure distributions, stresses, high reactant cross-over across the membrane. These can increase an unbalanced force and alter a water movement inside the cell. The author believed that the results from the air RH cycling combining with the results received from the H_2 RH cycling will give more information of what are the parameters/factors that could accelerate the rate of membrane failure. Note that this work only operates one time per each run within the time allowed. However, to verify the results are not made by any 'fluke' occurrence, additional runs are required to prove the findings.

5.2.3 Development of diagnostic test from the experimental results

From the overall results of the three runs, the degradation of fuel cell could simply estimate via a voltage degradation curve. As mentioned, the voltage degradation curve is a basically plot of the average cell voltage at a constant current density against the operating time. A rapid change in slope of the curve gives a certain drop in fuel cell performance. This test has been investigated and shown that the cell voltage's degradation time is consistent with the results from the electrochemical impedance spectroscopy and linear sweep voltammetry measurements. Additionally, different types of Nafion^{TM} membranes (with different equivalent weight ionomers) that widely use from various manufacturers,

including Ion Power, Dow, Aciplex, and Flemion membranes, should be further operated and observed if the cell voltage degradation curve is valuable to confirm the membrane failure time same as a Gore^{TM} membrane. According to the test is easy and requires no additional sensors or hardware, the cell voltage degradation curve would thus useful for cell diagnostic in operating fuel cell stacks in the development of fuel cell technology.

REFERENCES

1. A. Collier, H. Wang, X.Z. Yuan, J. Zhang, D.P. Wilkinson, *Degradation of polymerelectrolyte membranes.* International Journal of Hydrogen Energy, 2006. **31**: p. 1838 - 1854.

2. J. Healy, C. Hayden, T. Xie, K. Olson, R. Waldo, M. Brundge, H. Gasteiger, and J. Abbott, *Aspects of the Chemical Degradation of PFSA Ionomers used in PEM Fuel Cells.* FUEL CELLS 2005, 2004. **5**(2): p. 302 - 308.

3. J. Zhang, Y. Tang, C. Song, Z. Xia, H. Li, H. Wang, J. Zhang, *PEM fuel cell relative humidity (RH) and its effect on performance at high temperatures.* Electrochimica Acta, 2008. **53**: p. 5315-5321.

4. S. Kundu, *Development and Application of a Chemical Degradation Model for Reinforced Electrolyte Membranes in Polymer Electrolyte Membrane Fuel Cells*, in *Chemical Engineering*. 2008, University of Waterloo: Waterloo. p. 194.

5. J. Wu, X. Z. Yuan, J.J. Martin, H. Wang , J. Zhang, J. Shen, S. Wu, W. Merida, *A review of PEM fuel cell durability: Degradation mechanisms and mitigation strategies.* Journal of Power Sources, 2008. **184**: p. 104 - 119.

6. EG&G Technical Services, Science Applications International Corporation, *Fuel Cell Handbook*. 6th ed. 2002, West Virginia, USA.

7. Canadian Hydrogen and Fuel Cell Association, Hydrogen Economy. 2008: 4250 Wesbrook Mall, Vancouver, B.C. V6T 1W5.

8. J. Larminie, A. Dicks, *Fuel Cell Systems Explained*. 2nd ed. 2003: John Wiley & Sons Ltd.

9. J. Gostick, Multiphase Mass Transfer and Capillary Properties of Gas Diffusion Layers for Polymer Electrolyte Membrane Fuel Cells in Chemical Engineering. 2008, University of Waterloo: Waterloo. p. 225.

10. S. Thomas, M. Zalbowitz, *Fuel cells - Green Power*. 2000, Los Alamos National Laboratory: New Maxico.

11. W. Roberto, M. Donis, *Diagnosis of PEMFC Stack Failures via Electrochemical Impedance Spectroscopy*, in *Department of Mechanical Engineering* 2002, University of Victoria.

12. R.J. Wayne, *Durability Studies on Polymer Electrolyte Membrane Fuel Cells*, in *Department of Materials Science and Engineering*. 2004, Case Western Reserve University. p. 120.

13. V. Mehta, J.S. Cooper, *Review and analysis of PEM fuel cell design and manufacturing.* Journal of Power Sources, 2003. **114**: p. 32 - 53.

14. W. Liu, K. Ruth, and G. Rusch, *Membrane Durability in PEM Fuel Cells.* Journal of New Materials for Materials for Electrochemical Systems, 2001. **4**: p. 227 - 231.

15. K. Panha, *Literature Reviews on Membrane Durability in PEMFCs*. 2008, University of Waterloo: Waterloo.

16. H. Tang, S. Peikang, S. P. Jiang, F. Wang, M. Pan, *A degradation study of Nafion proton exchange membrane of PEM fuel cells.* Journal of Power Sources, 2007. **170**: p. 85–92.

17. S. Kundu, L.C. Simon, M. Fowler, S. Grot, *Mechanical properties of Nafion^{TM} electrolyte membranes under hydrated conditions.* Polymer, 2005. **46**: p. 11707-11715.

18. T. Okada, G. Xie, Y. Tanabe, *Theory of water management at the anode side of polymer electrolyte fuel cell membranes.* Journal of Electroanalytical Chemistry, 1996. **413**: p. 49-65.

19. J. Yu, T. Matsuura, Y. Yoshikawa, Md N. Islam, M. Hori, *Life time behavior of a PEM fuel cell with low humidication of feed stream.* Phys. Chem. Chem. Phys., 2004. **7**: p. 373 - 378.

20. Tao Gu, W.K. Lee, J. W. Van Zee, *Quantifying the'reverse water gas shift' reaction inside a PEM fuel cell.* AppliedCatalysisB:Environmental, 2005. **56**: p. 43–49.

21. J. St-Pierre, D.P. Wilkinson, S. Knights, M. Bos, *Relationships between water management, contamination and lifetime degradation in PEFC.* Journal of New Materials for Electrochemical Systems, 2000. **3**: p. 99 - 106.

22. X. Deng, G. Liu, George Wang, Min Tan, *Modeling and identication of a PEM fuel cell humidication system.* J Control Theory Appl, 2009. **7**(4): p. 373-378.

23. D. Chen, H. Peng, *A Thermodynamic Model of Membrane Humidifiers for PEM Fuel Cell Humidification Control*. 2005, ASME.

24. G. Pourcelly, A. Oikonomou, C. Gavach, *Influence of the water content on the kinetics of counter-ion transport in perfluorosulphonic membranes.* J. Electroanal. Ckem., 1998. **287**: p. 43-59.

25. Z. Qi, A. Kaufman, *Improvement of water management by a microporous sublayer for PEM fuel cells.* Journal of Power Sources, 2002. **109**: p. 38-46.

26. R. Baldwin, M. Pham, A. Leonida, J. Mcelroy, T. Nalette, *Hydrogen-Oxygen Proton Exchange Membrane Fuel Cells and Electrolyzers.* Journal of Power Sources, 1990. **29**: p. 399 - 412.

27. Z. Qi, A. Kaufman, *PEM fuel cell stacks operated under dry-reactant conditions.* Journal of Power Sources, 2002. **109**: p. 469-476.

28. L. Carrette, K.A. Friedrich, U. Stimming, *FuelCells: Fundamentals and Applications.* 2001. **1**(1).

29. M. Shi, F.C. Anson, *Dehydration of protonated Nafion coatings induced by cation exchange and monitored by quartz crystal microgravimetry.* Journal of Electroanalytical Chemistry, 1997. **425**: p. 117-123.

30. C. Huang, K.S. Tan, J. Lin, K. L. Tan, *XRD and XPS analysis of the degradation of the polymer electrolyte in H2-O2 fuel cell.* Chemical Physics Letters, 2003. **371**: p. 80 - 85.

31. S. Kundu, K. Karan, M. Fowler, L.C. Simon, B. Peppley, E. Halliop, *Influence of micro-porous layer and operating conditions on the fluoride release rate and degradation of PEMFC membrane electrode assemblies.* Journal of Power Sources, 2008. **179**: p. 693-699.

32. A. Ohma, S. Suga, S. Yamamoto, K. Shinohara, *Membrane Degradation Behavior during Opeon-Circuit Voltage Hold Test.* Journal of The Electrochemical Society, 2007. **154**(8): p. B757-B760.

33. C. Paik, T. Skiba, V. Mittal, S. Motupally, T.D. Jarvi. *Membrane degradation studies under accelerated conditions in PEMFC.*

34. S. Kocha, J.D. Yang, J.S. Yi, *Characterization of Gas Crossover and Its Implications in PEM Fuel Cells.* AIChEJournal, 2006. **52**(5).

35. M. Inaba, T. Kinumoto, M. Kiriake, R. Umebayashi, A. Tasaka , Z. Ogumi, *Gas crossover and membrane degradation in polymer electrolyte fuel cells.* Electrochimica Acta, 2006. **51**: p. 5746 – 5753.

36. M.W. Fowler, R.F. Mann, J.C. Amphlett, B.A. Peppley, P.R. Roberge, *Incorporation of voltage degradation into a generalised steady state electrochemical model for a PEM fuel cell.* Journal of Power Sources, 2002. **106**: p. 274 - 283.

37. M. Crum, W. Liu, *Effective Testing Matrix for Studying Membrane Durability in PEM Fuel Cells: Part 2. Mechanical Durability and Combined Mechanical and Chemical Durability.* ECS Transactions, 2006. **3**(1): p. 541 - 550.

38. R. Borup, J. Davey, S. Pacheco, D. Wood, J. Xie, Michael Inbody and Fernando Garzon. *Durability issues of the PEMFC GDL and MEA under steady-state and drive-cycle operating conditions*.

39. C. Huang, Z.S. Liu, D.Q. Mu, *The Mechanical Changes in the MEA of PEM Fuel Cells due to Load Cycling.* ECS Transactions, 2008. **16**(2): p. 1987-1996.

40. X. Huang, W. Yoon, *Inhomogeneous Degradation of Polymer Electrolyte Membrane in PEM Fuel Cells* in *216th ECS Meeting*. 2008. Vienna, Austria: The Electrochemical Society.

41. R. Solasi, Y. Zou, X. Huang, K. Reifsnider, D. Condit, *On mechanical behavior and in-plane modeling of constrained PEM fuel cell membranes subjected to hydration and temperature cycles.* Journal of Power Sources, 2007. **167**: p. 366-377.

42. Xi. Huang, R. Solasi, Y. Zou, M. Feshler, K. Reifsnider, D. Condit, S. Burlatsky, T. Madden, *Mechanical Endurance of Polymer Electrolyte Membrane and PEM Fuel Cell Durability*. Journal of Polymer Science: Part B: Polymer Physics, 2006. **44**: p. 2346-2357.

43. M.B. Satterfield, P.W. Majsztrik, H. Ota, J.B. Benziger, A.B. Bocarsly, *Mechanical Properties of Nafion and Titania/Nafion Composite Membrances for Polymer Electrolyte Membrane Fuel Cells.* Journal of Polymer Science, 2006. **44**: p. 2327-2345.

44. J. Benziger, E. Chia, J.F. Moxley, I.J. Kevrekidis, *The dynamic response of PEM fuelcells to changes in load.* Chemical Engineering Science, 2005. **60**: p. 1743-1759.

45. S. Zhang, X. Yuan, H. Wang, W. Merida, J. Shen, S. Wu, J. Zhang, H. Zhu, *A review of accelerated stress tests of MEA durability in PEM fuel cells.* International Journal of Hydrogen Energy, 2009. **34**: p. 388–404.

46. B. Yang, Y.Z. Fu, A. Manthiram, *Operation of thin Nafion-based self-humidifying membranes in proton exchange membrane fuel cells with dry O_2 and H_2*. Journal of Power Sources, 2005. **139**: p. 170–175.

47. H. Uchida, Y. Ueno, H. Hagihara, M. Watanabe, *Self-Humidifying Electrolyte Membranes for Fuel Cells: Preparation of Highly Dispersed TiO_2 Particles in Nafion 112.* Journal of The Electrochemical Society, 2003. **150**(1): p. A57-A62.

48. G.H. Guvelioglu, H.G. Stenger, *Flow rate and humidification effects on a PEM fuel cell performance and operation.* Journal of Power Sources, 2007. **163**: p. 882–891.

49. D. Chen, H. Peng, *Analysis of Non-Minimum Phase Behavior of PEM Fuel Cell Membrane Humidification Systems*, in *American Control Conference*. 2005: Portland, OR, USA.

50. G. Vasu, A.K. Tangirala, B. Viswanathan, K.S. Dhathathreyan, *Continuous bubble humidification and control of relative humidity of H_2 for a PEMFC system.* International Journal of Hydrogen Energy, 2008. **33**: p. 4640–4648.

51. M.V. Williams, H.R. Kunz, J.M. Fenton, *Operation of Nafion -based PEM fuel cells with no external humidification: influence of operating conditions and gas diffusion layers.* Journal of Power Sources, 2004. **135**: p. 122–134.

52. F.N. Buchit, S. Srinivasan, *Operating Proton Exchange Membrane Fuel Cells Without External Humidification of the Reactant Gases.* The Electrochemical Society, 1997. **144**(8): p. 2767-2772.

53. E.D. Wang, P.F. Shi, C.Y. Du, *Novel self-humidifying MEA with water transfer region for PEM fuel cells*. 2008, Department of Applied Chemistry, Harbin Institute of Technology: Harbin, PR China.

54. F. Liu, B. Yi, D. Xing, Ji. Yu, Z. Hou, Y. Fu, *Development of novel self-humidifying composite membranes for fuel cells.* Journal of Power Sources, 2003. **124**: p. 81–89.

55. Y. Zhang, H. Zhang, X. Zhu, C. Bi, *Promotion of PEM Self-Humidifying Effect by Nanometer-Sized Sulfated Zirconia-Supported Pt CatalystHybrid with Sulfonated Poly(EtherEtherKetone).* J. Phys. Chem. B, 2007. **111**: p. 6391-6399.

56. C. Wang, Z. Mao, J. Xu, X. Xie, L. Yang, *Preparation of a self-humidifying membrane electrode assembly for fuel cell and its performance analysis.* Science in China, 2003. **46**(501-508).

57. X.-B. Zhu, H.-M. Zhang, Y.-M. Liang, Y. Zhang, B.-L. Yi, *A Novel PTFE-Reinforced Multilayer Self-Humidifying Composite Membrane for PEM Fuel Cells.* Electrochemical and Solid-State Letters, 2006. **9**(2): p. A49-A52.

58. X. Zhu, H. Zhang, Y. Zhang, Y. Liang, X. Wang, B. Yi, *An Ultrathin Self-Humidifying Membrane for PEM Fuel Cell Application: Fabrication, Characterization, and Experimental Analysis.* J. Phys. Chem. B, 2006. **110**: p. 14240-14248.

59. E. Endoh, S. Terasono, H. Widjaja, Y.Takimoto, *Degradation Study of MEA for PEMFCs under Low Humidity Conditions.* Electrochemical and Solid-State Letters, 2004. **7**(7): p. A209 - A211.

60. J.F. Chiou, D.R. Paul, *Gas Permeation in a Dry Nafion Membrane*. Ind. Eng. Chem. Res., 1988. **27**: p. 2161 - 2164.

61. B. Wahdame, D. Candusso, F. Harel, X. Francois, M.C. Pera, D. Hissel, J.-M. Kauffmann, *Analysis of a PEMFC durability test under low humidity conditions and stack behaviour modelling using experimental design techniques.* Journal of Power Sources, 2008. **182**: p. 429–440.

62. J. Yu, T. Matsuura, Y. Yoshikawa, Md N. Islam, M. Hori, *In Situ Analysis of Performance Degradation of a PEMFC under Nonsaturated Humidification.* Electrochemical and Solid-State Letters, 2005. **8**(3): p. A156 - A158.

63. S. Yoshioka, A. Yoshimura, H. Fukumoto, O. Hiroi, H. Yoshiyasu, *Development of a PEM fuel cell under low humidified conditions*. 2005, Advanced Technology R&D Center, Mitsubishi Electric Corporation.

64. E. Endoh, *Highly Durable MEA for PEMFC Under High Temperature and Low Humidity Conditions* 2006, ECS Transactions, The Electrochemical Society. p. 9-18.

65. R. Borup, J. Meyers, B. Pivovar, Y.S. Kim, R. Mukundan, N. Garland, D. Myers, M. Wilson, F. Garzon, D. Wood, P. Zelenay, K. More, K. Stroh, T. Zawodzinski, J. Boncella, J.E. McGrath, M. Inaba, K. Miyatake, M. Hori, K. Ota, Z. Ogumi, S. Miyata, A. Nishikata, Z. Siroma, Y. Uchimoto, K. Yasuda, K. Kimijima, N. Iwashita, *Scientific Aspects of Polymer Electrolyte Fuel Cell Durability and Degradation.* Chemical Reviews, 2007. **107**: p. 3904-3951.

66. W. Gu, B. Litteer, R. Makharia, H.A. Gasteiger, B. Brady, M. Budinski, E. Thompson, F.T. Wagner, S.G. Yan, P.T. Yu, *Catalyst degradation mechanisms in PEM and direct methanol fuel cells*. 2008, Italy General Motors Corporation: Honeoye Falls. p. 225-233.

67. X.-Z. Yuan, C. Song, H. Wang, J. Zhang, *Electrochemical Impedance Spectroscopy in PEM Fuel Cells: Fundamentals and Applications*. 2009, Vancouver: Springer.

68. S. Cleghorn, J. Kolde, W. Liu in: W. Vielstich, H. Gasteiger, A. Lamm (Eds.), *Handbook of Fuel Cells—Fundamentals, Technology and Applications*. John Wiley & Sons, New York, 2003. **3**: p. 566–575.

69. Eco Chemie B.V., *Autolab Manual*. 2007: Utrecht, Netherland.

70. V. Singaram, *Development of efficient materials and MEA fabrication methods to improve the performance of PEM fuel cells*, in *Energy conversion Technology*. 2007, University of Science and Technology, South korea.

71. X. Yuan, S. Zhang, J. Wu, C. Sun, H. Wang, *Post analysis on MEA degradation: IR Imaging*. 2010, National Research Council Canada Institute for Fuel Cell Innovation.

72. C. Ma, L. Zhang, S. Mukerjee, D. Ofer, B. Nair, *An investigation of proton conduction in select PEM's and reaction layer interfaces designed for elevated temperature operation.* Journal of Membrane Science, 2003. **219**: p. 123 - 136.

APPENDIX A: FUEL CELL ASSEMBLY PROCEDURES

Tandem TP50 PEM fuel cell assembly procedure used in this project is presented in this section. Figure A-1 shows TP50 fuel cell components.

Figure A-1. Components of a single TP50 PEM fuel cell.

The fuel cell assembly procedure involves the following steps:

1) A manifold plate is firstly set on a support stand mount. The manifold fluid inlet/outlet plate consists of six fittings. On either side, three fittings are provided for flowing inlet and outlet reactants (anode, cathode, and cooling water). The manifold plate is placed into two small Teflon guide rods which inserted at the two corners of the end plate (Figure A-2).

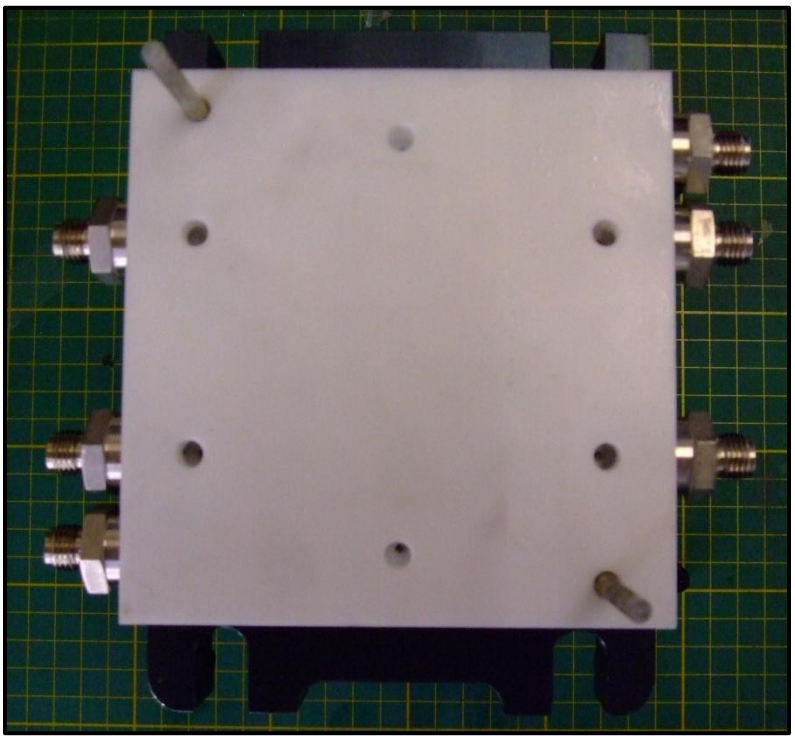

Figure A-2. A manifold plate of a TP50 PEM fuel cell.

2) An anode buss plate with six o-ring silicones (Figure A-3) is then located on the manifold plate followed by an anode cooling water plate (Figure A-4). The cooling water plate is used to control temperature inside the fuel cell by flowing water from water inlet fitting through water outlet fitting.

Figure A-3. An anode buss plate with six o-ring silicones.

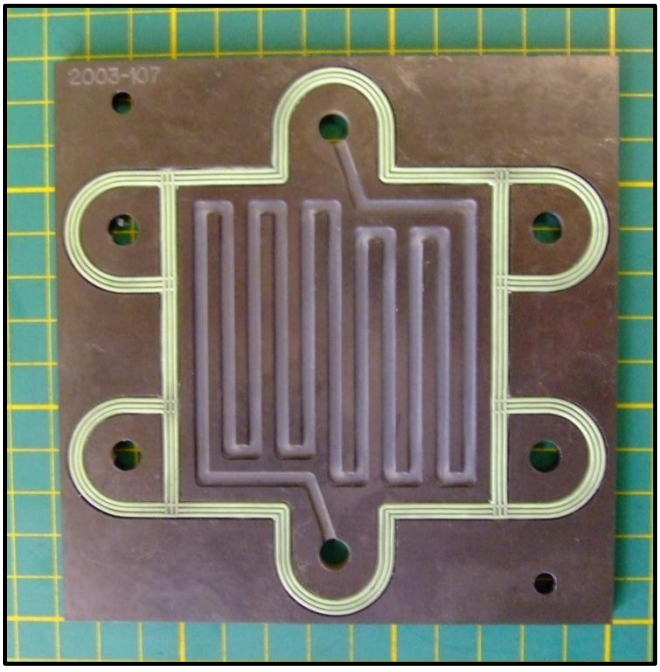

Figure A-4. An anode cooling water plate.

3) An anode flow field plate (Figure A-5) is later placed on the top of the cooling water plate. Next, it is a membrane electrode assembly (MEA) which consists of Gore™ membrane and kapton gaskets. The membrane is framed by the kapton gaskets. Two gas diffusion layers (GDLs) with a microporous layer are located on each side of the membrane as shown in Figure A-6.

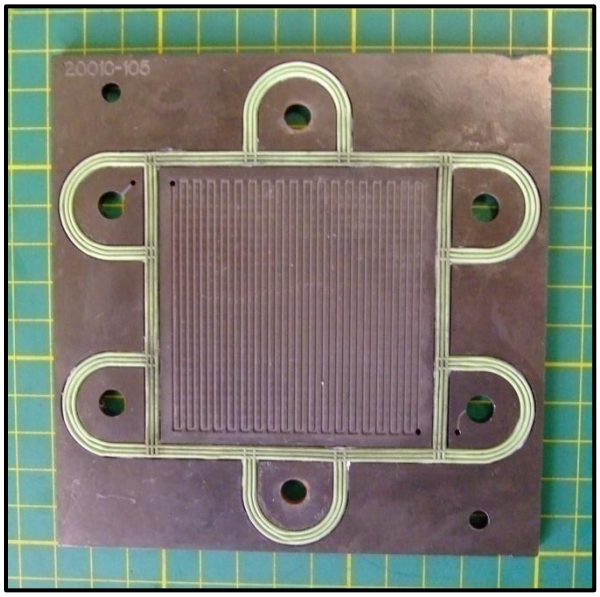

Figure A-5. An anode flow field plate.

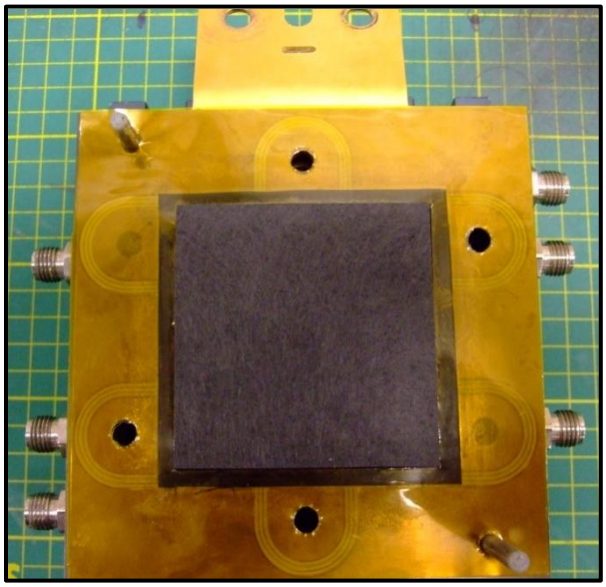

Figure A-6. A membrane electrode assembly (MEA) and gas diffusion layers (GDLs).

4) Same as the anode side by the following orders; a cathode flow field plate (Figure A-7a), a cathode cooling water plate (Figure A-7b), and a cathode buss plate (Figure A-7c) are placed against the MEA.

(a) (b)

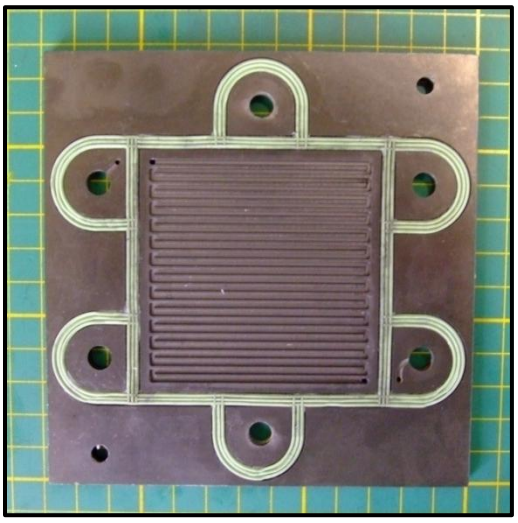

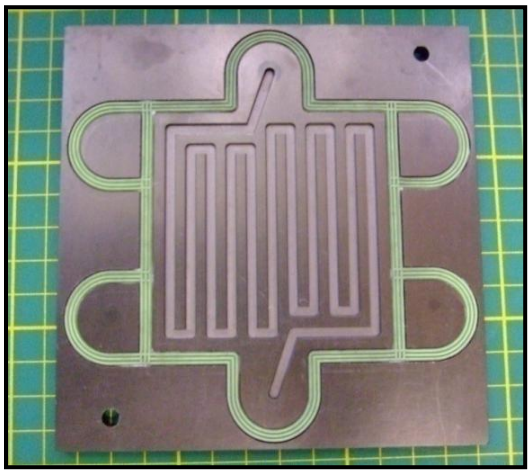

(c)

Figure A-7. Cathode plates (a) flow field plate, (b) cooling water plate, and (c) buss plate.

5) An electrical/thermal isolation plate (Figure 4-8) and a compression endplate (Figure 4-9) are set on the top of the assembled fuel cell.

Figure 4-8. An electrical/thermal isolation plate.

Figure 4-9. A compression endplate.

6) Finally, components are compressed with four tie-rods (Figure 4-10) by hand-tight in a start-cross manner so that pressure is distributed evenly upon all components of the fuel cell. The fuel cell is then tightened further using 100 psi N_2. During fuel cell operation, the cell can be able to monitor cell compression via an integrated pressure gage which is constructed at the compression endplate. Figure 4-11 shows a complete TP50 fuel cell assembly.

Figure 4-10. Four tie-rods.

Figure 4-11 A TP50 fuel cell assembly.

APPENDIX B: FUEL CELL TEST STATION OPERATION

In this section, a generally starting up, operating, purging, and shutting down a G50 fuel cell test station will be described as follows:

B1. Startup the test station

Starting the test station includes:

1) Once PEM fuel cell is assembled and installed, the fuel cell is compressed with 100 psi N_2 gas.

2) The fuel cell is heated-up to 70 °C using a water bath. The water bath is set at 75 °C in order to get the required cell temperature.

3) Power up the test station.

4) Turn on all gas supply valves; H_2 gas, an in house air, and N_2 gas.

5) Start LabView control system program.

6) On the 'Setup' at 'Station' page, set number of cells (i.e., 1 cell) and cells active area (i.e., 42.25 cm^2).

7) Click the 'Start' button at a side-bar. The system will switch from 'OFF' state to 'Setup' state.

B2. Running the test station

To run the test station:

1) Press 'Fuel ON' and 'Gas ON' to let H_2 gas and the air flow to the station.

2) Check water level of the two humidifiers. Both humidifiers must have enough water in the water tubes.

3) Click 'To LoadCtrl' button. The system will switch to the 'LoadCtrl' state.

4) Click 'Connect' button in the side-bar. The button label changes to 'Connected'. The system now establishes the connection between the load box and the fuel cell. Now, the station can be able to produce power as a required load. The 'Connect' button is active when the system is in the 'Load Ctrl' state only.

5) To use data logging, go to the side-bar and click ‘Logging’ button to ‘ON’. Data logging can be turned on at any time when the test information is required to record in the log file.

6) Control the gas flow rates by entering the flow rate values at the side-bar and click ‘Set’ button. The feedback values for the anode and cathode flows are displayed on the right side of the slider.

7) To control the current, entering the current values at the side-bar and click ‘Set’.

8) To control the gas pressures, under the ‘Pressure’ control in the side-bar, type new values for the anode and cathode, or use the sliders to change the pressures. Click ‘Set’ button. The feedback values for the inlet and outlet pressures for both anode and cathode are displayed in the feedback boxes to the right.

9) To manually control the temperatures, under the ‘Temperature’ control in the side-bar, specify values for dew points (DP in °C) for the anode and cathode flows. It is normal in practice to set the gas and inlet temperatures a litter bit higher than the dew point to avoid condensation problems.

10) Set gas temperature set points for the anode and cathode flows and click the ‘Set’ button after entering each value.

11) Once you have completed the test, return the load to 0 A (Open circuit voltage), ramp down the fuel cell, and then click the ‘To Setup’ or ‘Shutdown’ button.

B3. Purging the test station

Before start or shut down the test station, purging by N_2 is performed as follows:

1) Initially, make sure that the load box ‘Connect’ button is disconnected. The ‘Connect’ button should appear in grey color.

2) At ‘Station’ page on the ‘Setup’, go to the gas purge section.

3) In the purge time field, specify the duration for the purge; set at 30 minutes.

4) Click the ‘Purge Start’ button. The N_2 valve will automatic turn on and flow the N_2 into the fuel cell.

B4. Shutdown the test station

After purging the fuel cell, shutting down the test station can be done as follows:

1) Make sure the system in the ‘Setup’ state. If it isn’t, click the ‘To Setup’ button.

2) Click the ‘Shutdown’ button. The test station will shut down and switch to the ‘OFF’ state. The ‘Shutdown’ button will now show ‘Start’.

3) At ‘Station’ page on the ‘Setup’, click the ‘Exit Software’ button.

4) Close all gas supply valves; H_2 gas, the air line, and N_2 gas.

5) Turn the water bath off.

6) Slowly depressurize the fuel cell.

APPENDIX C: POLARIZATION CURVE PROCEDURE

A fuel cell performance testing, polarization curve, is presented in this section as follows:

1. Start up – See start up the test station
2. Logging interval to 1 minute
3. Stoichiometric ratio to 1.5:2.5 (anode:cathode)
4. Set temperatures to 70.65.60 (cell.anode and cathode inlet temperatures.anode and cathode dew temperatures).
5. Set the water bath at 75 ºC to achieve the desired cell temperature.
6. Set pressures of H_2 gas and air to 100 kPa.
7. Once temperatures have reached the set points, set H_2 and air flow rates at 0.113 and 0.358 slpm.
8. Click 'To Load Ctrl' button to connect the loadbox to the system.
9. Set current at OCV for 3 minutes and first record the OCV value.
10. Begin raising the current and the flow rates followed a standard flow chart. *Note that the flow rates must be adjusted to match each current density as to maintain the correct stoichiometric ratios in the cell.
11. Record the voltage value at each current density with a 1 minute interval.
12. Continue raising current until the voltage becomes unstable or cell voltage drops below 0.3 V. This usually corresponds to a current density of about 1.5 A cm^{-2}.
13. The current densities to be tested are 1.6, 1.5, 1.4, 1.3, 1.2, 1.1, 1.0, 0.9, 0.8, 0.7, 0.6, 0.5, 0.4, 0.3, 0.2, 0.1, 0.05, 0.02, 0.01, 0 A cm^{-2}.
14. Once the loadbox displays an unstable voltage, immediately decreases the current and the flow rates until back to the OCV.
15. By plotting voltage against current density, the polarization curve can be constructed.

APPENDIX D: SAMPLE DATA AND SAMPLE CALCULATIONS

D1. Sample data

D1.1 Run 1: 100% RH humidified cell

ICY
MODEL1_G57
Date: 2009-06-19
Time (hr:min:sec) = 13:44:12
Stack Active Area (cm^2) = 42.25

Description	CVM Cell Voltage	Current Density	Anode and Cathode dP	Anode Inlet Pressure
Unit	V	mAmp/cm^2	kPa	kPag
Time (min:sec:millisec)	data_cell_001V	current_density	FCIM_pressure_an_ca_diff	FCIM_pressure_an_PT_411
44:12.0	0.922819	2.666667	12.795115	21.802204
45:12.5	0.840175	14.285714	12.710937	21.802204
46:12.5	0.840358	14.285714	12.54258	21.718025
47:12.5	0.838954	14.285714	12.542581	21.381311
48:12.5	0.837184	14.285714	12.879293	21.633846
49:12.5	0.835963	14.285714	12.458402	21.633846
50:12.5	0.834986	14.285714	12.458402	21.718025
51:12.5	0.83401	14.285714	13.131829	22.054739
52:12.5	0.833827	14.285714	11.616618	21.802204
53:12.5	0.833399	14.285714	13.216008	21.97056
54:12.5	0.834254	14.285714	12.795115	21.718025
55:12.5	0.836634	14.285714	13.131829	21.128777
56:12.5	0.836573	14.285714	12.542582	20.707886
57:12.5	0.836268	14.285714	12.290045	20.202814
58:12.5	0.835902	14.285714	11.616619	19.781923
59:12.5	0.834986	14.285714	11.364082	19.529387
00:12.5	0.834193	14.285714	11.364083	19.361031
01:12.5	0.833277	14.285714	11.279904	19.276852
02:12.5	0.832606	14.285714	11.027369	19.024317
03:12.5	0.831263	14.285714	10.690657	18.603424
04:12.5	0.830164	14.285714	10.606479	18.855961
04:04.5	0.82931	14.285714	10.859014	18.855961
05:04.5	0.82754	14.285714	11.027369	18.940138
06:04.5	0.82461	14.285714	10.269765	20.118635
07:04.5	0.820215	14.285714	10.690656	21.97056
08:04.5	0.820704	14.285714	12.879294	24.07502
09:04.5	0.82107	14.285714	13.889435	24.748447
10:04.5	0.822047	14.285714	13.889434	24.159199
11:04.5	0.822047	14.285714	13.636899	23.56995
12:04.5	0.821375	14.285714	14.226148	23.654129
13:04.5	0.821436	14.285714	13.552721	23.233236
14:04.5	0.820826	14.285714	13.805256	22.728167
15:04.5	0.820765	14.285714	13.636899	22.896523
16:04.5	0.821131	14.285714	12.710938	22.559809
17:04.5	0.820338	14.285714	13.889434	22.643988
18:04.5	0.820338	14.285714	14.057791	21.97056
19:04.5	0.821558	14.285714	12.037511	21.802204
20:04.5	0.822962	14.285714	12.963472	21.46549

Description	Anode Inlet Temperature	Anode Outlet Pressure	Cathode Inlet Pressure	Cathode Outlet Pressure
Unit	C	kPag	kPag	kPag
Time (min:sec:millisec)	FCIM_temp_an_TC_412	FCIM_pressure_an_PT_412	FCIM_pressure_ca_PT_431	FCIM_pressure_ca_PT_432
44:12.0	71.300003	0.589249	9.175445	0.673427
45:12.5	71.300003	0.841784	9.175445	0.589249
46:12.5	71	0.589249	8.670375	0.589249
47:12.5	70.800003	0.589249	8.92291	0.673427
48:12.5	70.5	0.336714	9.175445	0.841784
49:12.5	70.300003	0.420892	9.259624	0.589249
50:12.5	70	0.336714	9.42798	0.673427
51:12.5	69.599998	0.673427	8.838732	0.589249
52:12.5	69.300003	0.336714	10.017229	0.673427
53:12.5	69.099998	0.673427	8.838732	0.673427
54:12.5	69	0.589249	8.502018	0.673427
55:12.5	68.900002	0.420892	8.333661	0.673427
56:12.5	68.900002	0.589249	8.165304	0.673427
57:12.5	68.900002	0.589249	7.912769	0.589249
58:12.5	69.099998	0.420892	8.165304	0.673427
59:12.5	69.599998	0.589249	7.996947	0.673427
00:12.5	70.099998	0.589249	7.996947	0.673427
01:12.5	70.599998	0.420892	7.996947	0.673427
02:12.5	71	0.420892	8.165304	0.841784
03:12.5	71.099998	0.420892	8.249482	0.673427
04:12.5	71.199997	0.336714	8.165304	0.841784
04:04.5	71.300003	0.420892	8.165304	0.841784
05:04.5	71.300003	0.336714	8.838732	0.841784
06:04.5	71.199997	0.420892	9.259624	0.673427
07:04.5	71.099998	0.420892	11.027369	0.673427
08:04.5	71	0.420892	11.279904	0.673427
09:04.5	70.699997	0.673427	10.438121	0.589249
10:04.5	70.599998	0.420892	10.185586	0.589249
11:04.5	70.400002	0.420892	9.680515	0.841784
12:04.5	70.099998	0.925962	9.175445	0.420892
13:04.5	70	0.589249	9.259624	0.673427
14:04.5	69.800003	0.589249	8.838732	0.673427
15:04.5	69.599998	0.420892	9.259624	0.841784
16:04.5	69.599998	0.336714	9.764693	0.841784
17:04.5	69.599998	0.925962	8.586196	0.589249
18:04.5	69.5	0.252535	8.92291	1.010141
19:04.5	69.599998	0.252535	9.680515	0.925962
20:04.5	69.599998	0.673427	8.502018	0.589249
21:04.5	69.599998	0.420892	8.502018	0.841784
22:04.5	69.699997	0.589249	8.249482	0.673427
23:04.5	69.800003	0.420892	7.996947	0.841784
24:04.5	69.800003	0.420892	7.996947	0.673427
25:04.5	69.900002	0.252535	7.996947	0.925962
26:04.5	70	0.420892	8.165304	0.841784
27:04.5	70	0.420892	8.165304	0.673427
28:04.5	70	0.420892	7.996947	0.841784
29:04.5	70	0.420892	8.249482	0.841784
30:04.5	70.099998	0.673427	8.165304	0.589249
31:04.5	70.099998	0.420892	8.333661	0.673427
32:04.5	70.199997	0.589249	8.249482	0.589249
33:04.5	70.199997	0.589249	8.586196	0.673427
34:04.5	70.199997	0.420892	9.259624	0.841784

Description	Anode and Cathode dT	Cathode Inlet Temperature	Cell Temperature	H2 Detector LEVEL
Unit	C	C	C	%
Time (min:sec:millisec)	FCIM_temp_an_ca_diff	FCIM_temp_ca_TC_432	FCIM_temp_ca_TC_433	FM_input_HD_1_LVL
44:12.0	2.300003	69	74	6.392157
45:12.5	0	71.300003	74.400002	6.862745
46:12.5	2.200005	73.300003	74.400002	6.235294
47:12.5	4.199997	75	74.599998	6.392157
48:12.5	5.599998	76.099998	74.599998	6.235294
49:12.5	6.699997	77	75	7.176471
50:12.5	8.699997	78.699997	74.800003	6.54902
51:12.5	9.400002	79	74.800003	6.705883
52:12.5	9.5	78.800003	74.800003	6.392157
53:12.5	9.099998	78.199997	74.699997	6.392157
54:12.5	7.900002	76.900002	74.900002	6.392157
55:12.5	6.5	75.400002	74.800003	6.54902
56:12.5	4.900002	73.800003	74.699997	6.705883
57:12.5	3.099998	72	74.800003	6.392157
58:12.5	1	70.099998	74.900002	6.54902
59:12.5	1.099998	68.5	75	6.54902
00:12.5	3.5	66.599998	74.800003	6.392157
01:12.5	5.799995	64.800003	74.900002	7.647059
02:12.5	7.900002	63.099998	74.900002	6.54902
03:12.5	9.299999	61.799999	74.800003	6.54902
04:12.5	10.399998	60.799999	75	7.490196
04:04.5	10.700005	60.599998	75.099998	6.54902
05:04.5	9.999996	61.200001	75	6.078432
06:04.5	8.299995	62.799999	75	6.54902
07:04.5	6.099998	65	75	7.647059
08:04.5	4.5	66.5	74.800003	7.490196
09:04.5	3.800003	67	75	7.333333
10:04.5	2.5	68.099998	74.800003	7.960784
11:04.5	0.200005	70.199997	74.800003	7.490196
12:04.5	2.099998	72.199997	74.900002	7.960784
13:04.5	4	74	75	7.490196
14:04.5	6	75.800003	75	7.647059
15:04.5	7.400002	77	74.800003	7.803922
16:04.5	8.400002	78	74.900002	7.490196
17:04.5	8.800003	78.300003	75	8.117647
18:04.5	10.099998	79.599998	74.900002	6.54902
19:04.5	9.400002	79	75.300003	8.117647
20:04.5	8.599998	78.199997	74.900002	7.647059
21:04.5	7.5	77.099998	75	7.647059
22:04.5	5.800003	75.5	75	6.392157
23:04.5	3.899994	73.699997	74.900002	6.392157
24:04.5	2.099998	71.900002	74.699997	6.392157
25:04.5	0.299995	70.099998	74.699997	7.647059
26:04.5	1.699997	68.300003	74.900002	6.54902
27:04.5	3.400002	66.599998	74.900002	6.705883
28:04.5	5	65	74.900002	6.54902
29:04.5	5.900002	64.099998	74.800003	6.392157
30:04.5	7.099998	63	74.800003	6.54902
31:04.5	8.299999	61.799999	74.900002	6.392157
32:04.5	9.099998	61.099998	74.599998	6.54902
33:04.5	8.799995	61.400002	74.900002	6.54902
	7.399998			

Description	Anode H2 Flow	Anode H2 Flow Setpoint	Cathode Air Flow	Cathode Air Flow Setpoint
Unit	nlpm	nlpm	nlpm	nlpm
Time (min:sec:millisec)	GSM_flow_an_MFC_111	GSM_flow_an_MFC_111_set	GSM_flow_ca_MFC_131	GSM_flow_ca_MFC_131_set
44:12.0	0.112687	0.113	0.353438	0.358
45:12.5	0.111813	0.113	0.357188	0.358
46:12.5	0.111062	0.113	0.3575	0.358
47:12.5	0.113	0.113	0.357188	0.358
48:12.5	0.113563	0.113	0.353438	0.358
49:12.5	0.110563	0.113	0.3575	0.358
50:12.5	0.113	0.113	0.360312	0.358
51:12.5	0.112812	0.113	0.358125	0.358
52:12.5	0.113812	0.113	0.364062	0.358
53:12.5	0.113688	0.113	0.360938	0.358
54:12.5	0.112187	0.113	0.36	0.358
55:12.5	0.112812	0.113	0.36125	0.358
56:12.5	0.112938	0.113	0.36	0.358
57:12.5	0.113375	0.113	0.360938	0.358
58:12.5	0.112	0.113	0.36375	0.358
59:12.5	0.112938	0.113	0.36	0.358
00:12.5	0.1135	0.113	0.362188	0.358
01:12.5	0.114125	0.113	0.35	0.358
02:12.5	0.112625	0.113	0.353125	0.358
03:12.5	0.111562	0.113	0.3475	0.358
04:12.5	0.112187	0.113	0.360938	0.358
04:04.5	0.113625	0.113	0.350313	0.358
05:04.5	0.113937	0.113	0.354375	0.358
06:04.5	0.111313	0.113	0.354688	0.358
07:04.5	0.11275	0.113	0.3575	0.358
08:04.5	0.11075	0.113	0.3575	0.358
09:04.5	0.111562	0.113	0.3575	0.358
10:04.5	0.11275	0.113	0.363438	0.358
11:04.5	0.112812	0.113	0.365312	0.358
12:04.5	0.112125	0.113	0.35625	0.358
13:04.5	0.112438	0.113	0.355938	0.358
14:04.5	0.114375	0.113	0.354688	0.358
15:04.5	0.113563	0.113	0.355312	0.358
16:04.5	0.112938	0.113	0.35375	0.358
17:04.5	0.111938	0.113	0.358438	0.358
18:04.5	0.113937	0.113	0.352812	0.358
19:04.5	0.111313	0.113	0.359688	0.358
20:04.5	0.112187	0.113	0.358125	0.358
21:04.5	0.113187	0.113	0.3525	0.358
22:04.5	0.113125	0.113	0.355938	0.358
23:04.5	0.113063	0.113	0.36	0.358
24:04.5	0.112687	0.113	0.3625	0.358
25:04.5	0.112938	0.113	0.360625	0.358
26:04.5	0.112812	0.113	0.361875	0.358
27:04.5	0.11375	0.113	0.359375	0.358
28:04.5	0.113312	0.113	0.351875	0.358
29:04.5	0.112938	0.113	0.362188	0.358
30:04.5	0.113563	0.113	0.355	0.358
31:04.5	0.11325	0.113	0.356562	0.358
32:04.5	0.112375	0.113	0.356562	0.358
33:04.5	0.114188	0.113	0.354375	0.358
34:04.5	0.113563	0.113	0.355625	0.358

Description	Anode Humidifier Output	Cathode Humidifier Output	Anode Dewpoint Setpoint
Unit	%	%	C
Time (min:sec:millisec)	HUMID_heater_an_HTR_383_PWM	HUMID_heater_ca_HTR_381_PWM	HUMID_temp_an_dewpt_PID_TC_389_set
44:12.0	0	1.575142	60
45:12.5	0	0	60
46:12.5	0	0	60
47:12.5	0	1.566194	60
48:12.5	0	2.886181	60
49:12.5	0	3.201134	60
50:12.5	0	4.170862	60
51:12.5	0	6.644296	60
52:12.5	0	0	60
53:12.5	0	0	60
54:12.5	0	0	60
55:12.5	0	0	60
56:12.5	0	0	60
57:12.5	0	0	60
58:12.5	0	11.714725	60
59:12.5	0.153735	11.661908	60
00:12.5	0.340277	11.319539	60
01:12.5	0.680294	49.292919	60
02:12.5	0.267613	45.103859	60
03:12.5	0.600499	36.586533	60
04:12.5	0.629863	27.141718	60
04:04.5	0.652826	18.169634	60
05:04.5	0.363619	33.669136	60
06:04.5	0	26.519962	60
07:04.5	0.310908	19.10293	60
08:04.5	0.329947	12.580008	60
09:04.5	1.156778	7.323665	60
10:04.5	1.122012	3.039074	60
11:04.5	1.399967	0	60
12:04.5	1.671139	0	60
13:04.5	0.678086	0	60
14:04.5	0.863556	0	60
15:04.5	0.722405	0	60
16:04.5	0.723525	0	60
17:04.5	0	0	60
18:04.5	0	0	60
19:04.5	0	0	60
20:04.5	0.985656	0	60
21:04.5	1.256894	0	60
22:04.5	0.75888	0	60
23:04.5	0.150775	0	60
24:04.5	0	38.500172	60
25:04.5	0.636643	39.718239	60
26:04.5	0.831491	35.37944	60
27:04.5	0.755509	29.164948	60
28:04.5	0.300727	22.756289	60
29:04.5	0.463181	17.825842	60
30:04.5	0	13.079751	60
31:04.5	0.637932	8.22081	60
32:04.5	0.243136	4.756312	60

Description	Cathode Dewpoint Setpoint	Cathode Humidifier Temp	Anode Humidifier Temp	Measured load
Unit	C	C	C	Amps
Time (min:sec:millisec)	HUMID_temp_ca_dewpt_PID_TC_386_set	HUMID_temp_TC_386	HUMID_temp_TC_389	load_value
44:12.0	60	64.800003	67.199997	0.112
45:12.5	60	65.099998	67	0.6
46:12.5	60	65	66.800003	0.6
47:12.5	60	64.800003	66.5	0.6
48:12.5	60	64.599998	66.300003	0.6
49:12.5	60	64.699997	66.099998	0.6
50:12.5	60	64.599998	65.800003	0.6
51:12.5	60	64.300003	65.699997	0.6
52:12.5	60	64.099998	65.599998	0.6
53:12.5	60	62.700001	65.5	0.6
54:12.5	60	62.299999	65.300003	0.6
55:12.5	60	60.700001	65.300003	0.6
56:12.5	60	60.400002	65.099998	0.6
57:12.5	60	60	65	0.6
58:12.5	60	58.5	65.099998	0.6
59:12.5	60	58.700001	65	0.6
00:12.5	60	58.900002	64.900002	0.6
01:12.5	60	59.200001	64.900002	0.6
02:12.5	60	60.400002	65	0.6
03:12.5	60	62	64.900002	0.6
04:12.5	60	63.599998	64.900002	0.6
04:04.5	60	64.900002	65	0.6
05:04.5	60	66	65	0.6
06:04.5	60	67.5	65.099998	0.6
07:04.5	60	68.599998	65	0.6
08:04.5	60	69.599998	65	0.6
09:04.5	60	70.300003	64.900002	0.6
10:04.5	60	70.800003	64.900002	0.6
11:04.5	60	71	64.900002	0.6
12:04.5	60	71	64.900002	0.6
13:04.5	60	69.300003	65	0.6
14:04.5	60	69.099998	65	0.6
15:04.5	60	67.400002	65	0.6
16:04.5	60	65.199997	65	0.6
17:04.5	60	65.300003	65	0.6
18:04.5	60	63.599998	65	0.6
19:04.5	60	61.400002	65	0.6
20:04.5	60	61.5	64.800003	0.6
21:04.5	60	61.099998	64.900002	0.6
22:04.5	60	60.799999	64.900002	0.6
23:04.5	60	60.299999	64.800003	0.6
24:04.5	60	60	65.099998	0.6
25:04.5	60	60.5	65	0.6
26:04.5	60	61.5	64.900002	0.6
27:04.5	60	62.599998	64.900002	0.6
28:04.5	60	63.799999	64.900002	0.6
29:04.5	60	64.5	65	0.6
30:04.5	60	65.300003	65	0.6
31:04.5	60	65.699997	64.800003	0.6
32:04.5	60	66.099998	65	0.6
33:04.5	60	66.300003	65	0.6
34:04.5	60	65.599998	64.900002	0.6

Description	Max Cell Voltage	Mean Cell Voltage	Min Cell Voltage	Stack Power	Total Anode Flow	Total Cathode Flow
Unit	V	V	V	W	nlpm	nlpm
Time (min:sec:millisec)	max_cell_voltage	mean_cell_voltage	min_cell_voltage	stack_power	total_anode_stack_flow	total_cathode_stack_flow
44:12.0	0.922819	0.922819	0.922819	0.103114	0.112687	0.353438
45:12.5	0.840175	0.840175	0.840175	0.501114	0.112438	0.354688
46:12.5	0.840358	0.840358	0.840358	0.501114	0.111062	0.353438
47:12.5	0.838954	0.838954	0.838954	0.501114	0.113	0.357188
48:12.5	0.837123	0.837123	0.837123	0.499649	0.113563	0.354688
49:12.5	0.835963	0.835963	0.835963	0.499649	0.110563	0.3575
50:12.5	0.834986	0.834986	0.834986	0.499649	0.113	0.360312
51:12.5	0.83401	0.83401	0.83401	0.498184	0.112812	0.358125
52:12.5	0.833766	0.833766	0.833766	0.498184	0.113812	0.364062
53:12.5	0.833399	0.833399	0.833399	0.498184	0.113688	0.360938
54:12.5	0.834254	0.834254	0.834254	0.498184	0.112187	0.36
55:12.5	0.836634	0.836634	0.836634	0.501114	0.112687	0.36125
56:12.5	0.836573	0.836573	0.836573	0.499649	0.112938	0.36
57:12.5	0.836268	0.836268	0.836268	0.499649	0.112562	0.358438
58:12.5	0.835902	0.835902	0.835902	0.498184	0.113688	0.359375
59:12.5	0.834986	0.834986	0.834986	0.499649	0.112938	0.36
00:12.5	0.834193	0.834193	0.834193	0.498184	0.1135	0.35625
01:12.5	0.833338	0.833338	0.833338	0.498184	0.113312	0.350313
02:12.5	0.832606	0.832606	0.832606	0.496718	0.112625	0.353125
03:12.5	0.831263	0.831263	0.831263	0.496718	0.112938	0.355
04:12.5	0.830164	0.830164	0.830164	0.495253	0.112187	0.360938
04:04.5	0.829371	0.829371	0.829371	0.495253	0.11325	0.350313
05:04.5	0.82754	0.82754	0.82754	0.495253	0.113937	0.354375
06:04.5	0.82461	0.82461	0.82461	0.492323	0.111313	0.354688
07:04.5	0.820215	0.820215	0.820215	0.490858	0.11275	0.3575
08:04.5	0.820704	0.820704	0.820704	0.490858	0.112187	0.360312
09:04.5	0.82107	0.82107	0.82107	0.490858	0.11125	0.3575
10:04.5	0.822047	0.822047	0.822047	0.492323	0.11275	0.363438
11:04.5	0.822047	0.822047	0.822047	0.492323	0.112062	0.361875
12:04.5	0.821375	0.821375	0.821375	0.492323	0.112125	0.35625
13:04.5	0.821436	0.821436	0.821436	0.492323	0.112438	0.355938
14:04.5	0.820826	0.820826	0.820826	0.492323	0.114375	0.354688
15:04.5	0.820765	0.820765	0.820765	0.492323	0.113563	0.355312
16:04.5	0.821131	0.821131	0.821131	0.492323	0.112938	0.35375
17:04.5	0.820338	0.820338	0.820338	0.490858	0.111938	0.358438
18:04.5	0.820276	0.820276	0.820276	0.490858	0.113937	0.352812
19:04.5	0.821619	0.821619	0.821619	0.492323	0.111313	0.359688
20:04.5	0.822962	0.822962	0.822962	0.493788	0.112187	0.358125
21:04.5	0.824793	0.824793	0.824793	0.493788	0.113187	0.3525
22:04.5	0.824915	0.824915	0.824915	0.493788	0.113125	0.355938
23:04.5	0.824976	0.824976	0.824976	0.493788	0.113063	0.36
24:04.5	0.824671	0.824671	0.824671	0.493788	0.112687	0.3625
25:04.5	0.823756	0.823756	0.823756	0.493788	0.112938	0.360625
26:04.5	0.822962	0.822962	0.822962	0.493788	0.112812	0.361875
27:04.5	0.821986	0.821986	0.821986	0.490858	0.11375	0.359375
28:04.5	0.820765	0.820765	0.820765	0.490858	0.113312	0.351875
29:04.5	0.8193	0.8193	0.8193	0.490858	0.112938	0.362188
30:04.5	0.818628	0.818628	0.818628	0.490858	0.112625	0.355
31:04.5	0.817957	0.817957	0.817957	0.489392	0.11325	0.356562
32:04.5	0.816797	0.816797	0.816797	0.489392	0.112062	0.355625
33:04.5	0.815577	0.815577	0.815577	0.489392	0.114188	0.357188
34:04.5	0.814356	0.814356	0.814356	0.486462	0.112375	0.355625

D1.2 Run 2: H_2-Air RH cycling cell

ICY
Model2_Gore57_RH Cycling
Date: 2009-10-01
Time (hr:min:sec) = 10:06:17
Stack Active Area (cm^2) = 42.25

Description	CVM Cell Voltage	Current Density	Anode and Cathode dP	Anode Inlet Pressure	Anode Outlet Pressure
Unit	V	mAmp/cm^2	kPa	kPag	kPag
Time (min:sec:millisec)	data_cell_001V	current_density	FCIM_pressure_an_ca_diff	FCIM_pressure_an_PT_411	FCIM_pressure_an_PT_412
06:17.7	0.881863	14.285714	1.515211	14.394506	0.420892
12:17.7	0.856533	14.285714	1.346854	13.552721	0.841784
18:17.7	0.845424	14.285714	1.094319	12.62676	0.084178
24:17.7	0.835597	14.285714	1.262676	13.468543	0.336714
30:17.7	0.82931	14.285714	1.346854	14.057792	0.841784
36:17.7	0.822779	14.285714	1.094318	14.310327	0.420892
42:17.7	0.822596	14.285714	1.346854	13.721078	0.336714
48:17.7	0.820948	14.285714	2.020281	13.552721	0.420892
54:17.7	0.81814	14.285714	1.262675	13.721078	0.841784
00:17.7	0.816004	14.285714	1.431032	13.721078	0.420892
06:17.7	0.814173	14.285714	1.431032	13.552721	0.336714
12:17.7	0.811914	14.285714	2.020282	14.057792	0.841784
18:17.7	0.810877	14.285714	1.346854	13.721078	0.589249
24:17.7	0.80929	14.285714	1.936103	13.805257	0.841784
30:17.7	0.807764	14.285714	1.262676	13.552721	0.420892
36:17.7	0.807459	14.285714	1.599389	13.468543	0.336714
42:17.7	0.80813	14.285714	0.925962	12.62676	0.336714
47:08.7	0.805506	14.285714	1.094319	13.216008	0.336714
53:08.7	0.805017	14.285714	1.262676	13.468543	0.589249
59:08.7	0.805444	14.285714	1.094318	12.542581	0.084178
05:08.7	0.803064	14.285714	1.767746	13.384364	0.252535
11:08.7	0.801416	14.285714	1.346854	13.721078	0.589249
17:08.7	0.800928	14.285714	1.767746	13.721078	0.841784
23:08.7	0.800256	14.285714	1.851924	13.468543	0.252535
29:08.7	0.799402	14.285714	1.767746	13.721078	0.420892
35:08.7	0.799524	14.285714	1.767746	13.468543	0.420892
41:08.7	0.798547	14.285714	1.599389	13.384364	0.252535
47:08.7	0.797143	14.285714	1.515211	13.805257	0.673427
53:08.7	0.796655	14.285714	1.599389	13.384364	0
59:08.7	0.796106	14.285714	1.599389	13.468543	0.252535
05:08.7	0.796411	14.285714	1.262675	13.468543	0.589249
11:08.7	0.795251	14.285714	1.515211	13.468543	0.336714
17:08.7	0.794397	14.285714	1.515211	13.552721	0.589249
23:08.7	0.793908	14.285714	1.599389	13.721078	0.336714
29:08.7	0.794031	14.285714	1.599389	13.552721	0.420892
35:08.7	0.793176	14.285714	1.683567	13.468543	0.336714
41:08.7	0.792077	14.285714	1.599389	13.552721	0.336714
47:08.7	0.791345	14.285714	1.767746	13.468543	0
53:08.7	0.791406	14.285714	1.767746	13.552721	0.336714
59:08.7	0.792199	14.285714	1.346854	13.384364	0.420892
05:08.7	0.791284	14.285714	1.767746	13.552721	0.589249
11:08.7	0.790613	14.285714	1.515211	13.468543	0.420892
17:08.7	0.790246	14.285714	1.010141	13.468543	0.336714
23:08.7	0.789758	14.285714	1.851924	13.721078	0.841784
29:08.7	0.789026	14.285714	1.767746	13.721078	0.336714

Description	Cathode Inlet Pressure	Cathode Outlet Pressure	Anode and Cathode dT	Anode Inlet Temp
Unit	kPag	kPag	C	C
Time (min:sec:millisec)	FCIM_pressure_ca_PT_431	FCIM_pressure_ca_PT_432	FCIM_temp_an_ca_diff	FCIM_temp_an_TC_412
06:17.7	12.879294	0.841784	1.300003	70.900002
12:17.7	11.53244	0.420892	0.300003	69.5
18:17.7	11.869154	0.925962	0.199997	69.900002
24:17.7	12.121689	0.673427	0.300003	70.199997
30:17.7	11.953332	0.420892	0.199997	70
36:17.7	12.879294	0.589249	0.400002	70
42:17.7	12.121689	0.673427	0.400002	70
48:17.7	11.953332	0.589249	0.099998	70
54:17.7	11.869154	0.420892	0.400002	70
00:17.7	12.121689	0.589249	0	70
06:17.7	11.953332	0.673427	0.099998	70
12:17.7	12.121689	0.420892	0.099998	69.900002
18:17.7	11.953332	0.589249	0.5	70.099998
24:17.7	11.700797	0.420892	0	70.099998
30:17.7	12.121689	0.589249	0.400002	69.900002
36:17.7	11.869154	0.420892	0.400002	69.699997
42:17.7	11.616618	0.673427	0.299995	70
47:08.7	11.700797	0.589249	0.300003	70.099998
53:08.7	11.700797	0.589249	0.300003	70
59:08.7	11.869154	0.841784	0	70
05:08.7	11.869154	0.589249	0.5	70
11:08.7	11.700797	0.336714	0	70
17:08.7	11.700797	0.252535	0.400002	70
23:08.7	11.953332	0.589249	0.5	69.800003
29:08.7	11.869154	0.336714	0.800003	70.099998
35:08.7	11.700797	0.336714	0.099998	70
41:08.7	11.869154	0.589249	0.900002	69.699997
47:08.7	11.869154	0.252535	0	70.099998
53:08.7	12.205867	0.673427	0.800003	70.199997
59:08.7	12.121689	0.420892	0.400002	70
05:08.7	11.700797	0.336714	0	70
11:08.7	11.869154	0.420892	0.099998	70.099998
17:08.7	11.869154	0.420892	0.099998	70
23:08.7	11.953332	0.420892	0.700005	70
29:08.7	11.953332	0.589249	0.300003	70
35:08.7	11.953332	0.589249	1.400002	69.800003
41:08.7	12.121689	0.420892	0.700005	69.800003
47:08.7	12.205867	0.673427	1.600006	70.099998
53:08.7	12.121689	0.589249	1.5	70.199997
59:08.7	11.953332	0.420892	0.599998	70.199997
05:08.7	11.700797	0.420892	1.599998	70
11:08.7	11.953332	0.420892	0.099998	70
17:08.7	11.869154	0.420892	0.900002	70.099998
23:08.7	11.700797	0.420892	0.400002	69.900002
29:08.7	12.121689	0.589249	0.800003	69.800003
35:08.7	11.953332	0.420892	0.599998	70.099998
41:08.7	12.290046	0.925962	0.300003	70.099998
47:08.7	12.290046	0.925962	0.799995	70
53:08.7	12.205867	0.589249	0.099998	70.099998
59:08.7	12.121689	0.673427	0.800003	69.900002
05:08.7	12.121689	0.673427	0.200005	69.800003

Description	Cathode and Coolant dT	Cathode Inlet Temp	Cathode Outlet Temp	H2 Detector LEVEL	Anode H2 Flow
Unit	C	C	C	%	nlpm
Time (min:sec:millisec)	FCIM_temp_ca_cool_diff	FCIM_temp_ca_TC_432	FCIM_temp_ca_TC_433	FM_input_HD_1_LVL	GSM_flow_an_MFC_111
06:17.7	3207.099854	69.599998	73.599998	4.980392	0.111625
12:17.7	3206.899902	69.800003	73.099998	5.45098	0.113375
18:17.7	3206.699951	70.099998	73.099998	4.823529	0.1115
24:17.7	3206.199951	70.5	73	4.823529	0.112687
30:17.7	3206.5	70.099998	73.199997	6.392157	0.112187
36:17.7	3207.099854	69.599998	73.099998	6.235294	0.113375
42:17.7	3207.099854	69.599998	73.099998	6.392157	0.112187
48:17.7	3206.599854	70.099998	73.199997	6.235294	0.112812
54:17.7	3206.300049	70.400002	73.099998	4.666667	0.114063
00:17.7	3206.699951	70	73.099998	4.823529	0.112
06:17.7	3206.899902	69.800003	73.300003	4.980392	0.114375
12:17.7	3206.800049	69.800003	73.199997	4.666667	0.113063
18:17.7	3206.199951	70.5	73.300003	4.980392	0.11175
24:17.7	3206.599854	70.099998	73.300003	5.45098	0.113
30:17.7	3207.300049	69.5	73.099998	4.980392	0.112375
36:17.7	3207.300049	69.5	73.400002	4.666667	0.112625
42:17.7	3206.5	70.099998	73.300003	5.294117	0.112625
47:08.7	3206.300049	70.300003	73.099998	4.980392	0.112187
53:08.7	3206.399902	70.300003	73	4.823529	0.113312
59:08.7	3206.699951	69.900002	73.400002	4.980392	0.112187
05:08.7	3207.199951	69.5	73.300003	4.980392	0.112375
11:08.7	3206.699951	70	73	4.980392	0.113688
17:08.7	3207.099854	69.599998	73	4.823529	0.113
23:08.7	3207.399902	69.300003	73.099998	4.980392	0.113937
29:08.7	3205.899902	70.800003	73	4.823529	0.111562
35:08.7	3206.800049	69.900002	73.199997	4.666667	0.113063
41:08.7	3207.800049	69	72.800003	4.823529	0.1125
47:08.7	3206.699951	70	73	5.45098	0.11225
53:08.7	3205.699951	71	72.800003	5.45098	0.112687
59:08.7	3206.300049	70.400002	73.099998	4.823529	0.113187
05:08.7	3206.699951	70.099998	72.800003	4.823529	0.112875
11:08.7	3206.699951	70	73.099998	5.45098	0.112125
17:08.7	3206.599854	70.199997	72.800003	4.980392	0.113
23:08.7	3205.899902	70.699997	72.599998	4.666667	0.113688
29:08.7	3207	69.599998	73	6.54902	0.112125
35:08.7	3208.300049	68.400002	72.900002	4.980392	0.11375
41:08.7	3207.599854	69.300003	73	4.823529	0.113812
47:08.7	3204.899902	71.800003	73.099998	5.45098	0.1125
53:08.7	3205.099854	71.599998	73.300003	4.823529	0.11325
59:08.7	3207.199951	69.5	73.099998	4.980392	0.114375
05:08.7	3208.199951	68.599998	73.099998	4.823529	0.112375
11:08.7	3206.599854	70.199997	73.099998	4.980392	0.112375
17:08.7	3205.599854	71	73	5.294117	0.112875
23:08.7	3206.399902	70.300003	73	5.45098	0.111625
29:08.7	3207.699951	69	73	5.294117	0.113063
35:08.7	3207.099854	69.599998	72.900002	4.823529	0.113375
41:08.7	3206.300049	70.400002	73	4.823529	0.112062
47:08.7	3206	70.800003	73.099998	4.823529	0.112938
53:08.7	3206.5	70.099998	73.099998	5.294117	0.114312
59:08.7	3207.599854	69.199997	72.800003	4.823529	0.112875
05:08.7	3207.099854	69.599998	73.199997	4.823529	0.114063
11:08.7	3206	70.300003	72.800003	4.823529	0.11275

Description	Anode H2 Flow Setpoint	Cathode Air Flow	Cathode Air Flow Setpoint	Anode Humidifier Output
Unit	nlpm	nlpm	nlpm	%
Time (min:sec:millisec)	GSM_flow_an_MFC_111_set	GSM_flow_ca_MFC_131	GSM_flow_ca_MFC_131_set	HUMID_heater_an_HTR_383_PWM
06:17.7	0.113	0.360938	0.358	7.224266
12:17.7	0.113	0.357188	0.358	6.429693
18:17.7	0.113	0.3575	0.358	5.532636
24:17.7	0.113	0.356875	0.358	4.959909
30:17.7	0.113	0.35625	0.358	5.23656
36:17.7	0.113	0.36	0.358	5.556272
42:17.7	0.113	0.360312	0.358	5.700568
48:17.7	0.113	0.357812	0.358	5.246519
54:17.7	0.113	0.358438	0.358	5.715884
00:17.7	0.113	0.359375	0.358	5.186265
06:17.7	0.113	0.360938	0.358	5.582366
12:17.7	0.113	0.355	0.358	5.909527
18:17.7	0.113	0.356562	0.358	5.708715
24:17.7	0.113	0.355938	0.358	6.1189
30:17.7	0.113	0.359062	0.358	7.043425
36:17.7	0.113	0.358125	0.358	7.369834
42:17.7	0.113	0.357812	0.358	7.464977
47:08.7	0.113	0.3575	0.358	8.034709
53:08.7	0.113	0.357188	0.358	8.088167
59:08.7	0.113	0.355938	0.358	8.321435
05:08.7	0.113	0.35125	0.358	8.212605
11:08.7	0.113	0.355625	0.358	8.234678
17:08.7	0.113	0.35625	0.358	8.213878
23:08.7	0.113	0.362812	0.358	9.071584
29:08.7	0.113	0.36	0.358	8.065564
35:08.7	0.113	0.360625	0.358	8.168468
41:08.7	0.113	0.354688	0.358	8.585163
47:08.7	0.113	0.355312	0.358	8.206635
53:08.7	0.113	0.359688	0.358	9.001043
59:08.7	0.113	0.36125	0.358	8.655363
05:08.7	0.113	0.36	0.358	8.649208
11:08.7	0.113	0.356875	0.358	8.022973
17:08.7	0.113	0.355938	0.358	7.997129
23:08.7	0.113	0.362188	0.358	7.23056
29:08.7	0.113	0.357812	0.358	7.546569
35:08.7	0.113	0.357188	0.358	8.28778
41:08.7	0.113	0.356875	0.358	9.252231
47:08.7	0.113	0.355938	0.358	7.860073
53:08.7	0.113	0.358125	0.358	7.982264
59:08.7	0.113	0.357812	0.358	7.743885
05:08.7	0.113	0.359062	0.358	7.615832
11:08.7	0.113	0.355312	0.358	7.434714
17:08.7	0.113	0.358438	0.358	7.424921
23:08.7	0.113	0.354688	0.358	7.168122
29:08.7	0.113	0.361875	0.358	6.702739
35:08.7	0.113	0.356562	0.358	6.649887
41:08.7	0.113	0.356562	0.358	6.345883
47:08.7	0.113	0.363125	0.358	6.292029
53:08.7	0.113	0.35875	0.358	6.39527
59:08.7	0.113	0.35625	0.358	6.784332
05:08.7	0.113	0.355625	0.358	6.479793
11:08.7	0.113	0.359688	0.358	6.744669

Description	Anode Humidifier Output	Cathode Humidifier Output	Anode Dewpoint Setpoint
Unit	%	%	C
Time (min:sec:millisec)	HUMID_heater_an_HTR_383_PWM	HUMID_heater_ca_HTR_381_PWM	HUMID_temp_an_dewpt_PID_TC_389_set
06:17.7	7.224266	10.547278	65
12:17.7	6.429693	8.195402	65
18:17.7	5.532636	8.129406	65
24:17.7	4.959909	7.112143	65
30:17.7	5.23656	7.312059	65
36:17.7	5.556272	7.08747	65
42:17.7	5.700568	6.910105	65
48:17.7	5.246519	6.405616	65
54:17.7	5.715884	7.006876	65
00:17.7	5.186265	7.084201	65
06:17.7	5.582366	7.183307	65
12:17.7	5.909527	6.711192	65
18:17.7	5.708715	7.227473	65
24:17.7	6.1189	8.7718	65
30:17.7	7.043425	8.330054	65
36:17.7	7.369834	8.391457	65
42:17.7	7.464977	8.906091	65
47:08.7	8.034709	8.773431	65
53:08.7	8.088167	9.062869	65
59:08.7	8.321435	9.271286	65
05:08.7	8.212605	8.737351	65
11:08.7	8.234678	8.58047	65
17:08.7	8.213878	8.146273	65
23:08.7	9.071584	9.139694	65
29:08.7	8.065564	8.474929	65
35:08.7	8.168468	9.278754	65
41:08.7	8.585163	8.71316	65
47:08.7	8.206635	8.146578	65
53:08.7	9.001043	9.753567	65
59:08.7	8.655363	10.157131	65
05:08.7	8.649208	9.203121	65
11:08.7	8.022973	8.859548	65
17:08.7	7.997129	9.237816	65
23:08.7	7.23056	8.77861	65
29:08.7	7.546569	9.13554	65
35:08.7	8.28778	9.342919	65
41:08.7	9.252231	8.940523	65
47:08.7	7.860073	8.4448	65
53:08.7	7.982264	9.828997	65
59:08.7	7.743885	9.659847	65
05:08.7	7.615832	8.530802	65
11:08.7	7.434714	7.740428	65
17:08.7	7.424921	7.864705	65
23:08.7	7.168122	9.383848	65
29:08.7	6.702739	8.180241	65
35:08.7	6.649887	8.050132	65
41:08.7	6.345883	7.371598	65
47:08.7	6.292029	8.685455	65
53:08.7	6.39527	9.234261	65
59:08.7	6.784332	8.259211	65

Description	Cathode Humidifier Temp	Anode Humidifier Temp	Measured load	Load Output Setpoint	Max Cell Voltage
Unit	C	C	Amps	Amps	V
Time (min:sec:millisec)	HUMID_temp_TC_386	HUMID_temp_TC_389	load_value	load_value_set	max_cell_voltage
06:17.7	63.599998	64.699997	0.6	0.5	0.882046
12:17.7	64.599998	64.900002	0.6	0.5	0.856533
18:17.7	64.900002	65.099998	0.6	0.5	0.845485
24:17.7	64.900002	65	0.6	0.5	0.835597
30:17.7	65.099998	65	0.6	0.5	0.82931
36:17.7	64.900002	65	0.6	0.5	0.822779
42:17.7	65	65	0.6	0.5	0.822596
48:17.7	65.099998	65	0.6	0.5	0.820948
54:17.7	65	65	0.6	0.5	0.81814
00:17.7	65	65	0.6	0.5	0.816004
06:17.7	65	65	0.6	0.5	0.814173
12:17.7	65.099998	65	0.6	0.5	0.811914
18:17.7	65	64.900002	0.6	0.5	0.810877
24:17.7	64.800003	64.900002	0.6	0.5	0.80929
30:17.7	65	64.800003	0.6	0.5	0.807764
36:17.7	65.099998	64.800003	0.6	0.5	0.807459
42:17.7	65	65	0.6	0.5	0.80813
47:08.7	65	64.900002	0.6	0.5	0.805506
53:08.7	64.900002	65	0.6	0.5	0.805017
59:08.7	65	65	0.6	0.5	0.805444
05:08.7	65	65	0.6	0.5	0.803064
11:08.7	65.099998	65	0.6	0.5	0.801416
17:08.7	65	65	0.6	0.5	0.800928
23:08.7	65	64.900002	0.6	0.5	0.800256
29:08.7	65	65	0.6	0.5	0.799341
35:08.7	65	65	0.6	0.5	0.799524
41:08.7	65.099998	65	0.6	0.5	0.798547
47:08.7	65.099998	65.099998	0.6	0.5	0.797143
53:08.7	64.800003	65	0.6	0.5	0.796655
59:08.7	64.900002	64.900002	0.6	0.5	0.796106
05:08.7	65	65	0.6	0.5	0.796411
11:08.7	65	65	0.6	0.5	0.795251
17:08.7	65	64.900002	0.6	0.5	0.794336
23:08.7	65	65.099998	0.6	0.5	0.793908
29:08.7	65	65	0.6	0.5	0.794031
35:08.7	65	64.900002	0.6	0.5	0.793176
41:08.7	65	64.900002	0.6	0.5	0.792077
47:08.7	65	65.099998	0.6	0.5	0.791345
53:08.7	65	65.099998	0.6	0.5	0.791406
59:08.7	65	65	0.6	0.5	0.792199
05:08.7	65.199997	65	0.6	0.5	0.791284
11:08.7	65.199997	65	0.6	0.5	0.790613
17:08.7	65	65	0.6	0.5	0.790307
23:08.7	64.800003	65.099998	0.6	0.5	0.789758
29:08.7	64.800003	65	0.6	0.5	0.789026
35:08.7	65.099998	65.099998	0.6	0.5	0.788049
41:08.7	65	65	0.6	0.5	0.787927
47:08.7	64.900002	65	0.6	0.5	0.787744
53:08.7	64.900002	64.900002	0.6	0.5	0.788842
59:08.7	65	65.099998	0.6	0.5	0.787744
05:08.7	65	65	0.6	0.5	0.787011

Description	Mean Cell Voltage	Min Cell Voltage	Stack Power	Total Anode Flow	Total Cathode Flow
Unit	V	V	W	nlpm	nlpm
Time (min:sec:millisec)	mean_cell_voltage	min_cell_voltage	stack_power	total_anode_stack_flow	total_cathode_stack_flow
06:17.7	0.882046	0.882046	0.530419	0.111625	0.360938
12:17.7	0.856533	0.856533	0.512836	0.113312	0.357188
18:17.7	0.845485	0.845485	0.50551	0.1115	0.35875
24:17.7	0.835597	0.835597	0.498184	0.112687	0.356875
30:17.7	0.82931	0.82931	0.496718	0.113375	0.35625
36:17.7	0.822779	0.822779	0.492323	0.113	0.36
42:17.7	0.822596	0.822596	0.492323	0.112187	0.360312
48:17.7	0.820948	0.820948	0.490858	0.112812	0.357812
54:17.7	0.81814	0.81814	0.489392	0.112625	0.358438
00:17.7	0.816004	0.816004	0.489392	0.112	0.359375
06:17.7	0.814173	0.814173	0.486462	0.114375	0.359688
12:17.7	0.811914	0.811914	0.484997	0.113063	0.355
18:17.7	0.810877	0.810877	0.483531	0.11175	0.356562
24:17.7	0.80929	0.80929	0.483531	0.113	0.355938
30:17.7	0.807764	0.807764	0.483531	0.11375	0.360312
36:17.7	0.807459	0.807459	0.483531	0.112625	0.358125
42:17.7	0.80813	0.80813	0.483531	0.112625	0.357812
47:08.7	0.805506	0.805506	0.482066	0.112187	0.3575
53:08.7	0.805017	0.805017	0.482066	0.113312	0.357188
59:08.7	0.805444	0.805444	0.482066	0.112187	0.355938
05:08.7	0.803064	0.803064	0.480601	0.112375	0.35125
11:08.7	0.801416	0.801416	0.480601	0.113688	0.355625
17:08.7	0.800928	0.800928	0.479136	0.113	0.35625
23:08.7	0.800256	0.800256	0.479136	0.113937	0.362812
29:08.7	0.799341	0.799341	0.479136	0.111562	0.36
35:08.7	0.799524	0.799524	0.479136	0.113063	0.360625
41:08.7	0.798547	0.798547	0.479136	0.1125	0.354688
47:08.7	0.797143	0.797143	0.476205	0.11275	0.355312
53:08.7	0.796655	0.796655	0.476205	0.112687	0.359688
59:08.7	0.796106	0.796106	0.47474	0.113187	0.36125
05:08.7	0.796411	0.796411	0.476205	0.112875	0.355
11:08.7	0.795251	0.795251	0.47474	0.112125	0.356875
17:08.7	0.794336	0.794336	0.47474	0.113	0.355938
23:08.7	0.793908	0.793908	0.473275	0.113688	0.362188
29:08.7	0.794031	0.794031	0.47474	0.112125	0.357812
35:08.7	0.793176	0.793176	0.47474	0.11375	0.357188
41:08.7	0.792077	0.792077	0.473275	0.113812	0.360312
47:08.7	0.791345	0.791345	0.473275	0.1125	0.356562
53:08.7	0.791406	0.791406	0.473275	0.11325	0.358125
59:08.7	0.792199	0.792199	0.473275	0.114375	0.357812
05:08.7	0.791284	0.791284	0.473275	0.112375	0.359062
11:08.7	0.790613	0.790613	0.473275	0.112375	0.355312
17:08.7	0.790307	0.790307	0.473275	0.11225	0.358438
23:08.7	0.789758	0.789758	0.471809	0.111625	0.354688
29:08.7	0.789026	0.789026	0.471809	0.113688	0.360938
35:08.7	0.788049	0.788049	0.471809	0.113375	0.356562
41:08.7	0.787927	0.787927	0.470344	0.11325	0.356562
47:08.7	0.787744	0.787744	0.471809	0.112938	0.363125
53:08.7	0.788842	0.788842	0.471809	0.114312	0.35875
59:08.7	0.787744	0.787744	0.471809	0.112875	0.35625
05:08.7	0.787011	0.787011	0.471809	0.114063	0.355625

D2. Voltage degradation rate

The voltage degradation rates at a constant current density of 10 mA cm^{-2} are separated into three regions; commissioning region, steady state region, and highly decayed region. The degradation rates of the steady state, highly decayed regions as well as the overall voltage degradation rate can be calculated as follows:

D2.1 List of terms

Variable	Description	Units
t_i	Start time of degradation	h
t_j	End time of degradation	h
V_{t_i}	Voltage at start time of degradation	V
V_{t_j}	Voltage at end time of degradation	V

D2.2 Run 1: 100% RH humidified cell

Sample data of cell voltages

Time (Hrs)	Voltage (V)
1	0.849147
26	0.821314
50	0.811426
97	0.83
117	0.878079
130	0.832118
165	0.872829
190	0.869594
212	0.866359
245	0.862636
264	0.864345
286	0.866878
316	0.869411
334	0.854762
357	0.851161
376	0.845607
395	0.842372
419	0.851711

Time (Hrs)	Voltage (V)
440	0.841395
463	0.839015
491	0.854091
509	0.839259
534	0.824427
561	0.821009
581	0.801477
606	0.8193
634	0.806421
650	0.838893
679	0.783532
721	0.743614
744	0.735496
766	0.717124
793	0.708457
819	0.69863
838	0.697287

D2.2.1 Steady state region

$$\text{Voltage degradation rate} = \frac{V_{t_i} - V_{t_j}}{t_j - t_i}$$

$$= \frac{V_{t_{117}} - V_{t_{634}}}{t_{634} - t_{117}}$$

$$= \frac{0.8781 - 0.8064}{634 - 117}$$

$$= 0.000139 \text{ V h}^{-1} = 0.139 \text{ mV h}^{-1}$$

D2.2.2 Highly decayed region

$$\text{Voltage degradation rate} = \frac{V_{t_i} - V_{t_j}}{t_j - t_i}$$

$$= \frac{V_{t_{634}} - V_{t_{838}}}{t_{838} - t_{634}}$$

$$= \frac{0.8064 - 0.6973}{838 - 634}$$

$$= 0.000535 \text{ V h}^{-1} = 0.535 \text{ mV h}^{-1}$$

D2.2.3 Overall cell voltage degradation rate

$$\text{Voltage degradation rate} = \frac{V_{t_i} - V_{t_j}}{t_j - t_i}$$

$$= \frac{V_{t_1} - V_{t_{838}}}{t_{838} - t_1}$$

$$= \frac{0.8491 - 0.6973}{838 - 1}$$

$$= 0.00018 \text{ V h}^{-1} = 0.18 \text{ mV h}^{-1}$$

D2.3 Run 2: RH cycling cell

Sample data of cell voltages

Time (hrs)	Voltage (V)
1	0.840602
25	0.806604
49	0.822596
73	0.818812
93	0.825282
117	0.802087
138	0.836818
167	0.839869
189	0.835841
258	0.823145
284	0.82345
308	0.826502
331	0.823634

Time (hrs)	Voltage (V)
368	0.820704
386	0.821925
410	0.821131
430	0.818628
454	0.805933
460	0.813013
480	0.808008
507	0.763695
534	0.7828
585	0.722434
633	0.680319
658	0.693381

D2.3.1 Steady state region

$$\text{Voltage degradation rate} = \frac{V_{t_i} - V_{t_j}}{t_j - t_i}$$

$$= \frac{V_{t_{138}} - V_{t_{460}}}{t_{460} - t_{138}}$$

$$= \frac{0.8368 - 0.8130}{460 - 138}$$

$$= 0.000074 \text{ V h}^{-1} = 0.074 \text{ mV h}^{-1}$$

D2.3.2 Highly decayed region

$$\text{Voltage degradation rate} = \frac{V_{t_i} - V_{t_j}}{t_j - t_i}$$

$$= \frac{V_{t_{460}} - V_{t_{658}}}{t_{658} - t_{460}}$$

$$= \frac{0.8130 - 0.6934}{658 - 460}$$

$$= 0.0006 \text{ V h}^{-1} = 0.6 \text{ mV h}^{-1}$$

D2.3.3 Overall cell voltage degradation rate

$$\text{Voltage degradation rate} = \frac{V_{t_i} - V_{t_j}}{t_j - t_i}$$

$$= \frac{V_{t_1} - V_{t_{658}}}{t_{658} - t_1}$$

$$= \frac{0.8406 - 0.6934}{658 - 1}$$

$$= 0.00024 \text{ V h}^{-1} = 0.24 \text{ mV h}^{-1}$$

D3. Fluoride release

In this section, the calculations of fluoride release rates and cumulative fluoride release from the effluent water of both anode and cathode are shown.

D3.1 List of terms

Variable	Description	Units
n_{F_A}	Moles of fluoride in water sample on anode side	Mol
n_{F_C}	Moles of fluoride in water sample on cathode side	mol
$\dot{n}_{F_A}$	Fluoride release rate on anode side	mol h^{-1}
$\dot{n}_{F_C}$	Fluoride release rate on cathode side	mol h^{-1}
C_{F_A}	Fluoride ion concentration for water sample on anode side	mg L^{-1}
C_{F_C}	Fluoride ion concentration for water sample on cathode side	mg L^{-1}
V_{W_A}	Collected water volume for water sample on anode side	mL
V_{W_C}	Collected water volume for water sample on cathode side	mL
t_W	Water collection time	h
t_S	Segment time	h
$n_{Cum\,F_A}$	Cumulative fluoride released from t = 0 to the end of water collection segment "i" on anode side	mol cm^{-2}
$n_{Cum\,F_C}$	Cumulative fluoride released from t = 0 to the end of water collection segment "i" on cathode side	mol cm^{-2}

D3.2 Data of Run 1: 100% RH humidified cell

Sample Name	Amount of F^- (mg/L)	Volume of water (mL)	Time spent (hrs)
Anode_Jun 22	3.116	110.0	91
Cathode_Jun 22	1.758	365.0	91
Anode_Jun 26	5.000	135.0	186
Cathode_Jun 26	7.000	380.0	186
Anode_Jun 30	2.000	120.0	273
Cathode_Jun 30	1.000	370.0	273
Anode_Jul 3	4.087	125.0	343
Cathode_Jul 3	3.776	395.0	343
Anode_Jul 7	5.348	61.5	420
Cathode_Jul 7	5.152	330.0	420
Anode_Jul 10	4.644	96.5	487
Cathode_Jul 10	5.076	360.0	487
Anode_Jul 13	7.840	68.5	558
Cathode_Jul 13	7.373	347.0	558
Anode_Jul 17	3.956	59.5	651
Cathode_Jul 17	4.625	300.0	651
Anode_Sep17	1.541	75	697
Cathode_Sep17	1.634	272	697
Anode_Sep21	0.921	155	790
Cathode_Sep21	0.934	551	790

D3.3 Data of Run 2: RH cycling cell

Sample Name	Amount of F- (mg/L)	Volume of water (mL)	Time spent (hrs)
Anode_Oct2	5.53	113	72
Cathode_Oct2	3.714	414	72
Anode_Oct7	5.175	37	96
Cathode_Oct7	4.649	127	96
Anode_Oct15	4.696	84	135
Cathode_Oct15	2.593	243	135
Anode_Oct17	3.401	71	181
Cathode_Oct17	1.486	77	181
Anode_Oct19	2.338	63	227
Cathode_Oct19	1.119	42	227
Anode_Oct20	2.574	38	248
Cathode_Oct20	1.72	23	248
Anode_Oct21	2.937	27	272

Cathode_Oct21	1.334	19	272
Anode_Oct22	2.654	34	300
Cathode_Oct22	1.096	24	300
Anode_Oct23	2.331	28	318
Cathode_Oct23	1.269	76	318
Anode_Oct24	2.313	35	348
Cathode_Oct24	1.501	65	348
Anode_Oct25	3.075	27	363
Cathode_Oct25	1.192	42	363
Anode_Oct26	1.977	35	385
Cathode_Oct26	1.085	59	385
Anode_Oct27	2.769	26	408
Cathode_Oct27	0.703	48	408
Anode_Oct28	2.899	17	428
Cathode_Oct28	0.997	52	428
Anode_Oct29	2.326	18	455
Cathode_Oct29	0.803	60	455
Anode_Oct30	4.49	18	477
Cathode_Oct30	5.263	66	477
Anode_Nov5	4.369	21	502
Cathode_Nov5	1.177	56	502
Anode_Nov6	3.113	31	530
Cathode_Nov6	1.587	85	530
Anode_Nov11	2.272	60	573
Cathode_Nov11	0.964	146	573
Anode_Nov12	1.833	89	596
Cathode_Nov12	0.957	175	596
Anode_Nov13	1.988	39	622
Cathode_Nov13	0.604	127	622

Sample of data set used for fluoride release rate and cumulative fluoride release calculations (from Run 1):

Segment "i"	Operating time (hrs)	Segment time (hrs)	Water collection time (hrs)	Anode fluoride concentration (mg L^{-1})	Cathode fluoride concentration (mg L^{-1})
1	91			3.116	1.758
2	186	95	70	5	7

D3.4 Fluoride release rate

D3.4.1 Anode fluoride release rate

- Amount of fluoride (n_{F_A})

$$n_{F_A} = C_{F_A} V_W$$

$$= \left[\left(3.116 \frac{mg}{L}\right) \frac{1g}{1000mg} \frac{1mol}{19\ g\ F-}\right] \left[(110\ mL) \frac{1L}{1000\ mL}\right]$$

$$= 1.8 \text{ x } 10^{-5} \text{ mol}$$

- Fluoride release rate ($\dot{n}_{F_A}$)

$$\dot{n}_{F_A} = \frac{n_{F_A}}{t_W} = \frac{1.8 \text{ x } 10^{-5} \text{mol}}{70\ hrs} = 2.58 \text{ x } 10^{-7} \frac{mol}{hr}$$

D3.4.2 Cathode fluoride release rate

- Amount of fluoride (n_{F_C})

$$n_{F_C} = C_{F_C} V_W$$

$$= \left[\left(1.758 \frac{mg}{L}\right) \frac{1g}{1000mg} \frac{1mol}{19\ g\ F-}\right] \left[(365\ mL) \frac{1L}{1000\ mL}\right]$$

$$= 3.38 \text{ x } 10^{-5} \text{ mol}$$

- Fluoride release rate ($\dot{n}_{F_C}$)

$$\dot{n}_{F_C} = \frac{n_{F_C}}{t_W} = \frac{3.38 \text{ x } 10^{-5} \text{mol}}{70\ hrs} = 4.82 \text{ x } 10^{-7} \frac{mol}{hr}$$

D3.5 Cumulative fluoride release rate

The cumulative fluoride release rate is calculated based on an assumption that the fluoride release rate is constant for a segment of time. This assumption is valid since all the effluent water has been collected and used for the calculation.

D3.5.1 Anode cumulative fluoride release rate

For the 1st segment time:

During the first segment (t_s) and base on the cell active area of 42.25 cm^2, the fluoride release rate per cell active area is

$$= \left[\frac{\left(2.58 \text{ x } 10^{-7} \frac{mol}{hr}\right)}{42.25\ cm^2} \frac{10^6 \mu mol}{1\ mol}\right] (95\ hrs)$$

$$= 0.5795\ \frac{\mu mol}{cm^2}$$

For the 2nd segment time: $n_{Cum\ F_A} = \sum_{i=2} n_{F_A}$

$$= 0.5795\ \frac{\mu mol}{cm^2} + 1.1411\ \frac{\mu mol}{cm^2}$$

$$= 1.6936\ \frac{\mu mol}{cm^2}$$

D3.5.2 Cathode cumulative fluoride release rate

For the 1st segment time:

During the first segment (t_s) and base on a cell active area of 42.25 cm^2, the fluoride release rate per cell active area is

$$= \left[\frac{\left(4.82 \text{ x } 10^{-7} \frac{mol}{hr}\right)}{42.25\ cm^2} \frac{10^6 \mu mol}{1\ mol}\right] (95\ hrs)$$

$$= 1.0848\ \frac{\mu mol}{cm^2}$$

For the 2nd segment time: $n_{Cum\ F_C} = \sum_{i=2} n_{F_C}$

$$= 1.0848\ \frac{\mu mol}{cm^2} + 4.4970\ \frac{\mu mol}{cm^2}$$

$$= 5.5827\ \frac{\mu mol}{cm^2}$$

D4. Water balance

D4.1. List of terms

Variable	Description	Units
$Q_{H_2,in}$	Volumetric flow rate of H_2 inlet	SLPM
$Q_{Air,in}$	Volumetric flow rate of Air inlet	SLPM
$T_{H_2,in}$	Temperature of H_2 inlet	°C
$T_{Air,in}$	Temperature of Air inlet	°C
$T_{H_2,ko}$	Temperature of H_2 exiting knockout drum	°C
$T_{Air,ko}$	Temperature of Air exiting knockout drum	°C
$RH_{H_2,in}$	Relative humidity of H_2 inlet	%
$RH_{Air,in}$	Relative humidity of Air inlet	%
$RH_{H_2,ko}$	Relative humidity of H_2 exiting knockout drum	%
$RH_{Air,ko}$	Relative humidity of Air exiting knockout drum	%
$n_{H_2,in}$	Molar flow rate of H_2 inlet	mol min^{-1}
$n_{Air,in}$	Molar flow rate of Air inlet	mol min^{-1}
n_{H_2O,H_2}	Molar flow rate of water into the cell by H_2 inlet	mol min^{-1}
$n_{H_2O,Air}$	Molar flow rate of water into the cell by Air inlet	mol min^{-1}
$n_{H_2O,H_2(ko)}$	Molar flow rate of water exiting knockout drum by H_2	mol min^{-1}
$n_{H_2O,Air(ko)}$	Molar flow rate of water exiting knockout drum by Air	mol min^{-1}
$n_{H_2O,rxn}$	Molar flow rate of water produced through the reaction	mol min^{-1}
$m_{H_2O,H_2(in)}$	Mass flow rate of water in H_2 inlet	g h^{-1}

$m_{H_2O,Air\ (in)}$	Mass flow rate of water in Air inlet	g h^{-1}
$m_{H_2O,H_2(ko)}$	Mass flow rate of water exiting H_2 knockout drum	g h^{-1}
$m_{H_2O,Air\ (ko)}$	Mass flow rate of water exiting Air knockout drum	g h^{-1}
$m_{H_2O,rxn}$	Mass flow rate of water produced through the reaction	g h^{-1}
$m_{H_2O,H_2(con)}$	Mass flow rate of water collected in H_2 knockout drum	g h^{-1}
$m_{H_2O,Air\ (con)}$	Mass flow rate of water collected in Air knockout drum	g h^{-1}
y_{H_2O,H_2}	Mole fraction of water in H_2 inlet	-
$y_{H_2O,Air}$	Mole fraction of water in Air inlet	-
$y_{H_2O,H_2(ko)}$	Mole fraction of water exiting H_2 knockout drum	-
$y_{H_2O,Air\ (ko)}$	Mole fraction of water exiting Air knockout drum	-
p_{H_2O}	Partial pressure of water	mmHg
$P^{v}{}_{H_2O,in}(T)$	Vapor pressure of water inlet at temperature "T"	mmHg
$P^{v}{}_{H_2O,ko}(T)$	Vapor pressure of water exiting knockout drum at temperature "T"	mmHg
P_{tot}	Total pressure	mmHg
i	Current density	mA cm^{-2}
A_{geo}	Fuel cell geometric active area	cm^2

D4.2 Water Balance Calculations

In this section, the water balance inside the fuel cell will be calculated. Note that the sample data sets used for the calculations are from Run 1:

D4.2.1 Mass flow of water into the fuel cell

By performing material balances on the inlet streams, the amount of water entering the fuel cell system with humidified anode and cathode is presented.

Set of data is given:

Variable	Value
$Q_{H_2,in}$	0.113 SLPM
$Q_{Air,in}$	0.358 SLPM
$T_{H_2,in}$	70°C
$T_{Air,in}$	70°C
RH_{H_2}	100%
RH_{Air}	100%

- Molar flow rate of H_2 inlet and air inlet

$$n_{H_2,in} = \frac{Q_{H_2,in}}{22.4 L mol^{-1}}$$

$$n_{H_2,in} = \frac{0.113\ L\ \min^{-1}}{22.4 L mol^{-1}} = 0.0050\ \frac{mol}{\min}$$

$$n_{Air,in} = \frac{Q_{Air,in}}{22.4 L mol^{-1}}$$

$$n_{Air,in} = \frac{0.358\ L\ \min^{-1}}{22.4 L mol^{-1}} = 0.0159\ \frac{mol}{\min}$$

- Mole fraction of water in H_2 inlet and air inlet streams

$$y_{H_2O,in} = \frac{p_{H_2O}}{P_{tot}} = \frac{RH_i}{100\ \%} \frac{P^v{}_{H_2O,in}(T)}{P_{tot}}$$

$$y_{H_2O,H_2} = y_{H_2O,Air} = \frac{100\ \%}{100\ \%} \frac{P^v{}_{H_2O,in}(70\ ^\circ C)}{760}$$

- From Antoine's equation: $P^v{}_{H_2O,in}(70\ ^\circ C)$ is obtained

$$\log_{10}(P^v{}_{H_2O,in}(70\ ^\circ C)) = 8.0713 - \frac{1730.63}{70 + 233.426} = 2.3677$$

$$p^v{}_{H_2O,in}(70\ ^\circ C) = 233.168\ mmHg$$

Thus,

$$y_{H_2O,H_2} = y_{H_2O,Air} = \frac{100\ \%}{100\ \%} \frac{233.168\ mmHg}{760\ mmHg} = 0.3068$$

- Molar flow rate of water into the cell with H_2 and air streams

$$n_{H_2O,H_2} = \frac{y_{H_2O,H_2}}{(1 - y_{H_2O,H_2})} n_{H_2,in} = \frac{0.3068}{(1 - 0.3068)} 0.0050\ \frac{mol}{\min} = 0.0022\ \frac{mol}{\min}$$

$$n_{H_2O,Air} = \frac{y_{H_2O,Air}}{(1 - y_{H_2O,Air})} n_{Air,in} = \frac{0.3068}{(1 - 0.3068)} 0.0159\ \frac{mol}{\min} = 0.0070\ \frac{mol}{\min}$$

Converting molar flow to mass flow gives

$$m_{H_2O,H_2(in)} = 0.0022 \ \frac{mol}{\min}\frac{18\ g}{mol}\frac{60\ \min}{1h} = 2.4091 \ \frac{g}{h}$$

$$m_{H_2O,Air\ (in)} = 0.0070 \ \frac{mol}{\min}\frac{18\ g}{mol}\frac{60\ \min}{1h} = 7.60 \ \frac{g}{h}$$

D4.2.2 Mass flow of water exiting the knockout drum with gas streams

Assumption: - The effluent water flows out from the knockout drums in the vapor phase at room temperature (25 °C).

- The water condenses in the knockout drums at the dew point temperature of the gas streams.

Set of data is given:

Variable	Value
$Q_{H_2,ko}$	0.113 SLPM
$Q_{Air,ko}$	0.358 SLPM
$T_{H_2,ko}$	25°C
$T_{Air,ko}$	25°C
$RH_{H_2,ko} = RH_{Air,ko}$	100%

Same as the calculation in Section D4.2.1, mass flow of water exiting the knockout drums with gas streams are calculated

- Mole fraction of water exiting the knockout drums

$$y_{H_2O,ko} = \frac{p_{H_2O}}{P_{tot}} = \frac{RH_{ko}}{100\ \%}\frac{P^{v}{}_{H_2O,ko}(T)}{P_{tot}}$$

$$y_{H_2O,H_2} = y_{H_2O,Air} = \frac{100\ \%}{100\ \%}\frac{P^{v}{}_{H_2O,ko}(25^{\circ}C)}{760}$$

- From Antoine's equation: $P^{v}{}_{H_2O,ko}(25^{\circ}C)$ is obtained

$$\log_{10}(P^{v}{}_{H_2O,ko}(25^{\circ}C)) = 8.0713 - \frac{1730.63}{25 + 233.426} = 1.3745$$

$$P^{v}{}_{H_2O,ko}(25^{\circ}C) = 23.69\ mmHg$$

Thus,

$$y_{H_2O,H_2} = y_{H_2O,Air} = \frac{100\ \%}{100\ \%}\frac{23.69\ mmHg}{760\ mmHg} = 0.0312$$

- Molar flow rate of water exiting the knockout drums

$$n_{H_2O,H_2} = \frac{y_{H_2O,H_2}}{(1 - y_{H_2O,H_2})} n_{H_2,in} = \frac{0.0312}{(1 - 0.0312)} 0.0050\ \frac{mol}{\min} = 0.0002\ \frac{mol}{\min}$$

$$n_{H_2O,Air} = \frac{y_{H_2O,Air}}{(1 - y_{H_2O,Air})} n_{Air,in} = \frac{0.0312}{(1 - 0.0312)} 0.0159\ \frac{mol}{\min} = 0.0005\ \frac{mol}{\min}$$

Converting molar flow to mass flow gives

$$m_{H_2O,H_2} = 0.0002\ \frac{mol}{\min}\frac{18\ g}{mol}\frac{60\ \min}{1h} = 0.216\ \frac{g}{h}$$

$$m_{H_2O,Air} = 0.0005\ \frac{mol}{\min}\frac{18\ g}{mol}\frac{60\ \min}{1h} = 0.553\ \frac{g}{h}$$

D4.2.3 Cathode water production from electrochemical reaction

The water production at the cathode side can be calculated through a reduction reaction as follows:

$$2H^+ + ½\ O_2 + 2e^- \rightarrow H_2O$$

Set of data is given:

Variable	Value1
i	11.83 mA cm^{-2}
A_{geo}	42.25 cm^2

- The moles of water produced at the cathode through the reaction

$$n_{H_2O,rxn} = i \frac{A}{1000\ mA} \frac{A_{geo}}{2F}$$

$$n_{H_2O,rxn} = 11.83 \frac{mA}{cm^2} \frac{A}{1000\ mA} 42.25\ cm^2 \frac{\frac{1C}{s}}{1A} \frac{1}{96485\ \frac{C}{mol\ e^-}} \frac{1 mol\ H_2O}{2 mol\ e^-} \frac{3600\ s}{1h} = 0.0093\ \frac{mol}{h}$$

Thus the mass flow is

$$m_{H_2O,rxn} = 0.0093\ \frac{mol}{h} \frac{18\ g}{mol} = 0.1678\ \frac{g}{h}$$

D4.2.4 Condensed water collection rates

Water condensation rates are determined by the mass of water collected in the knockout drums. The following is the water condensation rates measured in the knockout drums:

Variable	Value
$m_{H_2O,H_2(con)}$	2.2619 g/h
$m_{H_2O,Air\ (con)}$	6.6667 g/h

D4.2.5 Overall mass balance of water

The theoretical water collection rates are given by the amount of anode or cathode water provided into the fuel cell minus by the water exiting from the knockout drums.

- For the anode:

$$m_{H_2O,H_2(con)} = m_{H_2O,H_2(in)} - m_{H_2O,H_2(KO)} = 2.4091\ \frac{g}{h} - 0.216\ \frac{g}{h} = 2.1931\ \frac{g}{h}$$

- For the cathode the water produced during the electrochemical reaction must also included as shown:

$$m_{H_2O,Air\ (con)} = m_{H_2O,Air\ (in)} + m_{H_2O,Air\ (rxn)} - m_{H_2O,Air\ (KO)} = 7.60\ \frac{g}{h} + 0.1678\ \frac{g}{h} - 0.553\ \frac{g}{h} = 7.2148\ \frac{g}{h}$$

- From theory, the overall water balance is

$$m_{H_2O,H_2(con)} + m_{H_2O,Air\ (con)} = 2.1931\ \frac{g}{h} + 7.2148\ \frac{g}{h} = 9.4079\ \frac{g}{h}$$

Compared to the actual water collection from Section D4.2.4.

$$2.2619\ \frac{g}{h} + 6.6667\ \frac{g}{h} = 8.9286\ \frac{g}{h}$$

- The error between the measured and theoretical water collection rate is

$$Error = 100 \times \left| \frac{9.4079 \ \frac{g}{h} - 8.9286 \ \frac{g}{h}}{8.9286 \ \frac{g}{h}} \right| = 5.37\,\%$$